DISSERTATION

ADVANCED NANOSTRUCTURED MATERIALS FOR ENHANCING BIOACTIVITY

Submitted by

Abhishek Bhattacharjee

School of Advanced Materials Discovery

In partial fulfilment of the requirements

For the Degree of Doctor of Philosophy

Colorado State University

Fort Collins, Colorado

Spring 2024

Doctoral Committee:

Advisor: Ketul C. Popat

Walajabad Sampath
Margarita Herrera-Alonso
Zhijie Wang

ABSTRACT

ADVANCED NANOSTRUCTURED MATERIALS FOR ENHANCING BIOACTIVITY

Health hazards such as pathogenic infection, communicable diseases, and bone damage and injuries cause enormous human suffering and pain worldwide. Biomaterials such as orthopedic implants and biosensors are crucial tools to remedy these complications. Development of novel biomaterials and modifying existing materials can help enhance medical device efficacy. One of the key aspects of improving biomaterials is the utilization of nanotechnology. Nanoscale surface features can improve the interaction between materials and biological agents, thus improving their bioactivity. In this dissertation research, two different biomaterials were used for two distinct applications. Firstly, titanium, a common material for orthopedic implants, was used. Ti is a popular implant material because of its superior corrosion resistance, lightweight, and excellent biocompatibility. However, 10% of Ti implants fail each year due to pathogenic bacterial infection and poor osseointegration resulting in revision surgeries and immense suffering of the patients. Nanostructured surface modification approaches can potentially reduce the failure rate of Ti implants. In this study, TiO_2 nanotube arrays (NT) were fabricated followed by zinc (Zn) and strontium (Sr) doping. These elements provide important signals to mesenchymal stem cells to differentiate into osteoblasts which helps in bone healing. Zn also reduces bacterial adhesion to the implant surface. Results showed that the modified surfaces could significantly reduce bacterial adhesion and improved osseointegration properties of the mesenchymal stem cells. Secondly, a polydiacetylene (PDA)-based electrospun nanofiber biosensor was prepared that is flexible in nature for monitoring bacterial or viral infection. The nanofiber biosensor could selectively detect

Gram-negative bacteria via a vivid blue-to-red color transition. Since the color transition is visible to the naked eye, the biosensor offers immense potential to be used as a screening device for Gram-negative bacterial infection in various industries such as food packaging, medical, intelligence, and national security. During the COVID-19 pandemic, the PDA biosensing platform was utilized to detect the spike (S) protein of the SARS-CoV-2. For this, the surface chemistry of the PDA fibers was modified, and a receptor protein was conjugated at the end of the PDA polymer chain. When the modified PDA fibers were incubated with the S protein, the blue-to-red color transition happened, thus sensing the presence of S protein in the environment. This result indicated that PDA nanofiber biosensor is a flexible sensing platform for effectively detecting both bacteria and viruses. The two biomaterials investigated in this research indicated that the use of nanotechnology can help in enhancing their bioactivity.

ACKNOWLEDGEMENTS

Firstly, I would like to acknowledge the tremendous support that I received from my advisor, Dr. Ketul Popat. I consider myself privileged to have Dr. Popat as my academic advisor. Dr. Popat helped me cope during a tough time when I had to change labs and research topics in the middle of my Ph.D. program. Mere words cannot describe how grateful I am to Dr. Popat for saving my Ph.D. journey and helping me restart everything. Thank you so much, Dr. Popat, for being my mentor, teaching me actual research, and making my Ph.D. experience an insightful and enjoyable journey.

Secondly, I would like to thank my committee members, Dr. Walajabad Sampath, Dr. Margarita Herrera-Alonso, and Dr. Zhijie Wang, for their continuous support, insights, and encouragement. A special thanks to Dr. Paulo Soares from the Pontifícia Universidade Católica do Paraná in Brazil for providing me with collaborative research opportunities.

Next, I would like to express my gratitude towards my department, the School of Advanced Materials Discovery (SAMD). SAMD covered my academic expenses by providing Graduate Research Assistantship (GRA) and Graduate Teaching Assistantship (GTA). A special thanks to Caro Banuelos from SAMD for all the help and encouragement. I truly enjoyed her Professional Development classes, which changed my thought process towards professional activities and social life in a positive way. Also, thanks to Dr. Travis Bailey for supporting me in successfully completing my Ph.D. requirements.

Finally, I would like to thank my family and friends for their constant encouragement and guidance. I am immensely grateful to my wife, Anindita Chakraborty, who supported me unconditionally during the long tenure of higher education. I would also like to thank my mother,

Neli Chakraborty, who wholeheartedly encouraged me in all my life decisions. Additionally, I would like to thank my family members for their support during this time. Last but not least, I appreciate all my friends and lab mates who continuously encouraged, guided, and ensured a fun time, making this Ph.D. journey much more comfortable.

DEDICATION

I would like to dedicate this dissertation to-

My wife- Anindita Chakraborty

And my mom- Neli Chakraborty

For all the sacrifices so that I can pursue my dreams.

TABLE OF CONTENTS

CHAPTER 1/INTRODUCTION

1.1 Overview

Biomaterials are one of the important areas of research in materials science and engineering where a material encounters dynamic biological phenomena such as adult human cells, extracellular matrix, proteins, or pathogens such as bacteria. Performance of biomaterials depend on the successful interaction between the material surface and the biological agents. Since the nature of such interaction is largely diverse, research on novel material synthesis and surface modification approaches can enhance the functionality of biomaterials for biomedical applications. In this dissertation study, two separate classes of biomaterials were examined. One common theme among these two separate biomaterials is the use of nanotechnology. The first biomaterial of interest was titanium (Ti)-based orthopedic implant. Ti and its alloys are popular in orthopedic implant applications due to their excellent biocompatibility, superior corrosion resistance and lightweight properties [1]. However, approximately 10% of these implants fail each year due to bacterial infection and poor osseointegration [2]. To overcome this problem, a surface modification approach was investigated in this research. First, TiO_2 nanotubes (NT) arrays were fabricated on pure Ti surface by anodization, etching, and annealing processes. Then the surfaces were doped with important signaling ions for stem cells such as zinc (Zn) and strontium (Sr). Several material characterization tools were utilized to evaluate different properties of these modified surfaces. Then antibacterial activity and cell compatibility were assessed. The results indicated that the modified surfaces significantly reduced bacterial adhesion and improved cell adhesion, proliferation, growth. Moreover, the modified surfaces enhanced the osteoblasts differentiation of mesenchymal stem cells which is a strong indication of better osseointegration by the implants.

The second biomaterial of interest was polydiacetylene (PDA)-based nanofiber biosensor. PDA is a popular polymer for sensing different environmental stimuli such as change in heat and pH, organic solvents, and several pathogens such as bacteria, virus, and fungi. Among these applications of biosensor, pathogen detection is important for medical and food packaging industries to ensure a sterile working environment. Also, an easy and rapid pathogen detection method is paramount for reducing vector diseases such as the recent COVID-19 pandemic. In this work, a PDA nanofiber biosensor was prepared to selectively detect bacteria and pandemic coronavirus (SARS-CoV-2). The nanofiber biosensor was prepared by using electrospinning technique which is a relatively easy method of preparing nanoscale fiber mats. The biggest advantage of the PDA nanofiber biosensor over other sensing platform is the easy manufacturability and flexibility due to the fibrous nature of the material. The color of this fiber mat was blue after photopolymerization of PDA monomer. However, the color shifted to bright red when Gram-negative bacteria was introduced, indicating a selective detection of bacteria such as *Escherichia coli*. To detect the pandemic SARS-CoV-2, the end group of PDAs was transformed, and a receptor protein was conjugated to the fiber. When the spike protein of SARS-CoV-2 was introduced to this modified PDA fiber, the color changed to red indicating the successful detection of the pandemic coronavirus.

1.2 Bone disease and orthopedic implants

Bone diseases and bone related injuries are increasing health complications due to the increased population and mobility of human. Several bone diseases such as osteoarthritis, osteogenic imperfecta, osteoporosis, and bone cancer can cause significant loss of bone tissue and bone matrix along with bone deformation. Bone tissue loss and deformation can also result from

injuries due to accidents. Since the mobility of the human population has increased significantly over the last couple of decades, injuries from mobility related accidents are also projected to increase. Bone tissue provides the required structure of human body and supports mechanical stress which helps in mobility. Loss of bone tissue can cause severe pain and sufferings for the patient. One of the best remedies for bone related health complications is orthopedic implant. The implant provides necessary support to the patient while the body undergoes bone tissue remodeling over time. For these reasons, the implant should possess important material properties such as dynamic load bearing capability, tensile strength, flexibility, lightweight along with good biocompatibility and surface properties that can help improve the bone healing process. Therefore, understanding the material properties and their biocompatibility towards bone tissue is of superior importance for designing orthopedic implants.

The implant material can be metallic, polymeric, or composite, however, metallic implants are the most popular for orthopedic applications due to their advantageous material properties such as dynamic load-bearing capacity, strength, and excellent biocompatibility compared to polymeric or composite materials. Stainless steel and chromium-cobalt alloys have been popular choices for metallic orthopedic implants. Recently titanium (Ti) implants are gaining popularity due to their superior biocompatibility, high strength, and lower density which makes the implants lightweight compared to stainless steel and chromium-cobalt alloys. However, the Ti implants do possess some shortcomings, such as poor osteointegration and susceptibility to bacterial infection. Therefore, several research efforts were directed towards making the Ti implants more biocompatible. However, most of these works were focused on either reducing the bacterial infection or improving the osseointegration properties. There remains a lack of research efforts for surface modification of Ti implants that can reduce bacterial infection while improving the stem cell adhesion,

proliferation, growth, and differentiation to osteoblasts which results in better osteointegration. Therefore, in this work, surface modification approaches of Ti based orthopedic implants were performed with the help of nanotechnology for imparting better osteointegration and antibacterial activity simultaneously. The following sections will delve in-depth to understand the material properties of orthopedic implants especially of Ti, the superior advantages of Ti as an orthopedic implant, research approaches to improve the antibacterial properties and cell compatibility, surface modification approaches, ion implantation and their benefits, methods to impart important signaling ions, and finally the research goals of this dissertation.

1.3 Temporary and permanent orthopedic implants

Orthopedic implants are one of the most popular treatment procedures for bone healing due to bone diseases or fractures and injuries. The implant provides support to the damaged bone while the bone tissue regenerates and heals. These implants can be broadly classified into two types- temporary and permanent [3]. The temporary implants are mainly used for fracture treatment in bone caused by injuries. The implants provide support to the fractured bone tissue while bone regeneration happens to alleviate the fractured area. Plates, screws, and nails are the common shapes found for temporary implants. The permanent implants are inserted when the bone is damaged from diseases such as osteoarthritis, osteogenic imperfecta, or bone cancer when successful bone regeneration is not possible. The implant provides required mechanical properties and support to the diseased bone which helps the patient in conducting normal activities.

Since bone is a dynamic tissue, the implant should possess unique material properties for fulfilling its purpose. Polymers are used as implant material to reduce friction between two moving parts which can be two bones or two implants. To reduce friction our body naturally has cartilage

tissue between the bones. When this cartilage tissue is damaged, polymeric orthopedic implants are used. Ceramic implants are generally used as coatings to reduce inflammation and pathogenic infection. When a temporary or permanent implant is inserted to the body, its main function is to provide support to the damaged bone so that the pain and suffering to the patient is reduced. For that reason, a material with high load bearing capacity is desirable. Orthopedic implants for rigid bones such as hip and knee replacements often use metallic materials. Metals are well known to provide enhanced strength compared to polymers or ceramic materials during load-bearing applications. Also, passive metals can be anodized to produce an oxide layer which are known to be antifouling. Some metals produce this oxide layer naturally as a chemical reaction between the metal ion and oxygen in the environment, making metallic implants superior in biocompatibility. For a similar reason, dental implants often use metallic screws that supports the damaged teeth.

1.4 Titanium orthopedic implants

Since metals provide the desired dynamic load-bearing capacity, it serves as the most popular class of implants around the world. In the United States, 332,000 total hip and 719,000 total knee arthroplasties were performed in 2010, and the number is projected to increased almost 4 million by the year 2030 [4]. For almost 4000 years, humans are using implants to repair damaged tissues and organs with gold plate being used as the first synthetic implant in 1546 [5]. Since the middle of 20^{th} century, stainless steel has been a popular choice for orthopedic implants because of the corrosion resistance properties of 316L stainless steel which is also known as surgical stainless steel [6]. The corrosion resistance behavior of stainless steel was a determining factor since the metal will continuously be exposed to bodily fluids such as blood. However, stainless steel is highly susceptible to stress and crevice corrosion, thus limiting its use for

situations where material strength is not required for extended period of time [6]. Corrosion resistant stainless steel can possess various trace elements such as cobalt (Co), nickel (Ni), iron (Fe), molybdenum (Mo), and chromium. These elements can be released from the stainless-steel implants due to passivation process and impact the surrounding tissue adversely [7]. Trace elements such as Ni, Co, Cr, vanadium (V), aluminum (Al) can also be carcinogenic and impart toxicity to the surrounding environment [5]. On the other hand, titanium (Ti) can offer some advantageous properties that can overcome the shortcomings of stainless steel. Ti can provide superior corrosion resistance to the implant without the need for high alloying that is needed for 316L stainless steel. A systematic review between the stainless steel and titanium implants for fracture fixation was conducted by Barber et al. (2021) [8]. The researchers found that Ti had a lower rate of failure and fewer complications over stainless steel implants, although the researchers suggested further studies in the future. These results helped Ti based implants to achieve popularity in recent times as a material of choice for orthopedic implant applications. Around 1000 tons of Ti orthopedic implants are inserted into patients worldwide which signifies the ever-growing popularity of Ti implants [9].

1.5 Problems with Ti implants

Even though Ti offers tremendous benefits for orthopedic implant applications, it is not free of shortcomings. The first one is the cost of Ti. As a metal, Ti is almost 15-21% more expensive than stainless steel which increases the cost of implant surgeries [10]. However, cost can be reduced by economic measures and government sanctions if the material performs well. So, the major focus in this section will be determining if there are any functional shortcomings of Ti based orthopedic implants. Below are the two major factors where Ti based orthopedic implants suffers.

1.5.1 Poor osseointegration

The term osseointegration means a successful anchorage between the implant and the bone tissue [11]. When an implant is inserted to the host body, the first step is protein absorption on the material surface as a form of immune response from the host. If the surface of the implant resembles host environment, the immune response may subside, providing the bone progenitor cells and mesenchymal stem cells to get attached to the surface. Finally, these progenitor cells undergo osteoblast differentiation to form new bone matrix around the implant surface. As a metal, a passive oxide layer (TiO_2) is formed on the pure Ti surface. 10-100 angstrom thickness of this oxide layer can be formed within a minute and generally corrode less than 20μm/year [12]. This layer creates a barrier between the bulk Ti and the surrounding tissue. Also, this layer helps to avoid Ti corrosion by reducing passivation. However, metal corrosion can happen in the presence of a hostile biological environment where the passivation of TiO_2 layer occurs resulting in metal cation dissolution and release of electrons [12]. Denaro et al. (2008) showed that static electromagnetic field generated by corrosion current can inhibit the osteoblast differentiation which is an important factor for a successful osseointegration of Ti implants [13]. For the corrosion in Ti implants, inflammatory response can also occur that further worsen the implant loosening [14].

1.5.2 Bacterial infection

Surgery related infection is another major reason of Ti implant failure. Due to the lack of aseptic practices, bacterial cell can be carried inside the host with an orthopedic implant surface. Since the implant surface lacks vascular blood supply and proper immune response, bacterial infection can occur immediately after implant surgery [12]. **Figure 1.1** shows a scheme of bacterial

infection on biomaterial surfaces. If bacterial cells take over the surface, they form a biofilm which acts as a protective layer inside which the bacterial cells can easily proliferate. When the space and nutrition inside the biofilm get saturated, the cells break through the film and start to colonize new areas on the biomaterial surface. This cascade of events prevents host cells from getting attached to the surfaces and initiate tissue regeneration to heal the damaged area. Therefore, there is only a limited scope at the initiation stage after the surgery (marked in **Figure 1.1**) where biomaterial surfaces can prevent bacterial adhesion.

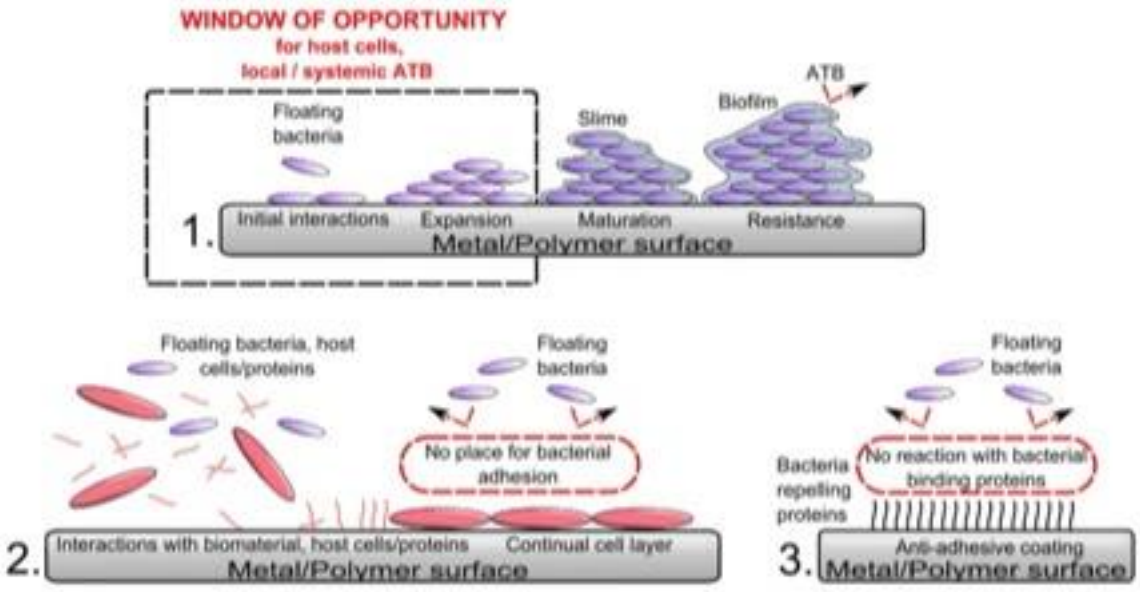

Figure 1.1. Schematic of bacterial infection on biomaterial surface and window of opportunity to prevent the infection. Adapted from [15]. Copyright 2014 by the authors, licensee MDPI, Basel, Switzerland, Creative Commons Attribution license (http://creativecommons.org/licenses/by/3.0/).

1.6 Surface modification approaches

To overcome the shortcomings of Ti orthopedic implants, surface modification approaches are utilized. One of the most popular surface modifications is hydroxyapatite (HA) coating on the pure Ti or its alloys. The coating can be performed using plasma spraying technique [16]. HA

produces a rough surface texture on the metallic implants that helps to improve osseointegration [12]. Moreover, bone mineral constitutes mainly of HA [12]. Therefore, immune response from the host during orthopedic implant surgery is reduced and cell adhesion properties improve with HA coatings. However, HA coatings are reported to be weaker that may break when dynamic loading is applied [17]. Thereofer, recently nanosurface modification approaches were conducted to improve osseointegration properties of Ti orthopedic implant. One such approach is to fabricate TiO_2 nanotube arrays (NT) on pure Ti or its alloys. Popat et al. (2007) fabricated the NT surfaces and found that the platform supports the growth and maintenance of bone cells effectively [18]. After that several surface modification approaches had been investigated for improving osseointegration properties on Ti. One of the recent approaches is interesting where researchers utilized polyelectrolytic multilayers of tanfloc/heparin on TiO_2 nanotube arrays [2]. The results indicated improved osteoblast differentiation of mesenchymal stem cells on these modified surfaces. However, all these approaches lack in providing important signaling to mesenchymal stem cells or bone progenitor cells to initiate osteoinduction and osteoconduction that can result into enhanced osseointegration for bone remodeling and healing purposes.

To reduce surgery related bacterial infection, oral antibiotics are often prescribed. However, this approach possesses an inherent risk of antibiotic resistant bacterial strain development [19]. Moreover, most the antibiotics on the market possess a short spectrum antibacterial activity, which may increase the risk of resistant bacterial strain infection on the implant surface. Therefore, surface modification approaches to include antibacterial activity on the implant surfaces is gaining more popularity in recent years [19]. One of the most popular choices to make a biomaterial surface antibacterial is to coat the surface with antibacterial chemicals. For instance, Chen et al. coated Ti surfaces with melimine using silane anchor to impart antibacterial

activity to the surfaces [20]. Their report shows bacterial adhesion and biofilm formation reduced 62% for *Pseudomonas aeruginosa* and 84% for *Staphylococcus aureus* [20]. Silane anchoring to impart antibacterial coating on Ti surfaces is another popular method of making orthopedic implant surfaces more antibacterial [21]. Apart from melimine and silane, other antibacterial agents such as silver (Ag), copper (Cu), and zinc (Zn) have been successfully implanted to the Ti surfaces for imparting antibacterial properties. Ferraris and Spriano (2016) documented implantation of these three popular antibacterial agents to the Ti surfaces [19]. They reported 3 principal strategies to make Ti surface antibacterial, namely- metal surface doping, TiO_2 layer growth and doping, and TiO_2 hydroxyapatite (HAp) coating. Ion implantation, plasma spray, sol-gel, plasma electrolytic oxidation (PEO), ion exchange, and sputtering are some of the popular methods to incorporate Ag, Cu and Zn ions to the implant surfaces. However, these antibacterial coatings may reduce the cell adhesion properties on the surfaces that can result into implant loosening and failure overtime.

1.7 Ion doping on titanium surfaces

Recently, ion implantation on Ti and NT surfaces are gaining popularity in the literature due to their enhanced antibacterial and osseointegration properties. Zinc (Zn) and strontium (Sr) ion doping are promising in this regard since they provide important signals to stem cells for differentiating into osteoblasts which can help in bone healing. Zn has been reported to improve osseointegration by osteoblast proliferation, mineralization, and osteoblast marker gene expression [22]. Zn can also prevent bone resorption by inhibiting osteoclast formation [22]. Several Zn doping techniques were reported in the literature on both Ti and NT surfaces such as alkaline heat treatment [23-24], hydrothermal treatment [22, 25-27], plasma electrolyte oxidation [28-29], and micro-arc oxidation method [30]. On the other hand, strontium has also been reported to improve

osseointegration properties during *in vivo* and *in vitro* studies [31]. Strontium gained more popularity after the development of antiosteoporosis drug of strontium ranelate [32]. Like Zn, Sr can also reduce osteoclast formation and improve osteoblast differentiation [33]. Several ion doping techniques such as micro-arc oxidation [34], hydrothermal treatment [35], and magnetron co-sputtering [36] have been reported to dope strontium on Ti and its alloys. However, there was a lack of research works to incorporate both Zn and Sr ions on TiO_2 nanotubes (NT) to improve both antibacterial and osseointegration properties.

1.8 Pathogenic bacteria and viruses

Pathogenic contamination and infection are major health hazards that cause enormous human and economic toll worldwide. According to the World Health Organization (WHO), pathogenic infection is one of the major reasons of children death around the world, mainly in the developing countries due to the lack of aseptic sanitary practices. Food borne pathogens are considered especially deadly since 91% of total foodborne outbreaks are caused by bacteria only [37]. Christian Gram developed a method to classify bacteria into two broad categories, Gram-positive and Gram-negative based on their outer membrane composition [38]. Gram-positive bacteria have a thick peptidoglycan outer layer that retains the primary violet stain during Gram-staining and exhibits a purple color. On the other hand, Gram- negative bacteria do not possess this thick outer layer and cannot retain the primary violet stain. Instead, Gram-negative bacteria retain the counter red stain during the Gram-staining test and exhibit a red or pink color [39]. One of the concerning bacterial strains for foodborne diseases is the Gram-negative *Escherichia coli* (*E. coli*). It was reported that *E. coli* can easily contaminate ground beef, milk, and chicken and when these contaminated foods are consumed, *E. coli* infection can occur in the lining of human

intestine causing severe health hazard [37]. Another problematic Gram-negative bacterial strain is *Salmonella* which is a genus from the bacteria family of Enterobacteriaceae. *E. coli* also falls into this bacteria family. Gram-negative bacteria from the Enterobacteriaceae family have been reported to cause urinary tract infection (UTI), bloodstream infections, hospital associated pneumonia, gastroenteritis, intra-abdominal infections, and other invasive infections in humans [40]. More and more bacterial strains from this family are becoming resistant to the available antibiotics and making the treatment procedures for bacterial infection highly complicated [40]. For this reason, selective detection of these bacteria using a simple and flexible detection method that can be incorporated into everyday materials is necessary.

Viruses are other pathogenic agents that can cause deadly health hazards to human population. Unlike bacteria, viruses cannot replicate themselves, instead they infect a host cell and make copies of themselves utilizing the host cell components [41]. The structure of most viruses is simple, consisting of a segment of nucleic acid such as DNA or RNA which is surrounded by a protein coat [41]. Among these viruses, coronavirus is a well-known name around the world due to recent global pandemic that caused millions of deaths and unimaginable economic and social burdens in almost all of the countries.

Coronavirus is an enveloped virus that has corona-shaped spiked protein on its outer membrane, and hence got its name. These viruses used to cause mild respiratory diseases in humans until the emergence of severe acute respiratory syndrome coronavirus (SARS-CoV) which was a variant of coronaviruses that transmitted from animal to human [42]. Then in 2019, another variant of SARS-CoV emerged in Wuhan, China where a cluster of pneumonia patients were identified infected with this new virus which later became known as SARS-CoV-2 [43]. On 11 March 2020, World Health Organization (WHO) declared the associated disease COVID-19 as a

pandemic [44]. SARS-CoV-2 has glycosylated spike (S) proteins that forms the corona shape around the viral outer membrane [45]. This protein can bind to the angiotensin-converting enzyme II (ACE2) receptor found in the lower respiratory tract of human, causing the pneumonia like COVID-19 disease [46]. To check the spread of this deadly pandemic viral disease, a number of viral identification techniques were identified. Among them, real-time reverse transcription-polymerase chain reaction (rRT-PCR) based virus identification tools were of great interest. However, these techniques require complex protocols, trained personnel, and are often prone to false-negative results which can complicates the problem manifold [47]. Therefore, a simple, fast, and reliable virus detection technique is necessary to develop.

1.9 Color changing polymer- polydiacetylene

Polydiacetylene (PDA) is a popular color changing popular that has gained popularity in recent years due to its stimuli detection capability. A diacetylene monomer can be easily photopolymerized to create PDA which exhibits a blue color. PDA has alternating alkene alkyne structure that creates an electron cloud in the polymer [48]. When this electron cloud is perturbed upon interaction to an environmental stimulus, a color change happens in the polymer structure from blue to red [49]. So, the presence of the specific environmental stimuli is detected due to the vivid blue to red color transition in the polymer. Utilizing this phenomenon, a number of biosensor applications have been reported in the literature such as heat change [48], pH change [49], bacteria [50] and virus [51].

1.10 Polydiacetylene nanofiber preparation by electrospinning

Although different platforms of PDA-based biosensors have been reported, nanofiber platform can offer some advantageous properties. The diameter of the nanofibers is in the nanometer range, offering a high aspect ratio (length: diameter). For a biosensor, high aspect ratio is highly desirable because they can provide a larger surface area to come in contact with the target such as bacteria or virus. Moreover, nanofibers are flexible structures that can be incorporated into everyday material or fiber mat can be used as its own. Nanofibers can be easily prepared by a technique called electrospinning. During electrospinning, the polymer of interest is taken in a syringe and pushed through a metallic needle which is known as the spinneret. A Taylor cone is created during this time at the tip of the needle. Then an electrical force is applied between the metallic tip and a metallic fiber collector plate. When the electrical force is greater than the surface tension of the polymer, the Taylor cone gets disrupted, and a fiber jet is created that shoots towards the collector plate. During this time, the solvent gets evaporated, and the polymer is stretched to form fibers. The fiber is collected on the metallic collector plate [52]. To prepare PDA nanofibers, first the electrospinning solution is prepared by mixing the diacetylene monomer with a matrix polymer. This is because diacetylene monomers do not have required viscosity or spinnability. Two matrix polymers have been used most to prepare PDA nanofibers- polyurethane (PU) and poly (ethylene oxide) (PEO). Among these two matrix polymers, PU is advantageous because it is a superhydrophobic polymer that do not dissolve with common biological agents such as growth media for bacteria or virus. Due to the superhydrophobic properties of PU, the PU-PDA fiber also becomes superhydrophobic [53]. PU-PDA nanofibers can be easily prepared by using the electrospinning technique. Different electrospinning parameters such as voltage, distance between spinneret and collector, polymer insertion rate, polymer solution concentration, and temperature

and relative humidity of the setup can change the properties of the fibers [52]. For example, when the voltage is too high, the solvents do not get enough time to evaporate, and thus creates beads on the fibers which are droplets of unevaporated solvents. On the other hand, if the voltage is too low, the surface tension of the polymer will be more, and the polymer jet may not form. So, optimizing the electrospinning parameters can prepare PU-PDA fiber mats with diameters in the nanoscale.

1.11 Bacteria and virus detection by PDA nanofiber

PDA interacts with biological agents such as bacteria and viruses since they are environmental stimuli and perturbs the electron clouds of the polymer chain. Alam et al. (2016) prepared a polyethylene-PDA fiber matrix that can detect a heat change greater than 55ºC [48]. Park et al. formulated another PDA nanofiber matrix as a low temperature thermochromic sensor [54]. Yapor et al. (2017) and Bhattacharjee et al. (2020) reported a PU-PDA fiber matrix that can detect bacteria in separate reports [49, 50]. Yapor et al. (2017) also reported that the PU-PDA fiber could detect a pH change greater than 11 [49]. Then, Hassan et al. (2019) did a microstructure and mechanical properties analysis of PDA nanofibers and found that PU-PDA were most suitable for detecting biological agents due to dissolution problems of PEO in liquid solutions [55]. Valdez et al. (2019) prepared a PDA based nanofiber sensor to detect food spoilage by using a ForceSpun® technique [56]. Although PDA polymer has been used in other forms, no other reports were found to use PDA nanofibers to detect bacteria. Also, selective bacteria detection by the PDA nanofibers were not investigated before.

The pioneering work of Charych et al. (1993) exhibited the potential of PDA for virus detection. In the work, a PDA bilayer assembly was prepared and functionalized with sialic acid

ligand to detect influenza virus hemagglutinin [57]. Son et al. (2019) reported a PDA-based paper sensor to detect pandemic influenza A (pH1N1) [51]. Jiang et al. (2015) functionalized the PDA vesicles with anti-H5 influenza antibody to detect influenza virus by a colorimetric transition in the vesicle [58]. Another influenza virus detecting sensor was prepared by Song et al. (2016) by utilizing peptide-functionalized polydiacetylene (PEP-PDA) [59]. Other viruses and viral DNA, RNA, and protein detection was reported that utilized PDA based colorimetric sensors [60]. All these works utilized PDA based membranes or vesicles to detect the presence of virus via a color change. However, no work was found that reported a PDA nanofiber platform to detect viruses or their associated proteins. Moreover, no PDA nanofiber sensor was found in the literature that can detect the coronavirus, especially SARS-CoV-2 that caused the recent pandemic.

1.12 Hypothesis

Nanoscale surface modification approaches and novel material synthesis using nanotechnology can improve bioactivity of materials. Bioactivity relates to the improvement of antibacterial activity, stem cell adhesion, proliferation, and differentiation, and rapid sensing of pathogenic biological agents by nanostructured surfaces.

1.12.1 Specific aim 1: The first nanostructured material developed in this study is TiO_2 nanotube (NT) surfaces doped with important trace elements such as zinc and strontium to improve antibacterial activity, and stem cell adhesion, proliferation, and differentiation to osteoblasts that results in better osseointergation. These research works are discussed in **Chapters 1, 2, 3, and 4.**

a) Fabrication and characterization of TiO_2 nanotube (NT) surface by anodization, etching, and annealing techniques followed by doping with zinc (Zn) using hydrothermal and alkaline heat-treatment methods to evaluate antibacterial activity of the surfaces.
b) Fabrication and characterization of NT surfaces doped with either Zn or strontium (Sr) to evaluate adipose derived stem cell (ADSC) adhesion, proliferation, and differentiation to osteoblasts.
c) Fabrication and characterization of NT surfaces simultaneously doped with Zn and Sr to evaluate antibacterial activity and ADSC adhesion, proliferation, and differentiation to osteoblasts.

1.12.2 Specific aim 2: The second nanostructured material developed in this study is polydiacetylene (PDA) nanofiber prepared by electrospinning technique. The nanofiber was developed to selectively detect Gram-negative bacteria via a color change from blue to red. The surface chemistry of the nanofiber was changed to conjugate a receptor protein to detect the pandemic coronavirus (SARS-CoV-2) via a similar color change. These research works are discussed in. **Chapters 1, 5, and 6.**

a) Fabrication and characterization of PDA nanofiber biosensor to selectively detect Gram-negative bacteria by a color transition from blue to red.
b) Fabrication and characterization of PDA nanofiber biosensor by conjugating a receptor protein to the PDA polymer for detecting the spike protein of SARS-CoV-2.

REFERENCES

1. Taddei, E. B., Henriques, V. A. R., Silva, C. R. M., & Cairo, C. A. A. (2004). Production of new titanium alloy for orthopedic implants. *Materials Science and Engineering: C*, *24*(5), 683-687. https://doi.org/10.1016/j.msec.2004.08.011
2. Sabino, R. M., Mondini, G., Kipper, M. J., Martins, A. F., & Popat, K. C. (2021). Tanfloc/heparin polyelectrolyte multilayers improve osteogenic differentiation of adipose-derived stem cells on titania nanotube surfaces. *Carbohydrate polymers*, *251*, 117079. https://doi.org/10.1016/j.carbpol.2020.117079
3. Jin, W., & Chu, P. K. (2019). Orthopedic implants. *Encyclopedia of biomedical engineering*, *1*(3), 425-439. https://doi.org/10.1016/B978-0-12-801238-3.10999-7
4. Tande, A. J., & Patel, R. (2014). Prosthetic joint infection. *Clinical microbiology reviews*, *27*(2), 302-345. https://doi.org/10.1128/cmr.00111-13
5. Eliaz, N. (2019). Corrosion of metallic biomaterials: A review. *Materials*, *12*(3), 407. https://doi.org/10.3390%2Fma12030407
6. Walley, K. C., Bajraliu, M., Gonzalez, T., Nazarian, A., & Goulet, J. A. (2016). The chronicle of a stainless steel orthopaedic implant. *The Orthopaedic journal at Harvard medical school*, *17*, 68-74. http://www.orthojournalhms.org/17/article68_74.html
7. Hofmann, J., Michel, R., Holm, R., & Zilkens, J. (1981). Corrosion behaviour of stainless steel implants in biological media. *Surface and interface analysis*, *3*(3), 110-117. https://doi.org/10.1002/sia.740030304

8. Barber, C. C., Burnham, M., Ojameruaye, O., & McKee, M. D. (2021). A systematic review of the use of titanium versus stainless steel implants for fracture fixation. *OTA International*, *4*(3). https://doi.org/10.1097%2FOI9.0000000000000138
9. John, A. A., Jaganathan, S. K., Supriyanto, E., & Manikandan, A. (2016). Surface modification of titanium and its alloys for the enhancement of osseointegration in orthopaedics. *Current Science*, 1003-1015. https://www.jstor.org/stable/24908502
10. Banovetz, J. M., Sharp, R., Probe, R. A., & Anglen, J. O. (1996). Titanium plate fixation: a review of implant failures. *Journal of orthopaedic trauma*, *10*(6), 389-394.
11. Albrektsson, T., & Johansson, C. (2001). Osteoinduction, osteoconduction and osseointegration. *European spine journal*, *10*(Suppl 2), S96-S101. https://doi.org/10.1007/s005860100282
12. Petersen, R. C. (2014). Titanium implant osseointegration problems with alternate solutions using epoxy/carbon-fiber-reinforced composite. *Metals*, *4*(4), 549-569. https://doi.org/10.3390/met4040549
13. Denaro, V., Cittadini, A., Barnaba, S. A., Ruzzini, L., Denaro, L., Rettino, A., ... & Sgambato, A. (2008). Static electromagnetic fields generated by corrosion currents inhibit human osteoblast differentiation. *Spine*, *33*(9), 955-959. https://doi.org/10.1097/brs.0b013e31816c90b8
14. Dias-Netipanyj, M. F., Cowden, K., Sopchenski, L., Cogo, S. C., Elifio-Esposito, S., Popat, K. C., & Soares, P. (2019). Effect of crystalline phases of titania nanotube arrays on adipose derived stem cell adhesion and proliferation. *Materials Science and Engineering: C*, *103*, 109850. https://doi.org/10.1016/j.msec.2019.109850

15. Gallo, J., Holinka, M., & Moucha, C. S. (2014). Antibacterial surface treatment for orthopaedic implants. *International journal of molecular sciences*, *15*(8), 13849-13880. https://doi.org/10.3390/ijms150813849

16. Ji, H., Ponton, C. B., & Marquis, P. M. (1992). Microstructural characterization of hydroxyapatite coating on titanium. *Journal of Materials Science: Materials in Medicine*, *3*, 283-287. https://doi.org/10.1007/BF00705294

17. Nakashima, Y., Hayashi, K., Inadome, T., Uenoyama, K., Hara, T., Kanemaru, T., ... & Noda, I. (1997). Hydroxyapatite-coating on titanium arc sprayed titanium implants. *Journal of Biomedical Materials Research: An Official Journal of The Society for Biomaterials and The Japanese Society for Biomaterials*, *35*(3), 287-298. https://doi.org/10.1002/(SICI)1097-4636(19970605)35:3%3C287::AID-JBM3%3E3.0.CO;2-D

18. Popat, K. C., Leoni, L., Grimes, C. A., & Desai, T. A. (2007). Influence of engineered titania nanotubular surfaces on bone cells. *Biomaterials*, *28*(21), 3188-3197. https://doi.org/10.1016/j.biomaterials.2007.03.020

19. Ferraris, S., & Spriano, S. J. M. S. (2016). Antibacterial titanium surfaces for medical implants. *Materials Science and Engineering: C*, *61*, 965-978. https://doi.org/10.1016/j.msec.2015.12.062

20. Chen, R., Willcox, M. D., Ho, K. K. K., Smyth, D., & Kumar, N. (2016). Antimicrobial peptide melimine coating for titanium and its in vivo antibacterial activity in rodent subcutaneous infection models. *Biomaterials*, *85*, 142-151. https://doi.org/10.1016/j.biomaterials.2016.01.063

21. Chouirfa, H., Bouloussa, H., Migonney, V., & Falentin-Daudré, C. (2019). Review of titanium surface modification techniques and coatings for antibacterial applications. *Acta biomaterialia*, *83*, 37-54. https://doi-org./10.1016/j.actbio.2018.10.036

22. Huo, K., Zhang, X., Wang, H., Zhao, L., Liu, X., & Chu, P. K. (2013). Osteogenic activity and antibacterial effects on titanium surfaces modified with Zn-incorporated nanotube arrays. *Biomaterials*, *34*(13), 3467-3478. https://doi.org/10.1016/j.biomaterials.2013.01.071

23. Yusa, K., Yamamoto, O., Takano, H., Fukuda, M., & Iino, M. (2016). Zinc-modified titanium surface enhances osteoblast differentiation of dental pulp stem cells in vitro. *Scientific Reports*, *6*(1), 29462. https://doi.org/10.1038/srep29462

24. Alvarez, K., Fukuda, M., & Yamamoto, O. (2010). Titanium Implants after Alkali Heating Treatment with a [Zn (OH) 4] 2− Complex: Analysis of Interfacial Bond Strength Using Push-Out Tests. *Clinical implant dentistry and related research*, *12*, e114-e125. https://doi.org/10.1111/j.1708-8208.2010.00278.x

25. Li, Y., Xiong, W., Zhang, C., Gao, B., Guan, H., Cheng, H., ... & Li, F. (2014). Enhanced osseointegration and antibacterial action of zinc-loaded titania-nanotube-coated titanium substrates: In vitro and in vivo studies. *Journal of Biomedical Materials Research Part A*, *102*(11), 3939-3950. https://doi.org/10.1002/jbm.a.35060

26. Cheng, H., Mao, L., Wang, L., Hu, H., Chen, Y., Gong, Z., ... & Zhu, Z. (2015). Bidirectional regulation of zinc embedded titania nanorods: antibiosis and osteoblastic cell growth. *RSC advances*, *5*(19), 14470-14481. https://doi.org/10.1039/C4RA17058J

27. Nageri, M., Kalarivalappil, V., Vijayan, B. K., & Kumar, V. (2016). Titania nanotube arrays surface-modified with ZnO for enhanced photocatalytic applications. *Materials Research Bulletin*, *77*, 35-40. https://doi.org/10.1016/j.materresbull.2016.01.020

28. Zhang, Z., Gu, B., Zhang, W., Kan, G., & Sun, J. (2012). The enhanced characteristics of osteoblast adhesion to porous Zinc–TiO_2 coating prepared by plasma electrolytic oxidation. *Applied surface science*, *258*(17), 6504-6511. https://doi.org/10.1016/j.apsusc.2012.03.067

29. Hu, H., Zhang, W., Qiao, Y. Q., Jiang, X. Y., Liu, X., & Ding, C. (2012). Antibacterial activity and increased bone marrow stem cell functions of Zn-incorporated TiO_2 coatings on titanium. *Acta biomaterialia*, *8*(2), 904-915. https://doi.org/10.1016/j.actbio.2011.09.031

30. Zhao, Q. M., Cheng, L., Liu, Z. T., & Zhao, J. J. (2014). Surface characteristics of Zinc– TiO_2 coatings prepared via micro-arc oxidation. *Composite Interfaces*, *21*(6), 585-593. http://dx.doi.org/10.1080/15685543.2014.914377

31. Shi, J., Li, Y., Gu, Y., Qiao, S., Zhang, X., & Lai, H. (2017). Effect of titanium implants with strontium incorporation on bone apposition in animal models: A systematic review and meta-analysis. *Scientific Reports*, *7*(1), 15563. https://doi.org/10.1038/s41598-017-15488-1

32. Bonnelye, E., Chabadel, A., Saltel, F., & Jurdic, P. (2008). Dual effect of strontium ranelate: stimulation of osteoblast differentiation and inhibition of osteoclast formation and resorption in vitro. *Bone*, *42*(1), 129-138. https://doi.org/10.1016/j.bone.2007.08.043

33. Zhang, K., Zhu, Y., Liu, X., Cui, Z., Yeung, K. W., Pan, H., & Wu, S. (2017). Sr/ZnO doped titania nanotube array: an effective surface system with excellent osteoinductivity and self-antibacterial activity. *Materials & Design*, *130*, 403-412. https://doi.org/10.1016/j.matdes.2017.05.085

34. Zhang, W., Cao, H., Zhang, X., Li, G., Chang, Q., Zhao, J., ... & Jiang, X. (2016). A strontium-incorporated nanoporous titanium implant surface for rapid osseointegration. *Nanoscale*, *8*(9), 5291-5301. https://doi.org/10.1039/C5NR08580B

35. Zhao, L., Wang, H., Huo, K., Zhang, X., Wang, W., Zhang, Y., ... & Chu, P. K. (2013). The osteogenic activity of strontium loaded titania nanotube arrays on titanium substrates. *Biomaterials*, *34*(1), 19-29. https://doi.org/10.1016/j.biomaterials.2012.09.041

36. Andersen, O. Z., Offermanns, V., Sillassen, M., Almtoft, K. P., Andersen, I. H., Sørensen, S., ... & Foss, M. (2013). Accelerated bone ingrowth by local delivery of strontium from surface functionalized titanium implants. *Biomaterials*, *34*(24), 5883-5890. https://doi.org/10.1016/j.biomaterials.2013.04.031

37. Ivnitski, D., Abdel-Hamid, I., Atanasov, P., & Wilkins, E. (1999). Biosensors for detection of pathogenic bacteria. *Biosensors and Bioelectronics*, *14*(7), 599-624. https://doi.org/10.1016/S0956-5663(99)00039-1

38. Bartholomew, J. W., & Mittwer, T. (1952). The gram stain. *Bacteriological reviews*, *16*(1), 1-29.

39. Smith, A. C., & Hussey, M. A. (2005). Gram stain protocols. *American Society for Microbiology*, *1*(14), 113-144.

40. Paterson, D. L. (2006). Resistance in gram-negative bacteria: Enterobacteriaceae. *American journal of infection control*, *34*(5), S20-S28. https://doi.org/10.1016/j.ajic.2006.05.238

41. National Human Genome Research Institute (NHGRI). (2024, February 26). *Virus*. https://www.genome.gov/genetics-glossary/Virus

42. Hoffmann, M., Kleine-Weber, H., Schroeder, S., Krüger, N., Herrler, T., Erichsen, S., ... & Pöhlmann, S. (2020). SARS-CoV-2 cell entry depends on ACE2 and TMPRSS2 and is blocked by a clinically proven protease inhibitor. *cell*, *181*(2), 271-280. https://doi.org/10.1016/j.cell.2020.02.052

43. Zhu, N., Zhang, D., Wang, W., Li, X., Yang, B., Song, J., ... & Tan, W. (2020). A novel coronavirus from patients with pneumonia in China, 2019. *New England journal of medicine*, *382*(8), 727-733. https://doi.org/10.1056/NEJMoa2001017

44. World Health Organization (WHO). (2020, March 11). *Coronavirus disease 2019 (COVID-19) Situation Report – 51*. https://www.who.int/docs/default-source/coronaviruse/situation-reports/20200311-sitrep-51-covid-19.pdf?sfvrsn=1ba62e57_10

45. Ashour, H. M., Elkhatib, W. F., Rahman, M. M., & Elshabrawy, H. A. (2020). Insights into the recent 2019 novel coronavirus (SARS-CoV-2) in light of past human coronavirus outbreaks. *Pathogens*, *9*(3), 186. https://doi.org/10.3390/pathogens9030186

46. Zhou, P., Yang, X. L., Wang, X. G., Hu, B., Zhang, L., Zhang, W., ... & Shi, Z. L. (2020). A pneumonia outbreak associated with a new coronavirus of probable bat origin. *nature*, *579*(7798), 270-273. https://doi.org/10.1038/s41586-020-2012-7

47. Lai, C. C., Wang, C. Y., Ko, W. C., & Hsueh, P. R. (2021). In vitro diagnostics of coronavirus disease 2019: Technologies and application. *Journal of Microbiology, Immunology and Infection*, *54*(2), 164-174. https://doi.org/10.1016/j.jmii.2020.05.016

48. Alam, A. M., Yapor, J. P., Reynolds, M. M., & Li, Y. V. (2016). Study of polydiacetylene-poly (ethylene oxide) electrospun fibers used as biosensors. *Materials*, *9*(3), 202. https://doi.org/10.3390/ma9030202

49. Yapor, J. P., Alharby, A., Gentry-Weeks, C., Reynolds, M. M., Alam, A. M., & Li, Y. V. (2017). Polydiacetylene nanofiber composites as a colorimetric sensor responding to *Escherichia coli* and pH. *ACS omega*, *2*(10), 7334-7342. https://doi.org/10.1021/acsomega.7b01136

50. Bhattacharjee, A., Clark, R., Gentry-Weeks, C., & Li, Y. V. (2020). A novel receptor-free polydiacetylene nanofiber biosensor for detecting *E. coli* via colorimetric changes. *Materials Advances*, *1*(9), 3387-3397. https://doi.org/10.1039/D0MA00619J

51. Son, S. U., Seo, S. B., Jang, S., Choi, J., Lim, J. W., Lee, D. K., ... & Lim, E. K. (2019). Naked-eye detection of pandemic influenza a (pH1N1) virus by polydiacetylene (PDA)-based paper sensor as a point-of-care diagnostic platform. *Sensors and Actuators B: Chemical*, *291*, 257-265. https://doi.org/10.1016/j.snb.2019.04.081

52. Bhardwaj, N., & Kundu, S. C. (2010). Electrospinning: A fascinating fiber fabrication technique. *Biotechnology advances*, *28*(3), 325-347. https://doi.org/10.1016/j.biotechadv.2010.01.004

53. Chen, L., Wu, F., Li, Y., Wang, Y., Si, L., Lee, K. I., & Fei, B. (2018). Robust and elastic superhydrophobic breathable fibrous membrane with in situ grown hierarchical structures. *Journal of Membrane Science*, *547*, 93-98. https://doi.org/10.1016/j.memsci.2017.10.023

54. Park, I. S., Park, H. J., Jeong, W., Nam, J., Kang, Y., Shin, K., ... & Kim, J. M. (2016). Low temperature thermochromic polydiacetylenes: design, colorimetric properties, and nanofiber formation. *Macromolecules*, *49*(4), 1270-1278. https://doi.org/10.1021/acs.macromol.5b02683

55. Hassan, F., Gentry-Weeks, C., Reynolds, M., & Li, Y. V. (2019). Study on microstructure and mechanical properties of polydiacetylene composite biosensors. *Journal of Applied Polymer Science*, *136*(34), 47877. https://doi.org/10.1002/app.47877

56. Valdez, M., Gupta, S. K., Lozano, K., & Mao, Y. (2019). ForceSpun polydiacetylene nanofibers as colorimetric sensor for food spoilage detection. *Sensors and Actuators B: Chemical*, *297*, 126734. https://doi.org/10.1016/j.snb.2019.126734

57. Charych, D. H., Nagy, J. O., Spevak, W., & Bednarski, M. D. (1993). Direct colorimetric detection of a receptor-ligand interaction by a polymerized bilayer assembly. *Science*, *261*(5121), 585-588. https://www.science.org/doi/abs/10.1126/science.8342021

58. Jiang, L., Luo, J., Dong, W., Wang, C., Jin, W., Xia, Y., ... & He, H. (2015). Development and evaluation of a polydiacetylene based biosensor for the detection of H5 influenza virus. *Journal of virological methods*, *219*, 38-45. https://doi.org/10.1016/j.jviromet.2015.03.013

59. Song, S., Ha, K., Guk, K., Hwang, S. G., Choi, J. M., Kang, T., ... & Lim, E. K. (2016). Colorimetric detection of influenza A (H1N1) virus by a peptide-functionalized polydiacetylene (PEP-PDA) nanosensor. *RSC advances*, *6*(54), 48566-48570. https://doi.org/10.1039/C6RA06689E

60. Qian, X., & Städler, B. (2020). Polydiacetylene-Based Biosensors for the Detection of Viruses and Related Biomolecules. *Advanced Functional Materials*, *30*(49), 2004605. https://doi.org/10.1002/adfm.202004605

CHAPTER 2/ZINC (ZN) DOPING BY HYDROTHERMAL AND ALKALINE HEAT-TREATMENT METHODS ON TITANIA NANOTUBE ARRAY FOR ENHANCED ANTIBACTERIAL ACTIVITY[1]

2.1 Introduction

Titanium (Ti) is a popular biomaterial for orthopedic implant applications due to its superior mechanical properties such as corrosion resistance and low modulus of elasticity. However, around 10% of these implants fail annually due to bacterial infection and poor osseointegration resulting in severe pain and suffering for the patients. To improve their performance, nanoscale surface modification approaches and doping of trace elements on the surfaces can be utilized that may help in improving cell adhesion for better osseointegration while reducing bacterial infection. In this work, at first, titania (TiO_2) nanotube arrays (NT) were fabricated on commercially available pure Ti surfaces via anodization. Then zinc (Zn) doping was conducted following two distinct methods- hydrothermal and alkaline-heat treatment. Scanning electron microscopic (SEM) images of the prepared surfaces revealed unique surface morphologies, while energy dispersive X-ray spectroscopy (EDS) revealed Zn distribution on the surfaces. Contact angle measurement indicated that NT surfaces were superhydrophilic. X-ray photoelectron spectroscopy (XPS) provided the relative amount of Zn on the surfaces and indicated that hydrothermally treated surfaces had more Zn compared to the alkaline-heat treated surfaces. X-ray crystallography (XRD) and nanoindentation techniques provided the crystal structure and mechanical properties of the surfaces. While testing with adipose derived stem cells (ADSC), the

[1]This work was published in *Nanomaterials* and is reproduced here with permission [1].

surfaces showed no apparent cytotoxicity to the cells. Finally, bacteria adhesion and morphology were evaluated on the surfaces after 6 hrs and 24 hrs of incubation. From the results, it was confirmed that NT surfaces doped with Zn drastically reduced bacteria adhesion compared to the Ti control. Zn doped NT surfaces thus offered a potential platform for orthopedic implant application.

Every year, millions of people undergo surgeries that incorporate different orthopedic implants due to bone related injuries or diseases such as rheumatoid arthritis and osteosarcoma. For these patients, undergoing implant surgery is one of the crucial treatment choices to maintain the quality of life [2]. Although implants can be made of metals, ceramic, polymers, or composites, around 70-80% of all implant materials are metallic made from cobalt-chromium (CoCr) alloys, stainless steel (SS), and titanium (Ti) alloys [3]. Compared to the CoCr alloys and SS, Ti alloys are reported to be advantageous due to improved corrosion resistance, low modulus of elasticity, and biocompatibility [4]. Therefore, a huge amount of (around 1000 tons) Ti alloy implants are inserted in patients annually around the world [3]. However, around 10% of these implants fail each year resulting in revision surgeries and expensive medications throughout the rest of the patient's lifetime [5]. One of the major reasons of orthopedic implant failures is pathogenic infection caused by bacteria resulting in osteomyelitis. Bacteria can get attached to the implant surfaces and once in the body can proliferate, leading to biofilm formation and subsequent failure of the implant [6]. Osteomyelitis can lead to devastating consequences for the patients such as sepsis and prolonged hospitalization [7]. Along with osteomyelitis, another major complication of orthopedic implant is poor osseointegration [5, 8-9]. Osseointegration deals with anchorage of implant by forming bone tissue around it without growing any fibrous tissue [10]. A successful osseointegration deals with many facts including the biocompatibility, macroscopic, and

microscopic surface properties of the implant along with undisturbed healing process of the bone [11]. In the USA, around 1.2 million orthopedic implants are inserted in patients annually, of which 112,000 are projected to fail [12]. Complications and failure related to the implants also create a huge economic toll on the society. It was estimated that implant related medical costs climbs up to $3 billion annually in the USA [8]. With an increasingly mobile human population, the number of bone related injuries will increase along with the number of patients having orthopedic implants. This can result in a higher amount of implant failures. The economic burden and human suffering from pain related to complicated treatment procedures and repeated surgeries will also result from such higher number of implant failures.

There have been numerous research works to improve osseointegration and reduce bacteria adhesion on the implant surfaces. The two major approaches for reducing bacterial adhesion while improving cell adhesion comprises of surface coatings and surface modifications [13]. Modifications of implant surfaces such as the introduction of nanoscale surface characteristics have been reported to be effective in osteogenic cellular interaction and reducing bacterial adhesion on the surfaces. One popular approach of surface modification is a combination of grid-blasting and acid-etching. Pits and spike like nanostructures are created on the surfaces by this modification technique that showed improved osseointegration [14-16, 17, 18]. Other methods of surface modification include chemical vapor deposition, sol-gel coatings, hydrothermal treatment, glow discharge plasma treatment, and ion implantation [19-20]. The major focus of these Ti surface modifications is to improve osseointegration to help in orthopedic disease treatment by Ti based implants. It has been reported that increased hydrophilicity of the surfaces also helps in early osseointegration [21]. One of the quick, convenient, inexpensive, and highly tunable methods of preparing a super-hydrophilic Ti surface is by producing TiO_2 nanotube arrays (NT) by anodization

[20]. NT surfaces have shown cell adhesion to the implant surfaces that results in improved osseointegration [14, 22-24]. Interestingly, NT surfaces also exhibit improved antibacterial activity [13, 25]. This is a useful characteristic of the NT surfaces because they can promote osseointegration while reducing bacterial adhesion. This can provide the necessary biocompatibility to the orthopedic implant. Another interesting fact about NT surfaces is that their tubular structures can be used as a delivery mechanism for antibiotics [26], antibacterial substances [27], and trace elements that are useful for cell growth and proliferation [8].

Trace elements such as silver (Ag) nanoparticles, copper (Cu), strontium (Sr) and zinc (Zn) are critical for cell growth and proliferation around an implant surface that can improve osseointegration. Besides, they can also hinder bacterial infection on the implant surfaces. For that reason, the incorporation of trace elements on implant surfaces is gaining popularity. Also, metal ion release can be a viable technique to improve the antibacterial property of biomaterials [28]. Among the trace elements, Zn is interesting because it can provide required cell signaling for improved osseointegration while hindering bacterial adhesion on the implant surface [8]. Zn helps in bone regeneration by osteoblast activity such as osteoblast proliferation, mineralization, and osteoblast marker gene expression [8]. Zn also inhibits bone resorption by reducing osteoclast formation as well as helps in anti-inflammation [8]. For these interesting characteristics, Zn has gained popularity in preparing biomaterials. Recent work utilized several techniques to dope Zn on Ti surfaces. These techniques involved hydrothermal treatment [8-9, 29-30], alkaline-heat treatment [31-32], and plasma electrolytic oxidation (PEO) [33-34]. Even though Zn incorporation on implant surfaces can potentially improve the biocompatibility of orthopedic implants, only a few investigations have been reported in the literature. Therefore, examining the trace element

incorporation on orthopedic implant surfaces along with their antibacterial and toxicological behavior analysis is imperative.

In this work, Zn doping was conducted on Ti and NT surfaces using two different methods: hydrothermal and alkaline-heat treatment. These two processes were selected because they are relatively simple and highly tunable. For the hydrothermal method, the surfaces were incubated with zinc acetate. For the alkaline-heat treatment the surfaces were incubated with a solution containing zinc nitrate hexahydrate and sodium hydroxide. The difference between these two methods was mainly in treatment temperature and time. Hydrothermal method used 200°C and 1 hr treatment time, whereas alkaline heat treatment was conducted for 24 hrs at 60°C. All the treated surfaces were annealed at 530°C to crystallize the Zn and NTs. Scanning electron microscopy (SEM) and Energy-dispersive X-ray spectroscopy (EDS) were used to understand the morphology, topography, and Zn distribution on the surfaces. X-ray photoelectron spectroscopy (XPS) and X-ray diffraction (XRD) crystallography were used to evaluate surface chemistry and crystalline structure. XPS was also used to quantify Zn on the surfaces. Cytotoxic behavior was analyzed by incubating the surfaces with adipose derived human stem cells (ADSCs) and examining the amount of lactate dehydrogenase (LDH) released from the cells when in contact with the surfaces. Finally, the antibacterial properties of the surfaces were evaluated by incubating the surfaces with Gram-positive *Staphylococcus aureus* and Gram-negative *Pseudomonas aeruginosa*. SEM and live/dead bacteria staining were used to examine bacteria adhesion and morphology on the surfaces. Experimental results indicated that the Zn doped surfaces exhibited improved biocompatibility by reducing the bacteria adhesion significantly while not being cytotoxic to the ADSCs.

2.2 Materials and methods

2.2.1 Titania nanotube (NT) fabrication

Titania nanotube (NT) surfaces were fabricated from commercially available 0.5 mm thick pure titanium. First, 2 cm X 2 cm Ti samples were cut and polished using silicon carbide sheets. Then, the samples were soaked in acetone for 3 mins and sonicated for 10 mins to clean any debris from the surface. The samples were further cleaned using soap and iso-propanol followed by 10 mins sonication each in iso-propanol and de-ionized water (DI). Finally, the cleaned Ti samples were dried inside a hood before subsequent processing. NT were grown on the surfaces by anodization and annealing. An electrolyte cell was used for the anodization process where cleaned titanium surface was used as anode and platinum was used as cathode. Prior to the anodization process, the platinum surfaces were cleaned thoroughly using nitric acid, iso-propanol, and DI water. A solution containing 95% diethylene glycol (DEG), 2% hydrofluoric acid (HF, 48%), and 3% DI water was used as electrolyte. Titanium anode and platinum cathode were hooked to the electrolyte cell using alligator tips. Care was taken when hooking the samples so that the alligator tips do not touch the electrolyte solution. Then, 55 V electricity was supplied for 22 hrs at room temperature for the anodization process. After the anodization process, NT surfaces were removed and washed using DI water and iso-propanol before drying inside a hood. Finally, the NT surfaces were annealed at 530°C for 3 hrs with 15°C/min temperature increment and stored before using for subsequent experiments. Cleaned and polished titanium (Ti) was also prepared to be used as a control.

2.2.2 Zinc doping on Ti and NT surfaces

Zinc (Zn) doping on Ti and NT surfaces was done by two different methods: hydrothermal and alkaline-heat treatment. To prepare hydrothermally Zn doped NT surfaces (NThyt), un-annealed NT surfaces were used. These surfaces were incubated in 0.1 M zinc acetate solution at 200°C for 1 hr inside a polytetrafluoroethylene (PTFE) lined hydrothermal autoclave reactor. The surfaces were taken out from the reactor and thoroughly washed in DI water for 5 min. Finally, the surfaces were annealed similarly as described in section 2.1 prior to storing for subsequent experiments.

To prepare alkaline heat-treated NT surfaces (NT_{alk}), un-annealed NT surfaces were used. These surfaces were incubated in 10.71% zinc nitrate hexahydrate, 17.31% sodium hydroxide, and 71.98% DI water solution at 60°C for 24 hrs inside a PTFE container. The surfaces were taken out from the reactor and thoroughly washed in DI water for 5 min. Finally, the surfaces were annealed similarly as described in section 2.1 prior to storing for subsequent experiments.

Ti surfaces were also treated in a similar way to prepare hydrothermally treated Ti_{hyt} and alkaline heat-treated Ti_{alk} surfaces.

2.2.3 Material characterization

To understand the morphological and topographical characteristics of different surfaces (Ti, Ti_{hyt}, Ti_{alk}, NT, NT_{hyt}, NT_{alk}), a JEOL JSM-6500F field emission scanning electron microscope (FESEM) was used at 15 kV. Scanning electron microscopic (SEM) images were taken from each surface at varying magnifications ranging from 500x to 30000x. Working distance, brightness and contrast were optimized for each image to ensure high quality of SEM images of the surfaces. Further, energy-dispersive X-ray spectroscopy (EDS) spectra were collected with an Oxford SDD

EDS detector connected to the FESEM. For each surface, element mapping was done to understand elemental distribution on the surfaces. For NT_{hyt}, NT_{alk}, Ti_{hyt}, and Ti_{alk} surfaces, elemental mapping was also conducted in specific zones to understand special features on the surfaces. All EDS data were analyzed using Oxford Aztec software.

To understand the surface wettability, static contact angle was measured for all the surfaces by using a Ramé-Hart goniometer. A 10 µl drop of water was placed on each surface using a micrometer syringe. Then static contact angle and image of the droplet on the surfaces were collected using DROPimage software.

To understand the surface chemistry, X-ray photoelectron spectroscopy (XPS) was utilized. XPS survey was taken by PHI Physical Electronics PE-5800 X-ray Photoelectron Spectrometer with an Al Kα x-ray source. Survey spectra for all the surfaces were collected from 0 eV to 1100 eV. Peak-fit analysis was conducted using MultiPak. From the survey spectra, elemental analysis was also conducted for each surface using the MultiPak and the composition (atomic weight percentage, %at) of each element was recorded.

Crystalline structure of the surfaces was analyzed by utilizing X-ray diffraction (XRD, XRD-7000 Shimadzu) while using CuKα radiation at 40 kV and 30 mA. When performing XRD, a thin film (TF-XRD) geometry was utilized for the surfaces with a fixed incidence angle of 5°. Diffractograms were acquired with continuous scan from 20 to 80° at a scanning speed of 1°/min. Peaks were indexed using the Match! software with the PDF2 database.

2.2.4 Stability of Zn doped surfaces

To understand stability of the Zn doped surfaces, elemental analysis from XPS survey scan was used. 2 cm X 2 cm surfaces were collected and incubated in DI water for 4 weeks (28 days)

at room temperature. Then the surfaces were dried inside a hood and XPS surveys were taken following the method described in **section 2.3**. From these survey scans, %at was calculated for each of the surfaces. Finally, the %at of the elements after 4 weeks was compared with data gathered in **section 2.3** to evaluate the changes in Zn composition after 28 days in DI water.

2.2.5 Mechanical properties of the surfaces

To understand the mechanical properties such as surface hardness and elastic modulus, the nanoindentation technique was utilized. A Nanoindenter (ZwicK-Roell/ Asmec) was used to measure the surface hardness (H) and elastic modulus (E). It was programmed by an array (5 x 5), with 50 µm of distance between each indentation and 0.1 N of maximum applied force on the surface by a calibrated Berkovich tip. The indentation method used was Quasi Continuous Stiffness Measurement (QCSM). This method allows to get high accuracy measurements due to a progressive increasing force (from 0 – 100mN for this study) combined with a dwell time at each force point.

2.2.6 Cytotoxicity behavior of the surfaces

To evaluate the cytotoxicity induced by the surfaces, a lactate dehydrogenase (LDH) based indicator assay was utilized (CyQUANT^{TM} LDH Cytotoxicity Assay Kit). The cytotoxicity of the surfaces was evaluated with adipose derived adult stem cells (ADSCs). The ADSCs were cultured in a growth medium containing 90% MEM Alpha Modification (1x, cytiva), 9% fetal bovine serum (FBS), and 1% penicillin-streptomycin. The surfaces were taken into a 48-well plate and sterilized by UV light for 1 hr followed by washing with PBS for two times. After that, the surfaces were incubated for 24 hrs at 5% CO_2 with 20000 ADSC cells/ml. After the incubation, 50 µl supernatants

of the cell media were taken from each surface in a sterile 96 well plate. Then the manufacturer's protocol was followed to determine the cytotoxicity induced by the surfaces against the ADSCs.

2.2.7 Bacteria culture

To evaluate the antibacterial properties of different surfaces, Gram-positive *Staphylococcus aureus* (*S. aureus*, ATCC6538) and Gram-negative *Pseudomonas aeruginosa* (*P. aeruginosa*, ATCC10145) bacterial strains were used. Both bacteria were grown in tryptic soy broth (TSB, Sigma Aldrich) at 37°C for 24 hrs until a bacterial concentration of 10^9 Colony Forming Units (CFU)/ml was achieved. The CFU/ml was measured by determining the absorbance values of bacterial solution using a plate reader at 562 nm wavelength. To understand the bacteria adhesion and morphology on the surfaces, a diluted bacteria culture of 10^6 CFU/ml was used. The surfaces were taken into a 48-well plate and sterilized by UV light for 30 mins and subsequently washed twice with PBS for 5 mins. Then the surfaces were incubated with the 10^6 CFU/mL bacteria solution for 6 hrs and 24 hrs at 37°C inside an incubator. After the incubation, the surfaces were washed twice with PBS for 5 mins to remove any non-adhered bacteria from the surfaces before subsequent characterization.

2.2.7.1 Bacteria adhesion on different surfaces

For evaluating the number of live or dead bacteria adhered on different surfaces, a fluorescence microscope was used. For this, the surfaces were incubated at room temperature for 15 mins in a stain solution containing a 1:1 ratio of propidium iodide (dead bacteria stain) and Syto 9 (live bacterial stain) (3 µl/ml in PBS, Invitrogen). Then, the stain solution was removed, and the surfaces were incubated with 3.7% formaldehyde for 15 mins at room temperature. After that, the

formaldehyde was removed, and the surfaces were rinsed with PBS twice for 5 mins. Immediately after that, the surfaces were imaged using a fluorescence microscope. ImageJ was used to evaluate the percentage of area fraction covered by the live or dead bacteria on the surfaces. From staining to imaging, all the procedures were conducted in dark.

2.2.7.2 Bacteria morphology on different surfaces

To characterize adhered bacteria morphology on different surfaces, SEM images were collected for each surface after incubating with bacteria. After bacteria incubation, the surfaces were incubated with a primary fixative solution containing 3% glutaraldehyde, 0.1 M sucrose, and 0.1 M sodium cacodylate in DI water for 45 mins at room temperature. Then the fixative solution was removed, and the surfaces were incubated with a buffer solution containing the fixative solution without the glutaraldehyde for 10 mins. Finally, the surfaces were dehydrated using 35%, 50%, 70%, and 100% ethanol solution (10 mins incubation in each solution). Before imaging with SEM, the surfaces were kept dry inside a desiccator. Right before loading the surfaces in the SEM instrument, a 10 nm gold coating was done by using Denton Vacuum Desk II Gold Sputter Coater to improve surface conductivity for imaging.

2.2.8 Statistical analysis

For surface characterization, at least 3 samples (n_{min} = 3) of each surface were used. To evaluate the cytotoxicity, at least 4 samples (n_{min} = 4) of each surface were incubated with ADSCs. For antibacterial activity studies, 3 samples from each surface were used and all the experiments were repeated at least twice (n_{min}= 6). For statistical analysis, a two-way analysis of variance test

(ANOVA) was conducted followed by a post-hoc analysis (t-test). The results were considered statistically significant when *p* value was less than 0.05.

2.3 Results and discussion

2.3.1. Morphology and Zn distribution on the surfaces

Morphological and topographical features of the Ti and NT surfaces were characterized by SEM images. The morphological features on the surfaces are important for biomaterials since they can affect cell and bacteria adhesion on surfaces. Surface properties, such as roughness, have been reported to improve cell adhesion and osseointegration [35,36]. Titania nanotube array (NT) and Zn incorporation can effectively change the morphological properties of the surfaces due to treatments utilizing different chemicals and temperature ranges. **Figure 2.1** shows the representative SEM images of different surfaces. The Zn-doped Ti_{hyt} and Ti_{alk} surfaces exhibited significant differences in the surface morphology. On the Ti_{hyt} surface, crystal-like structures were found relatively evenly distributed throughout the surface. This is significantly different from the Ti control surface where such crystal-like structures were absent. Thus, it was hypothesized that these crystals were Zn crystals formed due to the hydrothermal process, and this was further confirmed by EDS (discussed later). The Ti_{alk} surface exhibited a web-like structure. This is also significantly different compared to the Ti and Ti_{hyt} surfaces. Alvarez et al. (2009) performed an alkali heat treatment on Ti implants containing $[Zn(OH)4]2-$ complex and found a similar web-like structure, which they named a reticulated microporous structure [31]. Manivasagam and Popat (2020) also treated Ti implants with an alkali solution at 60 °C for 24 h and found a similar web-like structure [37]. So, the alkaline heat treatment in this study conformed to the reported literature. From the SEM images collected on NT surfaces, it was evident that the anodization and annealing

processes were successful in producing an evenly distributed NT array. The tubular geometrical shapes were distinctly visible on NT surfaces, which resemble the NT shapes described in the previously reported literature [5, 38-39]. The roughness of the implant surface is necessary to biomimic the bone microenvironment inside a human body. NT arrays can provide that required roughness, which can help in cell proliferation and viability. Moreover, the tubular-shaped geometry can hinder the growth of bacterial adhesion due to charge repulsion, bacteria membrane stretching by the NTs, and variations in surface roughness [13]. When these NT surfaces were doped with Zn, a similar trend to that of Ti_{hyt} and Ti_{alk} was observed. The NT_{hyt} surfaces were prepared by hydrothermal treatment and had a crystal-like structure on top of the NTs. The Zn crystals were also evenly distributed here but not as visible as the Ti_{hyt} because of the nanostructured surface architecture. Some of the Zn crystals were smaller than the diameter of the NTs and the space between the surrounding NTs. So, it is possible that some crystals filled up the space in these empty channels. For the alkaline heat-treated NT_{alk} surface, a familiar web-like structure was visible. The web was formed on top of the NTs and was evenly distributed throughout the surface. However, a new rod-shaped feature was found on the NT_{alk} surfaces which was absent on the Ti_{alk} surfaces. These features were probably arising from the sodium (Na) content in the alkaline (NaOH) solution used for Zn doping, which was later examined utilizing EDS. From the morphological analysis of the surfaces, it was evident that two Zn doping techniques initiated distinct morphological features on the surfaces compared to the pure Ti and NT controls.

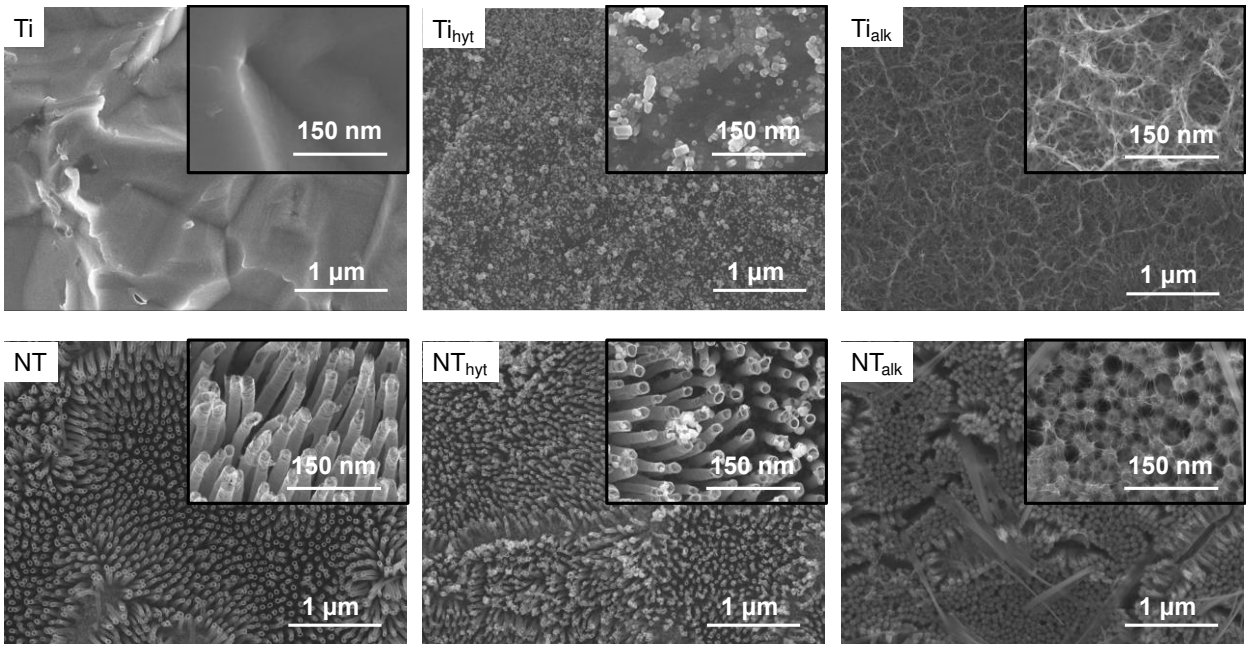

Figure 2.1. Representative SEM images of different surfaces at low (5000×) and high magnification (insert, 30,000×).

To understand the distribution of different elements on the surfaces, EDS mapping was conducted. The EDS mapping was especially helpful for understanding Zn-doping efficiency and the distribution of Zn throughout the surfaces. **Figure 2.2** shows representative EDS maps of NT_{hyt} and NT_{alk} surfaces. For the hydrothermally treated Ti_{hyt} and NT_{hyt} surfaces, although the Zn was evenly distributed, its concentration was much higher where the crystal-like structures were present. Hence, a higher magnification image was taken to understand the elemental composition of these crystal-like structures (**Figure 2.2**). The magnified EDS mapping indicated a higher concentration of Zn on these crystal-like structures, thus proving the crystals were indeed Zn crystals. For alkaline heat-treated surfaces (Ti_{alk} and NT_{alk}), Zn was found to be evenly distributed. Na distribution was also found for the alkaline heat-treated surfaces that might result from the residual NaOH used in the Zn-doping treatment. However, the distribution of Na from EDS mapping can be misleading since the characteristics X-ray released by these two elements are very

similar in energy level (Na, Kα = 1.04 eV and Zn, Lα = 1.012). Yet, the EDS spectra signaled the presence of Na on these surfaces, which was later confirmed utilizing XPS. A rod-shaped feature was found to be present on the NT_{alk} surface. High-magnification mapping was performed for these interesting features, which is shown in **Figure 2.2**. From the EDS mapping, it was found that these features mainly consisted of Zn, Na, and O. So, from the EDS mapping, it was understood that the web-like structure was mainly formed by the alkaline heat treatment of Zn and the rod-like features were formed by the Zn and excess Na on the surfaces. Na was also found to be present in Ti_{alk} surfaces; although, they did not create a rod-like feature on the surface. This interesting difference can result from the presence of NT arrays and their interaction with an alkaline solution during the alkaline heat treatment process.

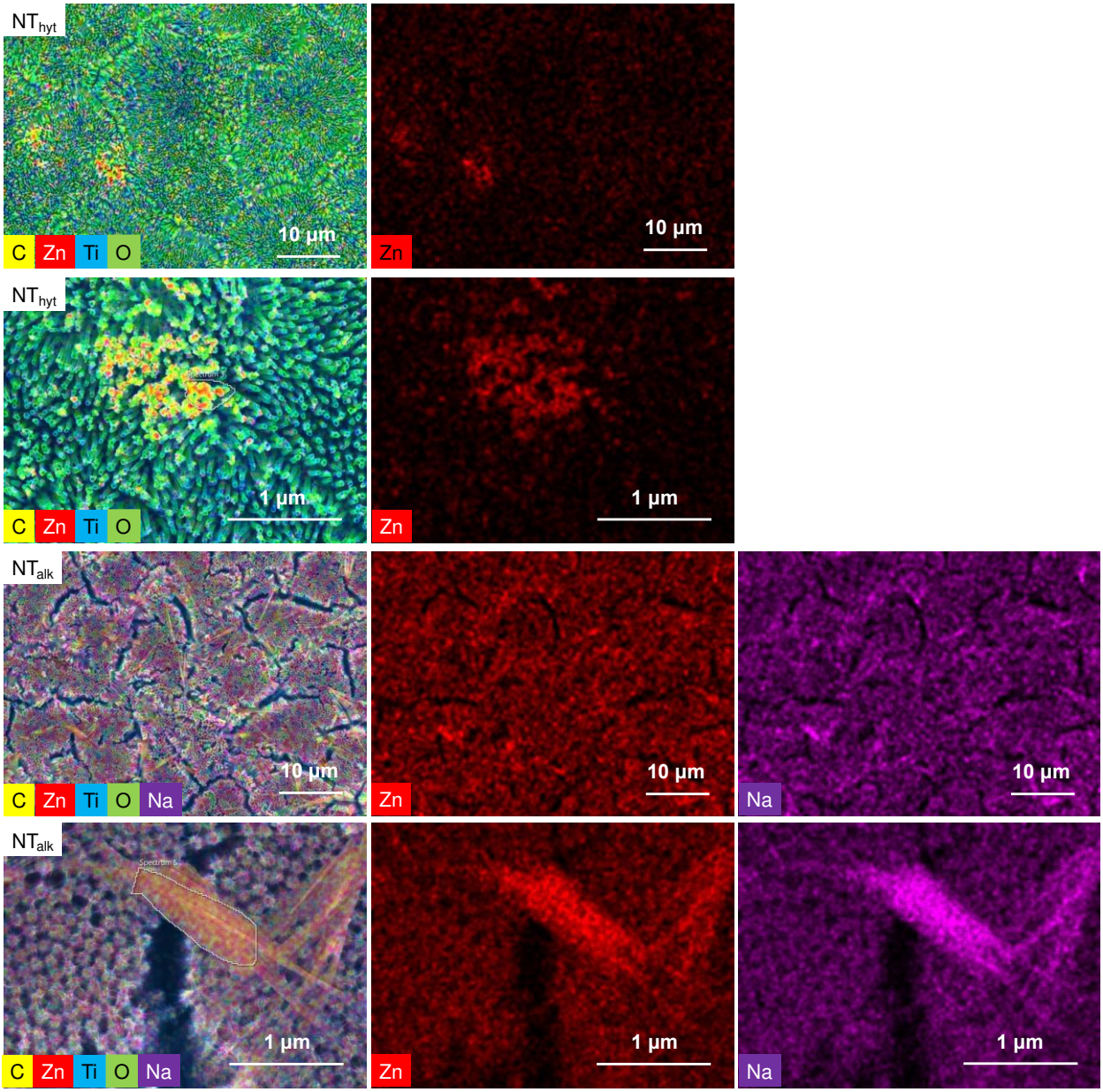

Figure 2.2. EDS analysis of representative surfaces NT_{hyt} and NT_{alk}. The top two rows show the EDS layered images of NT_{hyt} at different magnifications along with the Zn distribution. The bottom two rows show the EDS layered images of NT_{alk} at different magnifications along with Zn and Na distribution. White outlines in NT_{hyt} (2nd row) and NT_{alk} (4th row) is showing the crystal and rod-shaped features on the NT_{hyt} and NT_{alk} surfaces respectively.

2.3.2. Surface chemistry

The pure Ti surface underwent multiple surface modifications in this work to improve its biocompatibility. Hence, it is important to understand the chemical properties of the surfaces

before and after these modifications. Additionally, evaluating the surface chemistry is required to understand if the Zn doping was successful or not. As a first step, XPS survey scans were collected for all the surfaces. XPS survey scans can identify the elements present on the surfaces along with their relative concentration. From the survey scan of the Ti control, the presence of Ti2p3, C1s, and O1s was detected, which is typical of the Ti XPS spectrum reported in the previous literature [39]. However, after the Zn doping, both the Ti_{hyt} and Ti_{alk} exhibited a new peak at binding energy 1022 eV that corresponds to the presence of Zn2p3 on the surfaces (**Figure 2.3**). The prominence of this Zn2p3 peak was less in Ti_{alk} compared to the Ti_{hyt}, which indicated a lower amount of Zn presence on the alkaline-treated surfaces. However, Ti_{alk} exhibited another peak at binding energy 1071.4 eV corresponding to Na1s, which came from the NaOH used in the solution for alkaline heat treatment. The NT surface spectrum was similar to the Ti control, except for the high prominence of the O1s peak (530 eV) due to the presence of titania (TiO_2) on the surface. Like the Ti_{hyt} and Ti_{alk}, the Zn-doped NT_{hyt} and NT_{alk} surfaces also showed a new Zn2p3 peak (1022 eV), which was absent both in the Ti and NT surfaces, thus confirming the successful doping of Zn on the surfaces. Similar to the Ti_{alk}, the NT_{alk} also exhibited an Na peak (1071.4 eV) due to the presence of NaOH in an alkaline solution.

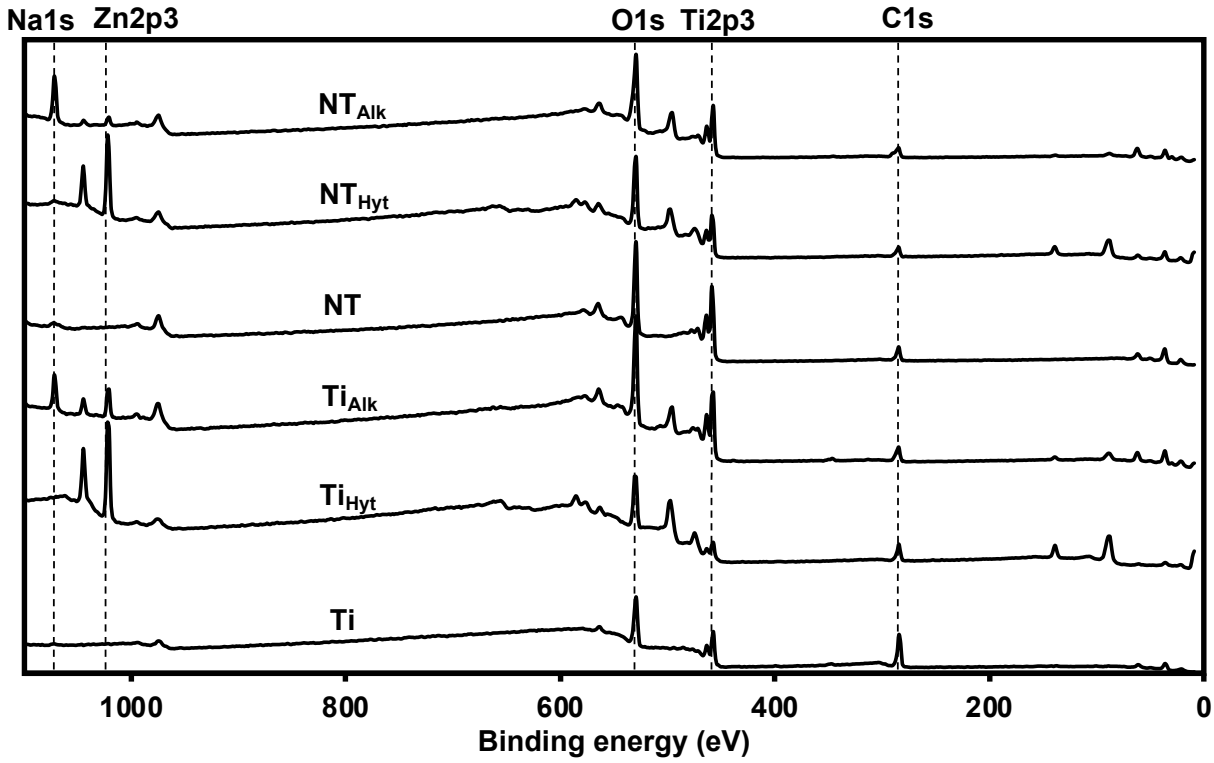

Figure 2.3. XPS survey spectra of different surfaces.

From the XPS survey scans, the elemental composition (atomic weight percentage, %at) of the surfaces was calculated (**Table 2.1**). Both Ti and NT showed no Zn or Na as expected. The %at of O increased from 34.7% to 57.3% between Ti and NT, indicating the presence of TiO_2 on the surface. Both the hydrothermally treated surfaces (Ti_{hyt} and NT_{hyt}) showed a higher amount of Zn compared to the alkaline heat-treated surfaces. The amount of Zn on Ti_{hyt} was higher (21.6%) compared to NT_{hyt} (16.9%), possibly due to the presence of a higher amount of O on NT_{hyt}. On the other hand, both alkaline heat-treated surfaces showed Na along with Zn. The amount of Na was higher in NT_{alk} (18.1%) compared to Ti_{alk} (9.8%), which probably affected the relative percentage of Zn (NT_{alk} 1.3% and Ti_{alk} 4.1%) on these surfaces.

Table 2.1. Elemental analysis (%at) of the surfaces from XPS survey spectra.

	% C	% O	% Ti	% Zn	% Na
Ti	55.6	34.7	9.7	0.0	0.0
Ti_{hyt}	29.7	42.8	5.9	21.6	0.0
Ti_{alk}	19.2	51.7	15.2	4.1	9.8
NT	21.3	57.3	21.4	0.0	0.0
NT_{hyt}	17.7	53.6	11.7	16.9	0.0
NT_{alk}	19.5	49.0	12.0	1.3	18.1

2.3.3. Surface crystallinity

Both the NT array preparation and Zn-doping techniques used higher temperatures, which can alter the crystalline phases of the surfaces. So, identifying these phases is important for this study. After anodization, NT arrays were amorphous, but after the annealing treatment at 530 °C, stable rutile and anatase crystalline structures were formed on the NT surfaces [36]. It is reported that the presence of rutile and anatase phases on the implant surface can help in osteogenic activity and osseointegration [40-42]. NT surfaces containing anatase and rutile phases also have been reported to possess antibacterial properties by reducing antibacterial adhesion on the surfaces [43-45]. In this work, all the NT surfaces showed a mixture of rutile and anatase phases (**Figure 2.4**). NT and NT_{hyt} surfaces had prominent anatase (25.27°, 48.01°, 53.91°) and rutile peaks (27.43°); however, these peaks were not as prominent in NT_{alk}, possibly due to the presence of web-like structure on top of the TiO_2 nanotubes. On the other hand, Ti control did not have any of these anatase or rutile phases. Ti_{hyt} and Ti_{alk} showed the stable rutile phase (27.43°) coming from the

high-temperature treatment for Zn doping. All the Zn-doped surfaces also showed a ZnO peak (31.73°), which confirmed the presence of Zn on the surfaces once again. Similar to the other peaks, the alkaline heat-treated surfaces showed less prominence of ZnO peak possibly due to the lower amount of Zn on the surfaces. Unmarked peaks in **Figure 2.4** correspond to Ti.

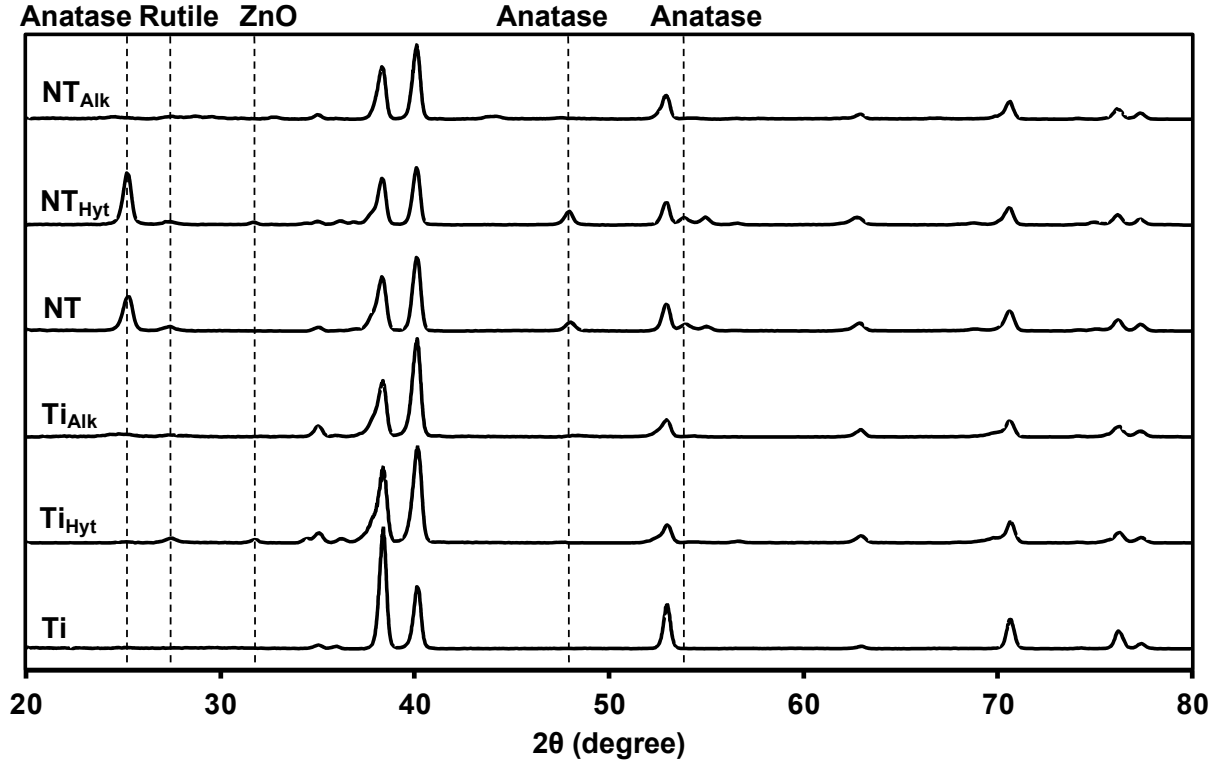

Figure 2.4. XRD spectra of different surfaces.

2.3.4. Surface stability

Surface stability is a key factor for biomaterials. Since implants are intended to stay inside the human body for a long period of time, it is important to understand the stability of the Zn-doped surfaces. The stability of the Zn-doped surfaces was evaluated up to 4 weeks (28 days) of incubation in DI water by taking an XPS survey scan and calculating surface elemental compositions (%at). **Table 2.2** shows the %at of Zn and Na before and after 28 days of incubation in DI water. After 4 weeks, there was a significant decrease in Zn for the hydrothermally treated

surfaces Ti_{hyt} and NT_{hyt}. Zn content in the Ti_{hyt} and NT_{hyt} reduced by almost 59% and 45%, respectively. Whereas the alkaline heat-treated samples Ti_{alk} and NT_{alk} showed a significant increase in Zn. However, this is not due to an increase in the Zn content on the surfaces, but rather a decrease In the Na content, which resulted in an Increase In the relative %at of Zn after 28 days. Since the surfaces were incubated in DI water, the Na might have been dissolved in water resulting in a significant decrease of Na on the surfaces after 28 days. The Ti control and NT surfaces did not show any change during this experiment.

Table 2. %at of Zn and Na on the surfaces measured from XPS elemental analysis on Day 0 and Day 28. The negative values in the %at change column indicate increased concentration after 28 days.

	% Zn			**% Na**		
	Day 0	**Day 28**	**% Change**	**Day 0**	**Day 28**	**% Change**
Ti	0.0	0.0	0.0	0.0	0.0	0.0
Ti_{hyt}	21.6	8.9	58.8	0.0	0.0	0.0
Ti_{alk}	4.1	5.2	−26.8	9.8	4.4	55.1
NT	0.0	0.0	0.0	0.0	0.0	0.0
NT_{hyt}	16.9	9.2	45.6	0.0	0.0	0.0
NT_{alk}	1.3	2.6	−100.0	18.1	0.0	100.0

2.3.5. Surface wettability

Surface wettability is another important surface characteristic of an implant's biocompatibility. Hydrophilic surfaces have been reported to promote cell adhesion and proliferation [46]. Hydrophilic surfaces can also reduce bacterial adhesion [44]. Surface wettability can be calculated by measuring the apparent static contact angle using a droplet of water on the surface. When the contact angle (θ) is lower than 90°, the surfaces are defined as hydrophilic, and when θ<10∘, then the surfaces are defined as superhydrophilic. All the treated surfaces in this work exhibited a significantly reduced contact angle compared to the Ti control. Ti, Ti_{hyt}, and NT_{hyt} were hydrophilic surfaces, whereas Ti_{alk}, NT, and NT_{alk} surfaces were superhydrophilic (**Figure 2.5**). All the surfaces except the Ti control were heat treated during annealing at 530 °C. During this heat treatment, the hydrophilic property of the surfaces increased, which matched the reported literature [44]. Thus, all the Zn-doped surfaces should potentially reduce bacterial adhesion and improve cell proliferation on the implant surfaces due to their superhydrophilic nature.

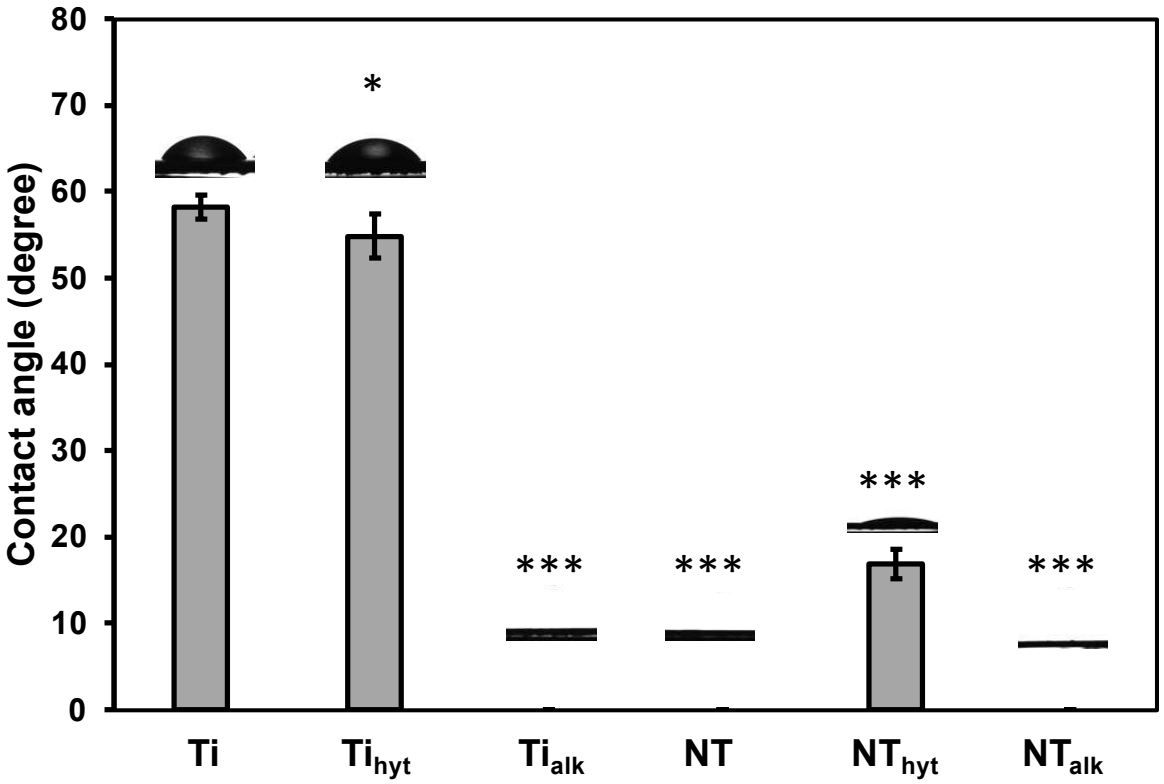

Figure 2.5. Static water contact angle of different surfaces. Images of water droplet on the surfaces are also shown in the plot. Statistical significances (*p*-value) were represented as * $p < 0.05$ and *** $p < 0.001$.

2.3.6. Mechanical properties

Mechanical properties such as material hardness, stiffness, and flexibility are important factors that determine cell-material interactions and ultimately cell fate on implant surfaces [47]. Several studies have reported that cells receive mechanical signaling from the surrounding microenvironment and prefer softer surfaces that promote cell adhesion on the material [47-50]. NT surfaces have nanoscale topographical features that can provide less restriction to deformation, resulting in a softer surface compared to an unmodified Ti surface [49]. To understand these mechanical properties, indentation hardness and elastic modulus of all the surfaces were evaluated using the nanoindentation technique. **Table 2.3** shows the hardness and elastic modulus values of

different surfaces. NT and NT_{hyt} showed the minimum hardness values of 0.32 ± 0.02 GPa and 0.26 ± 0.02 Gpa, respectively, whereas Ti control had a hardness value of 2.3 ± 0.4 GPa. The NT_{alk} exhibited a higher hardness value of 1.00 ± 0.2 GPa, which was higher than other NT surfaces, probably due to the presence of a web-like structure on top of the nanotubes as discussed in the morphological analysis. This web-like structure created a separate layer on the nanotubes and resulted in a higher restriction to deformation, which ultimately increased the hardness value. A similar result was observed for the Ti_{alk}, which exhibited a similar hardness value of 2.4 ± 0.2 GPa. Elastic modulus values also showed a similar trend to the hardness values (**Table 2.3**). All the NT surfaces exhibited lower elastic modulus compared to the Ti surfaces. This is an expected result due to the topographical differences of the Ti and NT surfaces that changed the restriction towards nanoindenter force.

Table 2.3. Indentation hardness and elastic modulus values for different surfaces.

	Indentation Hardness (GPa)	**Elastic Modulus (GPa)**
Ti	2.30 ± 0.4	138 ± 20
Ti_{hyt}	1.55 ± 0.08	94 ± 5
Ti_{alk}	2.40 ± 0.2	91 ± 20
NT	0.32 ± 0.02	23 ± 1
NT_{hyt}	0.26 ± 0.02	45 ± 4
NT_{alk}	1.00 ± 0.4	76 ± 20

2.3.7. Cytotoxicity of the surfaces

Cytotoxicity of different surfaces was determined using adipose-derived stem cells (ADSCs). The surfaces were incubated with ADSCs for 24 h before the lactate dehydrogenase (LDH) released by the damaged cells was calculated. A higher amount of LDH indicates a highly cytotoxic surface. The maximum release of LDH was calculated where all the cells were intentionally damaged to get the highest amount of LDH. A spontaneous release value was also calculated where no cells were damaged. When compared to these controls, all the surfaces showed no apparent cytotoxicity (**Figure 2.6**).

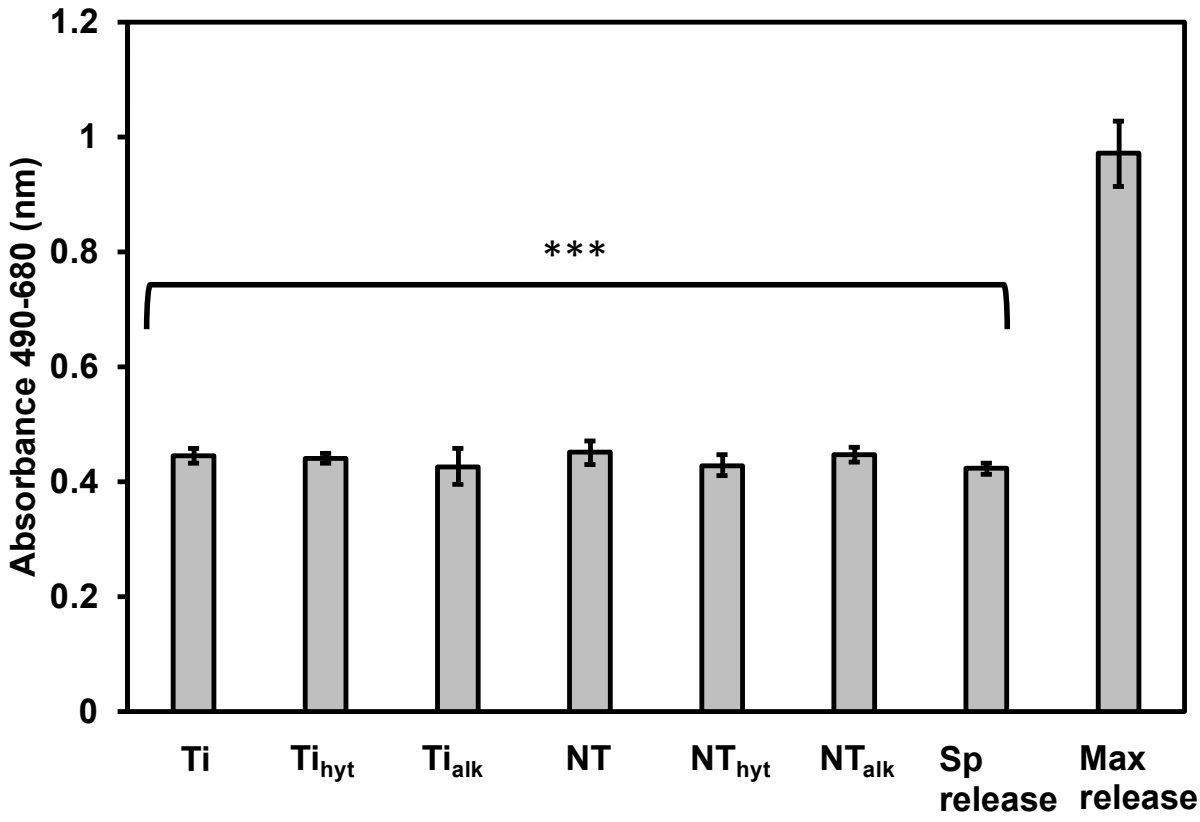

Figure 2.6. Cytotoxicity study of the surfaces against ADSCs. The values are represented as absorbance values at 490 and 680 nm. Sp release and Max release represent spontaneous and maximum LDH release values. *** represents p value < 0.001 when compared to the max release.

2.3.8. Bacteria adhesion

Bacterial infection is one of the major causes of orthopedic implant failure. Bacteria can attach to the implant surface and start to proliferate, forming biofilms that protect the bacteria colony from the surrounding immune response [13]. Most of the implant-related infections is caused mainly by the Gram-positive bacteria genus of Staphylococcus with *Staphylococcus aureus* (*S. aureus*) being a prominent infection-creating pathogen in this bacteria family [51-53]. Arciola et al. (2005) surveyed 1027 isolates from 699 patients undergoing revision orthopedic surgeries and found the majority of the infection was caused by *S. aureus* (35.5%) [51]. The second most prominent genus was Gram-negative Pseudomonas, with *Pseudomonas aeruginosa* (*P. aeruginosa*) being the most prominent infection-creating pathogen in this genus (6.7%) [51]. Even after maintaining a highly sterile environment during orthopedic implant surgeries, bacteria can still proliferate inside the host body [54]. Therefore, implants having antibacterial characteristics are a crucial step to reduce implant-related bacterial infection. To assess the antibacterial activity of the Zn-doped surfaces, all the surfaces were incubated for 6 h and 24 h with *P. aeruginosa* and *S. aureus*. Then live/dead bacteria staining was performed to evaluate the number of bacteria attached to each surface. **Figure 2.7** shows the fluorescence microscopic images of the surfaces after the incubation periods with *P. aeruginosa*. **Figure 2.7** also shows the two plots that quantified live and dead *P. aeruginosa* attached to different surfaces. Ti had the most bacteria attached to the surface for both 6 h and 24 h incubation periods. The Zn-doped Ti_{hyt} and Ti_{alk} had significantly lower P. *aeruginosa* attached to their surfaces. NT had lower *P. aeruginosa* attached to its surface when compared to the control Ti. All the Zn-doped surfaces reduced the *P. aeruginosa* attachment; however, the least reduction of bacteria attachment came from the NT_{hyt} surface. For instance, the area fraction % of Ti control by live *P. aeruginosa* after 6 h of incubation was 21.94%, whereas

NT_{hyt} was 6.1% (**Figure 2.7**). The hydrothermally treated NT_{hyt} surface had more Zn compared to the NT_{alk}. So, the number of bacteria attached to the NT_{hyt} was less than NT_{alk}.

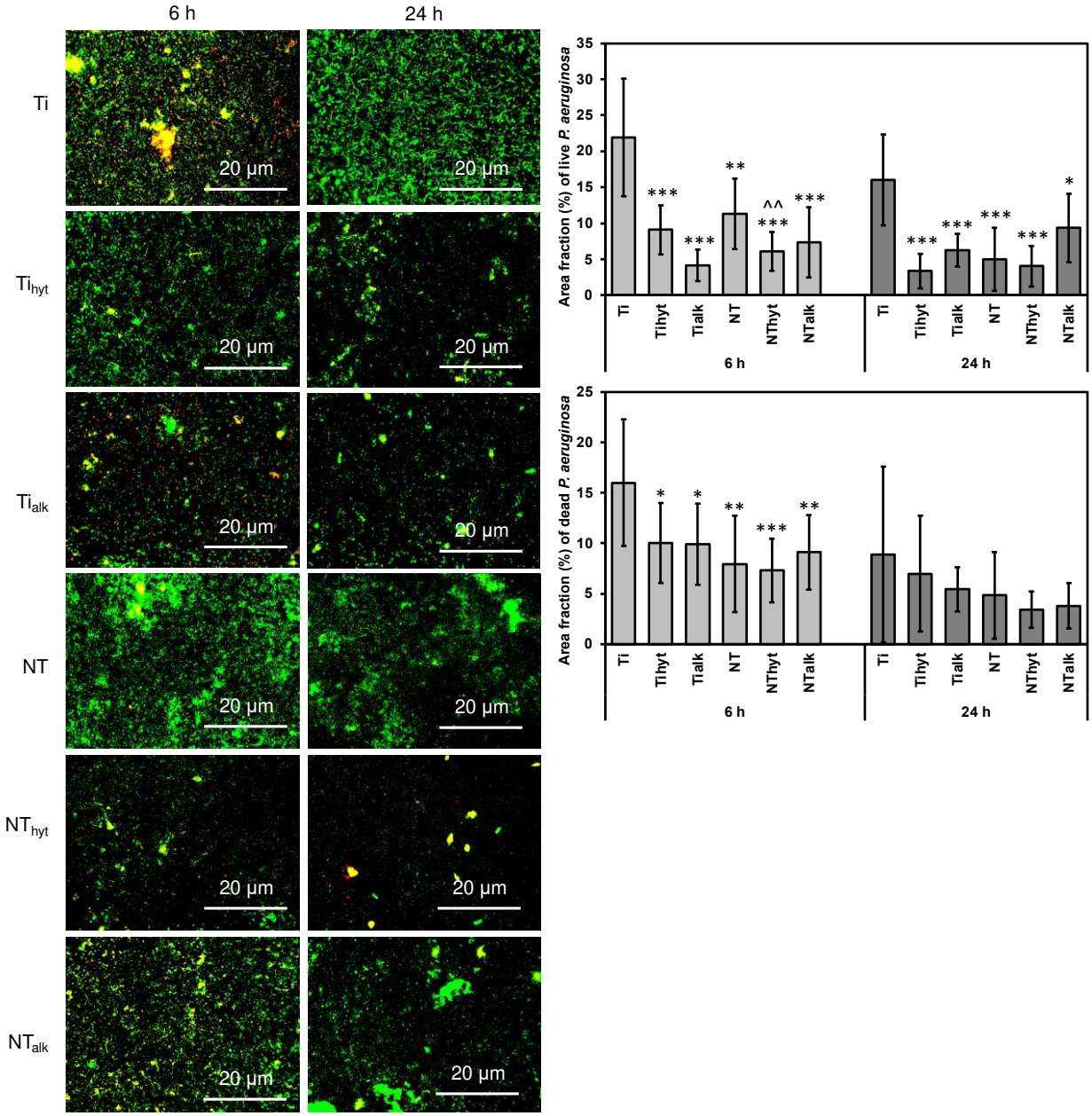

Figure 2.7. Representative fluorescence microscopic images of surfaces after incubation with *P. aeruginosa*. The graphs represent the number of live and dead *P. aeruginosa* attached to the surfaces. *, **, *** represent p-value < 0.05, <0.01, and <0.001 when compared with control Ti. ^^ represents p value < 0.01 when compared with NT.

Similar to *P. aeruginosa*, *S. aureus* attachment was also found to be low in Zn-doped surfaces compared to the control Ti. **Figure 2.8** shows the fluorescence microscopic images and quantified plots for *S. aureus* adhesion on the surfaces. After 6 h of incubation, both dead and live *S. aureus* adhesion were significantly reduced for Zn-doped Ti and NT surfaces compared to the Ti control. For instance, the area fraction % of Ti control by live *S. aureus* after 6 h of incubation was 41.95%, whereas NT_{hyt} and NT_{alk} were 23.73% and 11.58%, respectively (**Figure 2.8**). After 24 h of incubation, dead *S. aureus* reduction was also significantly reduced in the Zn-doped surfaces. Only in one case did the Ti control have better performance for live *S. aureus* reduction, which was after 24 h of incubation. All the Zn-doped surfaces also reduced *S. aureus* adhesion during this time; however, they were not significantly different from the Ti control.

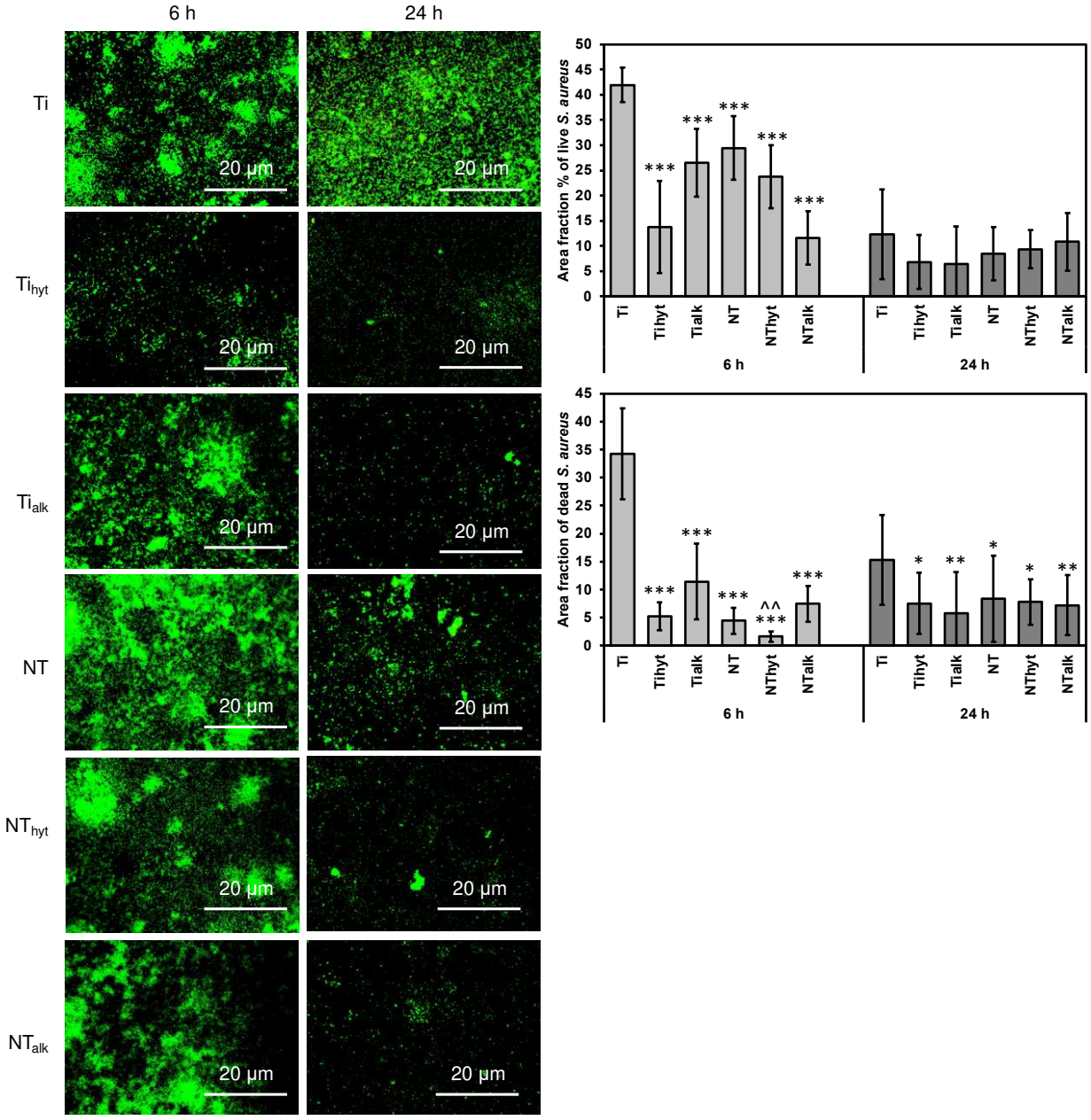

Figure 2.8. Representative fluorescence microscopic images of surfaces after incubation with *S. aureus*. The graphs represent the number of live and dead *S. aureus* attached to the surfaces. *, **, *** represent *p*-value < 0.05, <0.01, and <0.001 when compared with control Ti. ^^ represents *p* value < 0.01 when compared with NT.

2.3.9. Bacteria morphology

Morphological analysis of viable bacteria on the implant surfaces is important to understand how bacteria is attaching, proliferating, and forming biofilms. If bacteria can form a

biofilm on the surface, it can protect the bacteria from antibacterial agents and can proliferate until the implant fails. So, to understand bacteria morphology on the surfaces, SEM images were taken after the bacteria were fixed by using relevant adhesives. **Figure 2.9** shows the SEM images of the surfaces after 6 h and 24 h of *P. aeruginosa* incubation. Similar to the results described earlier, the Zn-doped surfaces reduced the *P. aeruginosa* attachment drastically. NT also reduced the *P. aeruginosa* on its surface; however, most reduction came from the NT_{hyt} and Ti_{hyt}. Both surfaces contained a higher amount of Zn compared to the NT_{alk} and Ti_{alk}, and hence, their antibacterial activity was improved. After 24 h of incubation, a biofilm formation could be seen on the Ti surface, which was absent on all the other surfaces. This finding confirmed the improved antibacterial activity of the Zn-doped surfaces.

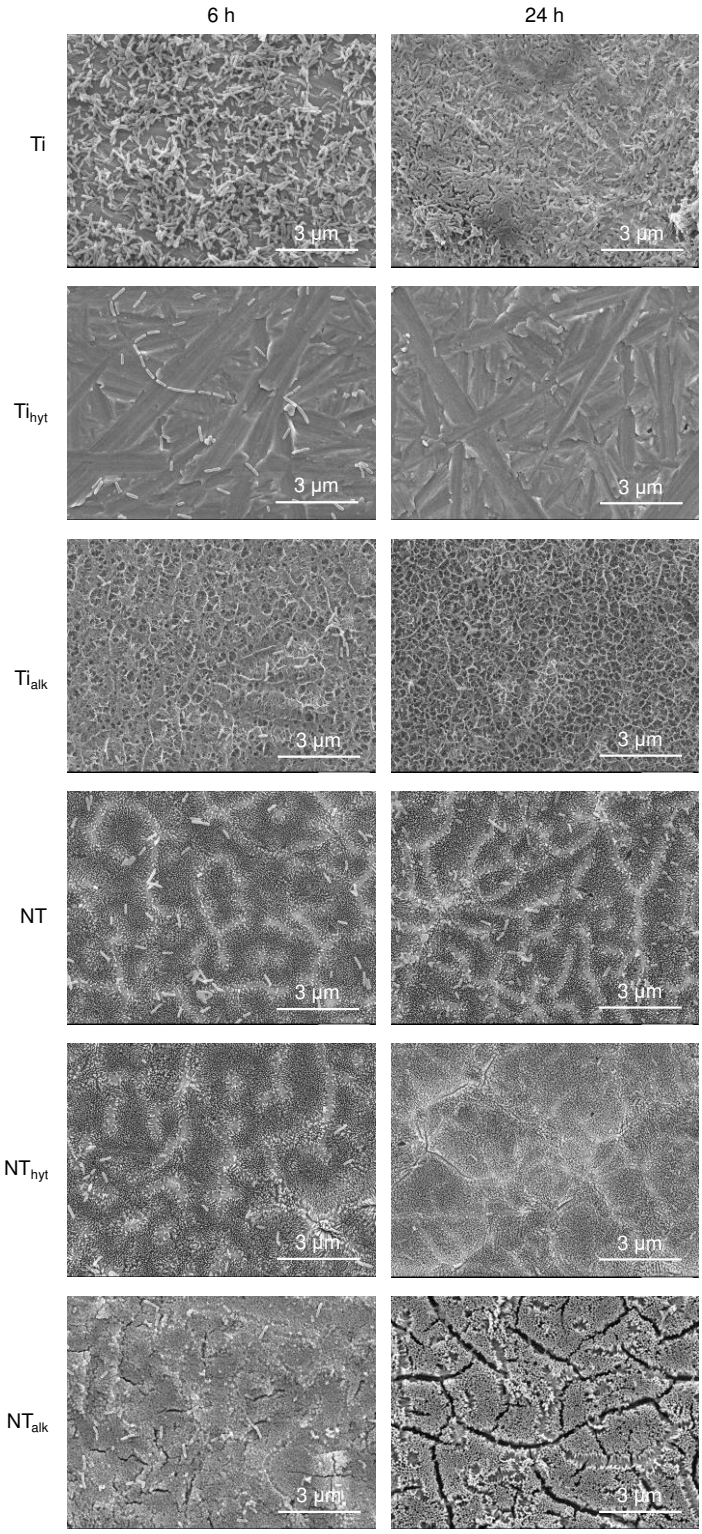

Figure 2.9. Representative SEM images of bacteria morphology after 6 h and 24 h of *P. aeruginosa* incubation.

A similar result was observed when the surfaces were incubated with Gram-positive *S. aureus* (**Figure 2.10**). Biofilm formation was also observed on the Ti surface after 24 h of incubation with *S. aureus*, which was absent in all other surfaces. All the Zn-doped surfaces reduced the amount of *S. aureus* adhesion; however, the Ti_{hyt} and NT_{hyt} performed well in this case due to the higher amount of Zn presence on the surfaces. When compared to *P. aeruginosa*, the *S. aureus* adhesion was higher for all the surfaces. This is probably due to the surface charge difference and size of the two bacteria tested. Although bacteria have an electronegatively charged outer layer, they can differ from Gram-positive to Gram-negative because of the difference in cell-wall composition [55]. Since the TiO_2 nanotube arrays have terminal hydroxyl groups which are negatively charged too, they repulse the bacteria and thus reduce bacteria adhesion on the NT surfaces [13]. For the differences in the electronegative charge between *P. aeruginosa* and *S. aureus*, the relative amount of antibacterial activity can differ, which was indicated in this case. Another important factor is the relative size of the two bacteria. *P. aeruginosa* is a rod-shaped bacterium having 1–5 μm of length and a 1 μm width [56]. On the other hand, *S. aureus* is a circular-shaped bacteria with a 1 μm diameter [57]. Due to this size difference, it is possible that the smaller *S. aureus* could evade the stretching force [13] induced by the NT arrays and resulted in more *S. aureus* attachment compared to *P. aeruginosa*.

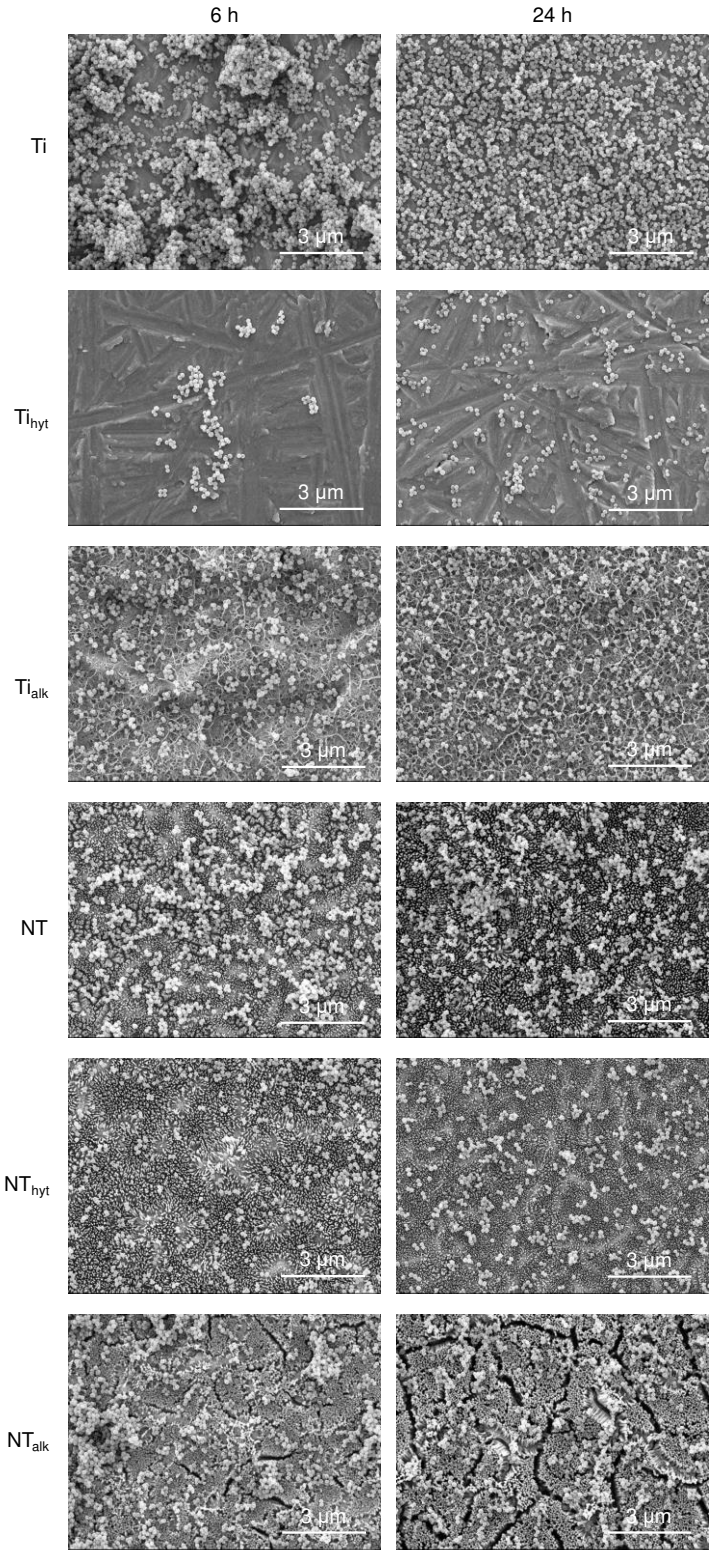

Figure 2.10. Representative SEM images of bacteria morphology after 6 h and 24 h of *S. aureus* incubation.

2.4 Conclusions

Nanoscale features on Ti surfaces can improve complications such as bacterial infection and poor osseointegration. In this work, titania (TiO_2) nanotube arrays (NT) were grown on pure Ti surfaces followed by zinc (Zn) doping. SEM images revealed noticeable morphological characteristics of the surfaces fabricated in this work. Hydrothermally treated Ti_{hyt} and NT_{hyt} surfaces had Zn crystals while the alkaline heat treatment created a web-like structure on the Ti_{alk} and NT_{alk} surfaces. EDS analysis indicated an even distribution of Zn on different surfaces. XPS confirmed the successful Zn doping on the surfaces while quantifying the amount of Zn. From the XPS, it was evident that hydrothermal treatment induced a higher amount of Zn on the surfaces. From the mechanical property analysis, it was found that the indentation hardness and elastic modulus of the nanotube surfaces (NT_{hyt} and NT_{alk}) were significantly lower than the Ti surfaces. This indicates a suitable platform for cell attachment, growth, and proliferation. While testing with bacteria, all the Zn-doped surfaces exhibited significantly improved antibacterial characteristics compared to the pure Ti. These results signified the greater potential of nanoscale surface modification approaches to improve the biocompatibility of Ti-based orthopedic implants.

REFERENCES

1. Bhattacharjee, A., Goodall, E., Pereira, B. L., Soares, P., & Popat, K. C. (2023). Zinc (Zn) Doping by Hydrothermal and Alkaline Heat-Treatment Methods on Titania Nanotube Arrays for Enhanced Antibacterial Activity. *Nanomaterials*, *13*(10), 1606.
2. Effenberger, H.; Ramsauer, T.; Böhm, G.; Hilzensauer, G.; Dorn, U.; Lintner, F. Successful hip arthroplasty using cementless titanium implants in rheumatoid arthritis. Arch. Orthop. Trauma Surg. 2002, 122, 80–87. https://doi.org/10.1007/s004020100320.
3. John, A.A.; Jaganathan, S.K.; Supriyanto, E.; Manikandan, A. Surface modification of titanium and its alloys for the enhance-ment of osseointegration in orthopaedics. Curr. Sci. 2016, 111, 1003–1015. Available online: https://www.jstor.org/stable/24908502 (accessed on 22 February 2023).
4. Taddei, E.; Henriques, V.; Silva, C.; Cairo, C. Production of new titanium alloy for orthopedic implants. Mater. Sci. Eng. C 2004, 24, 683–687. https://doi.org/10.1016/j.msec.2004.08.011.
5. Sabino, R.M.; Mondini, G.; Kipper, M.J.; Martins, A.F.; Popat, K.C. Tanfloc/heparin polyelectrolyte multilayers improve osteo-genic differentiation of adipose-derived stem cells on titania nanotube surfaces. Carbohydr. Polym. 2021, 251, 117079. https://doi.org/10.1016/j.carbpol.2020.117079.
6. Wang, M.; Tang, T. Surface treatment strategies to combat implant-related infection from the beginning. J. Orthop. Translat. 2019, 17, 42–54. https://doi.org/10.1016/j.jot.2018.09.001.
7. Lucke, M.; Schmidmaier, G.; Sadoni, S.; Wildemann, B.; Schiller, R.; Haas, N.; Raschke, M. Gentamicin coating of metallic im-plants reduces implant-related osteomyelitis in rats. Bone 2003, 32, 521–531. https://doi.org/10.1016/s8756-3282(03)00050-4.

8. Huo, K.; Zhang, X.; Wang, H.; Zhao, L.; Liu, X.; Chu, P.K. Osteogenic activity and antibacterial effects on titanium surfaces modified with Zn-incorporated nanotube arrays. Biomaterials 2013, 34, 3467–3478. https://doi.org/10.1016/j.biomaterials.2013.01.071.
9. Li, Y.; Xiong, W.; Zhang, C.; Gao, B.; Guan, H.; Cheng, H.; Fu, J.; Li, F. Enhanced osseointegration and antibacterial action of zinc-loaded titania-nanotube-coated titanium substrates: In vitro and in vivo studies. J. Biomed. Mater. Res. Part A 2014, 102, 3939–3950. https://doi.org/10.1002/jbm.a.35060.
10. Albrektsson, T.; Johansson, C. Osteoinduction, osteoconduction and osseointegration. Eur. Spine J. 2001, 10, S96–S101. https://doi.org/10.1007/s005860100282.
11. Parithimarkalaignan, S.; Padmanabhan, T.V. Osseointegration: An update. J. Indian Prosthodont. Soc. 2013, 13, 2–6. https://doi.org/10.1007/s13191-013-0252-z.
12. Darouiche, R.O. Treatment of infections associated with surgical implants. N. Engl. J. Med. 2004, 350, 1422–1429. https://doi.org/10.1056/nejmra035415.
13. Li, Y.; Yang, Y.; Li, R.; Tang, X.; Guo, D.; Qing, Y.; Qin, Y. Enhanced antibacterial properties of orthopedic implants by titanium nanotube surface modification: A review of current techniques. Int. J. Nanomed. 2019, 14, 7217–7236. https://doi.org/10.2147/ijn.s216175.
14. Souza, J.C.M.; Sordi, M.B.; Kanazawa, M.; Ravindran, S.; Henriques, B.; Silva, F.S.; Aparicio, C.; Cooper, L.F. Nano-scale modi-fication of titanium implant surfaces to enhance osseointegration. Acta Biomater. 2019, 94, 112–131. https://doi.org/10.1016/j.actbio.2019.05.045.
15. Uggeri, J.; Guizzardi, S.; Scandroglio, R.; Gatti, R. Adhesion of human osteoblasts to titanium: A morpho-functional analysis with confocal microscopy. Micron 2010, 41, 210–219. https://doi.org/10.1016/j.micron.2009.10.013.

16. Ziebart, T.; Schnell, A.; Walter, C.; Kämmerer, P.W.; Pabst, A.; Lehmann, K.M.; Ziebart, J.; Klein, M.O.; Al-Nawas, B. Interac-tions between endothelial progenitor cells (EPC) and titanium implant surfaces. Clin. Oral Investig. 2013, 17, 301–309. https://doi.org/10.1007/s00784-012-0691-7.
17. Stich, T.; Alagboso, F.; Křenek, T.; Kovářík, T.; Alt, V.; Docheva, D. Implant-bone-interface: Reviewing the impact of titanium surface modifications on osteogenic processes in vitro and in vivo. Bioeng. Transl. Med. 2021, 7, e10239. https://doi.org/10.1002/btm2.10239.
18. Jiang, P.; Zhang, Y.; Hu, R.; Shi, B.; Zhang, L.; Huang, Q.; Yang, Y.; Tang, P.; Lin, C. Advanced surface engineering of titanium materials for biomedical applications: From static modification to dynamic responsive regulation. Bioact. Mater. 2023, 27, 15–57. https://doi.org/10.1016/j.bioactmat.2023.03.006.
19. Liu, X.; Chu, P.K.; Ding, C. Surface modification of titanium, titanium alloys, and related materials for biomedical applica-tions. Mater. Sci. Eng. R Rep. 2004, 47, 49–121. https://doi.org/10.1016/j.mser.2004.11.001.
20. Manivasagam, V.K.; Sabino, R.M.; Kantam, P.; Popat, K.C. Surface modification strategies to improve titanium hemocompat-ibility: A comprehensive review. Mater. Adv. 2021, 2, 5824–5842. https://doi.org/10.1039/d1ma00367d.
21. Lang, N.P.; Salvi, G.E.; Huynh-Ba, G.; Ivanovski, S.; Donos, N.; Bosshardt, D.D. Early osseointegration to hydrophilic and hy-drophobic implant surfaces in humans. Clin. Oral Implant. Res. 2011, 22, 349–356. https://doi.org/10.1111/j.1600-0501.2011.02172.x.
22. Park, J.; Bauer, S.; von der Mark, K.; Schmuki, P. Nanosize and vitality: TiO_2 nanotube diameter directs cell fate. Nano Lett. 2007, 7, 1686–1691. https://doi.org/10.1021/nl070678d.

23. Park, J.; Bauer, S.; Schlegel, K.A.; Neukam, F.W.; von der Mark, K.; Schmuki, P. TiO_2 nanotube surfaces: 15 nm-an optimal length scale of surface topography for cell adhesion and differentiation. Small 2009, 5, 666–671. https://doi.org/10.1002/smll.200801476.

24. von Wilmowsky, C.; Bauer, S.; Roedl, S.; Neukam, F.W.; Schmuki, P.; Schlegel, K.A. The diameter of anodic TiO_2 nanotubes affects bone formation and correlates with the bone morphogenetic protein-2 expression in vivo. Clin. Oral Implants Res. 2012, 23, 359–366. https://doi.org/10.1111/j.1600-0501.2010.02139.x.

25. Simi, V.; Rajendran, N. Influence of tunable diameter on the electrochemical behavior and antibacterial activity of titania nanotube arrays for biomedical applications. Mater. Charact. 2017, 129, 67–79. https://doi.org/10.1016/j.matchar.2017.04.019.

26. Feng, W.; Geng, Z.; Li, Z.; Cui, Z.; Zhu, S.; Liang, Y.; Liu, Y.; Wang, R.; Yang, X. Controlled release behaviour and antibacterial effects of antibiotic-loaded titania nanotubes. Mater. Sci. Eng. C 2016, 62, 105–112. https://doi.org/10.1016/j.msec.2016.01.046.

27. Mei, S.; Wang, H.; Wang, W.; Tong, L.; Pan, H.; Ruan, C.; Ma, Q.; Liu, M.; Yang, H.; Zhang, L.; et al. Antibacterial effects and bio-compatibility of titanium surfaces with graded silver incorporation in titania nanotubes. Biomaterials 2014, 35, 4255–4265. https://doi.org/10.1016/j.biomaterials.2014.02.005.

28. Yougbaré, S.; Mutalik, C.; Okoro, G.; Lin, I.-H.; Krisnawati, D.I.; Jazidie, A.; Nuh, M.; Chang, C.-C.; Kuo, T.-R. Emerging trends in nanomaterials for antibacterial applications. Int. J. Nanomed. 2021, 16, 5831–5867. https://doi.org/10.2147%2FIJN.S328767.

29. Cheng, H.; Mao, L.; Wang, L.; Hu, H.; Chen, Y.; Gong, Z.; Wang, C.; Chen, J.; Li, R.; Zhu, Z. Bidirectional regulation of zinc em-bedded titania nanorods: Antibiosis and osteoblastic cell growth. RSC Adv. 2015, 5, 14470–14481. https://doi.org/10.1039/C4RA17058J.

30. Nageri, M.; Kalarivalappil, V.; Vijayan, B.K.; Kumar, V. Titania nanotube arrays surface-modified with ZnO for enhanced photocatalytic applications. Mater. Res. Bull. 2016, 77, 35–40. https://doi.org/10.1016/j.materresbull.2016.01.020.

31. Alvarez, K.; Fukuda, M.; Yamamoto, O. Titanium Implants after Alkali Heating Treatment with a [Zn(OH)4]2− Complex: Analysis of Interfacial Bond Strength Using Push-Out Tests. Clin. Implant. Dent. Relat. Res. 2009, 12, e114–e125. https://doi.org/10.1111/j.1708-8208.2010.00278.x.

32. Yusa, K.; Yamamoto, O.; Takano, H.; Fukuda, M.; Iino, M. Zinc-modified titanium surface enhances osteoblast differentiation of dental pulp stem cells in vitro. Sci. Rep. 2016, 6, 29462. https://doi.org/10.1038/srep29462.

33. Hu, H.; Zhang, W.; Qiao, Y.; Jiang, X.; Liu, X.; Ding, C. Antibacterial activity and increased bone marrow stem cell functions of Zn-incorporated TiO_2 coatings on titanium. Acta Biomater. 2012, 8, 904–915. https://doi.org/10.1016/j.actbio.2011.09.031.

34. Zhang, Z.; Gu, B.; Zhang, W.; Kan, G.; Sun, J. The enhanced characteristics of osteoblast adhesion to porous Zinc– TiO_2 coating prepared by plasma electrolytic oxidation. Appl. Surf. Sci. 2012, 258, 6504–6511. https://doi.org/10.1016/j.apsusc.2012.03.067.

35. Le Guehennec, L.; Lopez-Heredia, M.-A.; Enkel, B.; Weiss, P.; Amouriq, Y.; Layrolle, P. Osteoblastic cell behaviour on different titanium implant surfaces. Acta Biomater. 2008, 4, 535–543. https://doi.org/10.1016/j.actbio.2007.12.002.

36. Zareidoost, A.; Yousefpour, M.; Ghaseme, B.; Amanzadeh, A. The relationship of surface roughness and cell response of chem-ical surface modification of titanium. J. Mater. Sci. Mater. Med. 2012, 23, 1479–1488. https://doi.org/10.1007/s10856-012-4611-9.

37. Manivasagam, V.K.; Popat, K.C. In vitro investigation of hemocompatibility of hydrothermally treated titanium and titanium alloy surfaces. ACS Omega 2020, 5, 8108–8120. https://doi.org/10.1021/acsomega.0c00281.

38. Popat, K.C.; Leoni, L.; Grimes, C.A.; Desai, T.A. Influence of engineered titania nanotubular surfaces on bone cells. Biomaterials 2007, 28, 3188–3197. https://doi.org/10.1016/j.biomaterials.2007.03.020.

39. Sabino, R.M.; Kauk, K.; Movafaghi, S.; Kota, A.; Popat, K.C. Interaction of blood plasma proteins with superhemophobic tita-nia nanotube surfaces. Nanomed. Nanotechnol. Biol. Med. 2019, 21, 102046. https://doi.org/10.1016/j.nano.2019.102046.

40. Barthes, J.; Ciftci, S.; Ponzio, F.; Knopf-Marques, H.; Pelyhe, L.; Gudima, A.; Kientzl, I.; Bognár, E.; Weszl, M.; Kzhyshkowska, J.; et al. Review: The potential impact of surface crystalline states of titanium for biomedical applications. Crit. Rev. Biotechnol. 2018, 38, 423–437. https://doi.org/10.1080/07388551.2017.1363707.

41. Wang, G.; Li, J.; Lv, K.; Zhang, W.; Ding, X.; Yang, G.; Liu, X.; Jiang, X. Surface thermal oxidation on titanium implants to en-hance osteogenic activity and in vivo osseointegration. Sci. Rep. 2016, 6, 31769. https://doi.org/10.1038/srep31769.

42. Dias-Netipanyj, M.F.; Sopchenski, L.; Gradowski, T.; Elifio-Esposito, S.; Popat, K.C.; Soares, P. Crystallinity of TiO_2 nanotubes and its effects on fibroblast viability, adhesion, and proliferation. J. Mater. Sci. Mater. Med. 2020, 31, 94 . https://doi.org/10.1007/s10856-020-06431-4.

43. Del Curto, B.; Brunella, M.; Giordano, C.; Pedeferri, M.; Valtulina, V.; Visai, L.; Cigada, A. Decreased bacterial adhesion to sur-face-treated titanium. Int. J. Artif. Organs 2005, 28, 718–730. https://doi.org/10.1177/039139880502800711.

44. Ercan, B.; Taylor, E.; Alpaslan, E.; Webster, T.J. Diameter of titanium nanotubes influences anti-bacterial efficacy. Nanotechnol-ogy 2011, 22, 295102. https://doi.org/10.1088/0957-4484/22/29/295102.

45. Puckett, S.D.; Taylor, E.; Raimondo, T.; Webster, T.J. The relationship between the nanostructure of titanium surfaces and bacte-rial attachment. Biomaterials 2010, 31, 706–713. https://doi.org/10.1016/j.biomaterials.2009.09.081.

46. Eriksson, C.; Nygren, H.; Ohlson, K. Implantation of hydrophilic and hydrophobic titanium discs in rat tibia: Cellular reac-tions on the surfaces during the first 3 weeks in bone. Biomaterials 2004, 25, 4759–4766. https://doi.org/10.1016/j.biomaterials.2003.12.006.

47. Yao, X.; Peng, R.; Ding, J. Cell-material interactions revealed via material techniques of surface patterning. Adv. Mater. 2013, 25, 5257–5286. https://doi.org/10.1002/adma.201301762.

48. Discher, D.E.; Janmey, P.; Wang, Y.-L. Tissue cells feel and respond to the stiffness of their substrate. Science 2005, 310, 1139–1143. https://doi.org/10.1126/science.1116995.

49. Sorkin, J.A.; Hughes, S.; Soares, P.; Popat, K.C. Titania nanotube arrays as interfaces for neural prostheses. Mater. Sci. Eng. C 2015, 49, 735–745. https://doi.org/10.1016/j.msec.2015.01.077.

50. Sun, Q.; Hou, Y.; Chu, Z.; Wei, Q. Soft overcomes the hard: Flexible materials adapt to cell adhesion to promote cell mecha-notransduction. Bioact. Mater. 2022, 10, 397–404. https://doi.org/10.1016/j.bioactmat.2021.08.026.

51. Arciola, C.; An, Y.; Campoccia, D.; Donati, M.; Montanaro, L. Etiology of Implant Orthopedic Infections: A Survey on 1027 Clinical Isolates. Int. J. Artif. Organs 2005, 28, 1091–1100. https://doi.org/10.1177/039139880502801106.

52. Campoccia, D.; Montanaro, L.; Arciola, C.R. The significance of infection related to orthopedic devices and issues of antibiotic resistance. Biomaterials 2006, 27, 2331–2339. https://doi.org/10.1016/j.biomaterials.2005.11.044.

53. Ribeiro, M.; Monteiro, F.J.; Ferraz, M.P. Infection of orthopedic implants with emphasis on bacterial adhesion process and techniques used in studying bacterial-material interactions. Biomatter 2012, 2, 176–194. https://doi.org/10.4161/biom.22905.

54. Schierholz, J.; Beuth, J. Implant infections: A haven for opportunistic bacteria. J. Hosp. Infect. 2001, 49, 87–93. https://doi.org/10.1053/jhin.2001.1052.

55. Wilson, W.; Wade, M.M.; Holman, S.C.; Champlin, F.R. Status of methods for assessing bacterial cell surface charge properties based on zeta potential measurements. J. Microbiol. Methods 2001, 43, 153–164. https://doi.org/10.1016/s0167-7012(00)00224-4.

56. Diggle, S.P.; Whiteley, M. Microbe Profile: *Pseudomonas aeruginosa*: Opportunistic pathogen and lab rat. Microbiology 2020, 166, 30–33. https://doi.org/10.1099/mic.0.000860.

57. Harris, L.; Foster, S.; Richards, R. An introduction to *Staphylococcus aureus*, and techniques for identifying and quantifying *S. aureus* adhesins in relation to adhesion to biomaterials: Review. Eur. Cells Mater. 2002, 4, 39–60. https://doi.org/10.22203/ecm.v004a04.

CHAPTER 3/TITANIA (TiO_2) NANOTUBE SURFACES DOPED WITH ZINC AND STRONTIUM FOR IMPROVED CELL COMPATIBILITY

3.1 Introduction

Titanium-based orthopedic implants are gaining popularity in recent years due to their excellent biocompatibility, superior corrosion resistance and lightweight properties. However, these implants often fail to perform effectively due to poor osseointegration. Nanosurface modification approaches may help to resolve this problem. In this work, TiO_2 nanotube (NT) arrays were fabricated on commercially available pure titanium (Ti) surface by anodization and annealing. Then, zinc (Zn) and strontium (Sr), important for cell signaling, were doped on the NT surface by hydrothermal treatment. This very simple method of Zn and Sr doping takes less time and energy compared to other complicated techniques. Different surface characterization tools such as scanning electron microscopy (SEM), X-ray photoelectron spectroscopy (XPS), energy-dispersive X-ray spectroscopy (EDS), static water contact angle, X-ray diffraction (XRD) and nanoindentation techniques were used to evaluate the modified surfaces. Then, adipose derived stem cells (ADSCs) were cultured with the surfaces to evaluate cell adhesion, proliferation, and growth on the surfaces. After that, the cells were differentiated towards osteogenic lineage to evaluate alkaline phosphatase (ALP) activity, osteocalcin expression, and calcium phosphate mineralization. Results indicate that NT surfaces doped with Zn and Sr had significantly enhanced ADSC adhesion, proliferation, growth, and osteogenic differentiation compared to unmodified surface, thus confirming the enhanced performance of these surfaces.

Orthopedic implants play a key role to provide necessary support to the dynamic bone tissue while it undergoes remodeling and healing at the damaged site [1]. For a successful bone healing, interaction between the implant surface and bone tissue is profoundly important and

determines the success of the bone healing process. A proper interaction between the implant and bone tissue by the formation of new bone matrix around the implant is known as osseointegration [2]. An adequate osseointegration is determined by the osteoblast differentiation of mesenchymal stem cells (MSC) which is known as osteoinductivity, along with the new bone matrix deposition on the material surface known as osteoconductivity [3-4] Therefore, the osteoblast differentiation on the implant surface can be a good indicator to understand the efficacy of the implant for better osseointegration. For that reason, it is imperative to design implant surfaces that promote good osseointegration resulting in successful bone healing.

Orthopedic implants can be made of different materials such as metallic, polymeric, ceramic or composites. For example, a polymeric implant can be used for healing a damaged soft cartilage tissue. However, when the goal is to provide robust support to the damaged bone, a metallic implant is a better choice over polymer due to high cyclic load bearing capacity of metals over polymers. Certain reasons dictate the dominance of metals as orthopedic implants, one of which is the chemical inertness offered by the presence of an oxide layer on passive metal surfaces [5]. Since 1921, three most popular choices of metallic orthopedic implants were stainless steel (SS), chromium-cobalt (CC) alloys, and titanium (Ti) based implants [5]. Among these choices, Ti offers superior advantage over the others owing to its corrosion prevention, inertness, superior strength, and lightweight properties [6]. Additionally, Ti possesses excellent biocompatibility that helps in reducing immune response and bacterial infection after the orthopedic implant surgery. However, around 10% of Ti based implants fail each year mainly due to poor osseointegration which causes aseptic loosening of the implant from the desired bone site [4].

To improve the osseointegration properties of the Ti implants, nanosurface modification approaches have been utilized in recent years. Introduction of nanoscale features on pure Ti surface

were found to increase extracellular matrix protein absorption and cell attachment, while stimulating the osteogenic differentiation [7]. Several nano and micro surface modifications on Ti surfaces have been utilized in recent years [8]. Among them, nanotube structures are interesting because they impart additional material properties such as wettability, mechanical flexibility, hemocompatibility, and biocompatibility which are advantageous over pure Ti [9-10]. The nanotubes are formed by continuous anodization and etching of the TiO_2 layer. One of the important advantages of the nanotube structure is that they can act as anchoring points for the MSCs to adhere efficiently to the surface. Another advantage is that the nanotube structures are flexible in nature and help in accommodating the mechanical stress coming from the cells which results in better cell attachment and spread. However, they do not provide any relevant important signaling elements to the cells to differentiate into a specific phenotype. Therefore, a new approach should be investigated for nanosurface modification of Ti to improve the osseointegration properties.

Zinc (Zn) and strontium (Sr) act as important signaling elements for the MSCs to differentiate into osteoblasts. Zn is found as a micronutrient in bone and help in bone formation [11]. Additionally, previous studies reported that Zn provides antibacterial activity to the surfaces [12-13]. On the other hand, Sr is another important trace element for maintaining bone health. Sr helps in reducing osteoclast formation and improves osteoblasts differentiation which helps in bone healing instead of bone resorption [14]. For these reasons, incorporation of these important trace elements on the implant surface may help in achieving better cell compatibility and osseointegration. Different doping techniques such as hydrothermal, alkaline heat-treatment, photo electrolytic oxidation (PEO), micro-spark oxidation, magnetron sputtering, and plasma spray have been reported in the literature [15]. Among these methods, hydrothermal process is relatively

simple since it uses only few chemicals and a lower reaction time. In a previous study, Zn was doped on Ti surfaces using hydrothermal and alkaline-heat treatment, and it was found that hydrothermally treated surfaces provided better antibacterial activity than the alkaline-heat treated surfaces [16]. In this study, Zn and Sr, were doped on the titanium surfaces via hydrothermal treatment. The surfaces were characterized by using scanning electron microscopy (SEM), X-ray photoelectron spectroscopy (XPS), and energy dispersive spectroscopy (EDS) to understand surface morphology along with concentration and distribution of Zn and Sr on the surfaces. Static water contact angle was measured using a goniometer to understand the surface wettability. X-ray diffraction (XRD), nanoindentation hardness (H) and elastic modulus (E) were also measured to understand surface crystallinity and mechanical properties of the surfaces. Then cell compatibility of these surfaces was evaluated using adipose derived stem cells (ADSCs). Since ADSCs are MSCs derived from the abundant adipose tissue by minimally invasive procedure, their use is gaining popularity for biomaterials research [17]. ADSC adhesion, proliferation, and differentiation to osteoblastic phenotype was analyzed on different surfaces. After that, Adhered ADSCs were differentiated towards osteoblastic lineage. After 1 and 3 weeks of ADSC culture, alkaline phosphatase (ALP) activity, osteocalcin expression, and cell mineralization were analyzed to evaluate ADSC differentiation towards osteoblasts on the modified surfaces. The results indicate that surfaces with Zn and Sr could significantly improve ADSC adhesion and proliferation compared to pure titanium. TiO_2 nanotube (NT) surface doped with Sr exhibited the most promising result by enhanced ADSC differentiation towards osteoblasts compare to other surfaces indicating its potential of being used as an effective orthopedic implant surface.

3.2 Experimental methods

3.2.1 Titania nanotube surface fabrication

To fabricate titania (TiO_2) nanotube arrays on commercially available pure titanium (Ti) surface, a method described in a previous work was followed [6]. Briefly, titanium surfaces of 2 cm X 2 cm were cut and polished using silicon carbide sheets. Then they were soaked for 3 min in acetone followed by 10 min of sonication using a bath sonicator. Then the surfaces were cleaned using soap and isopropyl alcohol followed by 10 min of sonication in isopropyl alcohol and deionized (DI) water respectively. Then the surfaces were dried inside the fume hood prior to anodization. For anodization, an electrolyte solution containing 95% diethylene glycol (DEG, Thermo Fisher Scientific Chemicals Inc., Ward Hill, MA, USA), 2% hydrofluoric acid (HF, 48%, KMG Electronic Chemicals, Inc., Houston, TX, USA), and 3% DI water was prepared. Then cleaned Ti surfaces were connected to the electrolytic cell as anode using alligator tips. Similar sized platinum (Pt) surfaces were connected to the electrolytic cell as cathode. Then 55 kV electricity was applied to the electrolytic cells for 22 h at room temperature to perform anodizing and electrochemical etching on the Ti surfaces resulting in fabrication of nanotube arrays. After anodization, the surfaces were thoroughly cleaned with DI water and isopropyl alcohol and dried inside a hood for further processing. A control group of surfaces were annealed right after anodization at 530°C for 3 h with 15°C/min temperature increments. These surfaces were designated as NT. Cleaned Ti surfaces were also used as controls.

3.2.2 Zinc and strontium doping on different surfaces

Zinc (Zn) and strontium (Sr) were doped on anodized titanium surfaces by hydrothermal treatment. For Zn doping, the surfaces were incubated with a solution of 0.1 M zinc acetate inside

a polytetrafluoroethylene (PTFE) lined hydrothermal autoclave reactor for 1 h at 200°C. To dope Sr, the surfaces were incubated with a solution of 0.02 M strontium acetate octahydrate inside a polytetrafluoroethylene (PTFE) lined hydrothermal autoclave reactor for 1 h at 200°C. After the treatment, the surfaces were cleaned thoroughly with running DI water to remove excess solution. Finally, the surfaces were annealed at 530°C for 3 h inside a furnace to prepare NTZn and NTSr surfaces.

3.2.3 Surface characterization

Different surface properties such as surface morphology, Zn and Sr distribution on the surface, surface chemistry, stability, wettability, and mechanical properties were evaluated in this work. These different surface characterization methodologies are described below.

- To characterize the morphology of Ti, NT, NTZn, and NTSr surfaces, scanning electron microscopic (SEM) images were collected using a JEOL JSM-6500F field emission scanning electron microscope (FESEM). The operating voltage was 15 kV with a probe current of 7 A. SEM images were collected in varying magnifications from 500x to 30,000x. To ensure high-equality SEM images, working distance, contrast and brightness were adjusted during the image collection process.
- To examine the surface chemistry, X-ray photoelectron spectroscopy (XPS) survey spectra were collected for each surface. A PHI Physical Electronics PE-5800 X-ray Photoelectron Spectrometer with an Al Kα X-ray source was used to collect the survey spectra from 0 V to 1100 V. MultiPak (version 9.6.1.7) software was used to analyze the XPS spectra. From the survey spectra, corresponding atomic weight percentage (% at) of each element on the surfaces were analyzed using the MultiPak software.

- To confirm a uniform distribution of Zn and Sr on the surfaces, energy-dispersive X-ray spectroscopy (EDS) was used. An Oxford SDD EDS detector connected to the FESEM was utilized to collect the EDS spectra and corresponding element maps for each surface. Oxford Aztec software was used to analyze the EDS spectra and maps.
- To evaluate wettability of the surfaces, static water contact angle was measured using a Ramé-Hart goniometer (Ramé-Hart Instrument Co., Succasunna, NJ, USA). A DI water droplet of approximately 10 µl was dropped on each surface using a micrometer syringe. An image of the droplet was collected using the camera system of the goniometer. Finally, contact angle values were measured from the images using the DROPimage software.
- To examine surface crystallinity, X-ray diffraction (XRD) spectra were collected using XRD-7000 Shimadzu. CuKα radiation at 40 kV and 30 mA was utilized while collecting the spectra. A thin film geometry with an incidence angle of 5° was used. Continuous scans from 20° to 80° at a scanning speed of 1°/min was used to collect the diffractograms. Match! software with PDF2 database was used for indexing the peaks.
- Surface mechanical properties such nanoindentation hardness (H) and elastic modulus (E) were evaluated by using a nanoindentation procedure. A Nanoindenter (ZwicK-Roell/Asmec) was programmed by an array (5 × 5), with 50 µm distance between each indentation and 0.1 N of maximum applied force on the surface by a calibrated Berkovich tip. The indentation method used was the quasi-continuous stiffness measurement (QCSM) method. This method allows for high accuracy measurements due to a progressively increasing force (from 0–100 mN for this study) combined with a dwell time at each force point.

- To evaluate the Zn and Sr stability on the surfaces, XPS spectra of each surface was collected at 0 and 28 days of incubation with DI water. 1 cm x 1 cm surfaces were cut and XPS spectra were taken at 0 day. From the spectra, atomic weight % (at%) of the respective Zn and Sr were calculated. Then, the surfaces were incubated with 500 ml of DI water for 28 days. XPS spectra were collected again and at% were calculated to evaluate the change in Zn and Sr concentration on the surfaces.

3.2.4 Adipose derived stem cell (ADSC) culture

Adipose derived stem cells (ADSCs) of passage 3 were generously donated by Dr. Kimberly Cox-York from the Department of Food Science and Human Nutrition at the Colorado State University. The ADSCs were cultured in a growth medium containing 90% MEM Alpha Modification (1×, cytiva, Marlborough, MA, USA), 9% fetal bovine serum (FBS), and 1% penicillin-streptomycin in an incubator at 37°C and 5% CO_2. Prior to the cell compatibility studies, surfaces of 1 cm X 1 cm dimensions were cut and sterilized with 70% ethanol and then thoroughly cleaned with DI water and PBS followed by further sterilization with UV light for 30 min inside a biological safety hood. Then the surfaces were taken into 48-well plates and 20,000 ADSCs/well were introduced. Then the well plates were incubated at 37°C and 5% CO_2 for subsequent experiments. The growth media was changed after 4 days of incubation for all the well plates.

3.2.5 Cytotoxicity evaluation

To evaluate the cytotoxicity of the surfaces, a lactate dehydrogenase (LDH) based indicator assay (CyQuant™ LDH Cytotoxicity Assay Kit, ThermoFisher Scientific, Waltham, MA, USA) was used. ADSCs (passage 6) were cultured separately followed by the method described above.

Then, the surfaces were sterilized and incubated with 20,000 ADSCs/well for 24 hr. After the incubation, 90 µl supernatant from each well were collected in a sterile 90 well plate. Then, manufacturer's protocol was followed to determine the cytotoxicity of the surfaces.

3.2.6 Cell adhesion, proliferation, and morphology on the surfaces

- To evaluate cell adhesion and proliferation on the surfaces, the surfaces were taken out from the incubator after 4 and 7 days. The surfaces were then rinsed with PBS for 3 times to remove any unadhered cells. Then adhered cells were fixed on the surfaces using 3.7% formaldehyde in PBS for 15 min followed by 3 rinses with PBS. The fixed cells were then permealized using 1% triton-X in PBS followed by two rinses with PBS. Then the surfaces were incubated for 25 min in 70 nM rhodamine phalloidin (Cytoskeleton, Inc., Denver, CO, USA) which stained the actin filaments of the cells. Then 300 nm nuclear stain DAPI (ThermoFisher Scientific, Waltham, MA, USA) was added. Then the surfaces were incubated for 5 min followed by 2 rinses with PBS. Finally, a fluorescence microscope (Zeiss) was used to collect images of the surfaces. The images were analyzed to quantify cell adhesion and proliferation by counting the number of stained nuclei (DAPI) using imageJ software.
- SEM images were collected to examine the adhered cell morphology on the surfaces. Prior to image collection, the surfaces were taken out from the incubator after 4 and 7 days of incubation. Then the surfaces were rinsed 3 times with PBS to remove any unadhered cells. Then the surfaces were incubated with a primary fixative solution containing 3% glutaraldehyde (Sigma-Aldrich, St. Louis, MO, USA), 0.1 M sucrose (Sigma-Aldrich, St. Louis, MO, USA), and 0.1 M sodium cacodylate (Electron Microscopy Sciences, Hatfield,

PA, USA) in DI water for 45 min at room temperature. After that, the surfaces were incubated with a buffer solution containing the primary fixative without the glutaraldehyde for 10 min. Then the adhered cells were dehydrated using 35%, 50%, 75%, and 100% sequentially for 10 min in each solution. Then the surfaces were gold coated (10 nm thickness) using a sputter coater to enhance the conductivity of the adhered cells. Finally, the FESEM was used to take images of the surfaces at 15 kV with 7 A probe current. Images of different magnifications ranging from 100x to 2000x were collected. Brightness, contrast, and working distance settings were adjusted for ensuring high-quality of the SEM images.

3.2.7 Osteogenic differentiation of ADSCs

After 7 days of ADSC culture with the growth media, osteogenesis was introduced using an osteogenic differentiation media. This media was prepared by taking the growth media and supplementing it with 10^{-8} M dexamethasone (Sigma, 98 %), 50 μg/mL ascorbic acid (Sigma, 100 %), and 6 mM β-glycerol phosphate (Sigma, 98 %). The differentiation media was changed every other day for all the surfaces for 3 weeks. After 1 and 3 weeks of incubation period, the surfaces were analyzed to evaluate cell differentiation properties.

- Alkaline phosphate (ALP) activity of the cells at 1 and 3 weeks normalized by total protein content was evaluated to determine the differentiation activity of ADSCs when incubated with the surfaces. QuantiChrom™ Alkaline Phosphatase Assay Kit (DALP-250) (BioAssay Systems, Hayward, CA) was used for colorimetric determination of serum alkaline phosphatase activity. To measure the total protein content, a Micro BCA Protein

Assay Kit (ThermoFisher Scientific, Waltham, MA, USA) was used. Manufacturer's protocols were followed to collect and analyze data for both assays.

- Immunofluorescence (IF) images were collected for all the surfaces to evaluate osteocalcin expression from the differentiated osteoblasts. For this, the surfaces were collected after 1 and 3 weeks, and washed with PBS for 3 times. Then the cells were fixed using 3.7% formaldehyde in PBS for 15 min followed by 3 rinses with PBS. The fixed cells were then permealized using 1% triton-X in PBS followed by two rinses with PBS. After that, the cells were incubated with a blocking serum in PBS for 30 min followed by a rinse with PBS. Then, the surfaces were incubated with a primary osteocalcin antibody solution (1:100 in 1% BSA) for 1 h followed by three rinses with PBS. After that, the surfaces were incubated with a secondary FITC-conjugated antibody (1:200 in 1% BSA) for 45 min followed by two PBS rinses. After that, actin filament stain rhodamine phalloidin and nuclear stain DAPI were added followed by the procedure described above. Finally, IF images of the surfaces were collected using a fluorescence microscope (Zeiss). Osteocalcin coverage area and the number of adhered cells were analyzed from the images using imageJ software.
- SEM images were also collected to determine hydroxyapatite (HA) mineral deposition by differentiated osteoblasts. After 1 and 3 weeks of incubation, the surfaces were washed with PBS 3 times and the adhered cells were fixed to the surfaces following the SEM protocol described above. EDS elemental maps were also collected to confirm the elemental composition of the deposited minerals.

3.2.8 Statistical analysis

For morphological surface characterization via SEM, at least 5 images were taken for each sample group ($n_{min}=5$). For XPS, EDS, surface wettability analysis, 3 samples were used for each sample group ($n_{min}=3$). During cell study, 3 samples were used for taking 9 fluorescence microscope images ($n_{min}=9$). For cell viability, cytotoxicity, and protein studies (ALP, BCA) at least 4 samples were used for each sample group ($n_{min}=4$). To evaluate statistically significant difference between sample groups, analysis of variance (ANOVA) was conducted followed by post-hoc T-test ($\alpha = 0.05$).

3.3 Results and discussions

Surface characteristics of materials dictates the way a biological agent such as bacteria or cell interacts with the material. Previous studies suggest that nanoscale surface features can help in reducing bacterial infection along with increment in stem cell adhesion, proliferation, and differentiation [8,18-20]. Therefore, several material characterization techniques were utilized in the current study to understand the surface features of the modified Ti surfaces. First, morphological features of the surfaces were evaluated with scanning electron microscopic (SEM) images (**Figure 3.1**). Ti had relatively smooth morphology with no unique distinguishable features. When TiO_2 nanotubes (NT) were formed on the Ti surfaces via anodization and annealing, significant morphological change was observed. When Ti surfaces is used as anode in an electrolyte solution containing hydrofluoric acid (HF) alongside platinum as cathode, two separate processes happen simultaneously. H_2O from the electrolyte solution starts the anodization process and creates a TiO_2 layer. Simultaneously, pits form on this TiO_2 layer due to the electric field dissolution of oxide layer. In those pits, the F^- from HF starts etching the oxide layer to form tubular

nanotube structures [21]. As shown in SEM images in **Figure 3.1**, the tube-like structures were evenly distributed on the surfaces. The nanotubes were around 80-100 nm long with a 30-50 nm diameter. During the hydrothermal doping process, Zn ions from the zinc acetate solution forms ZnO which get embedded into the TiO_2 nanotubes. The NTZn surfaces had crystal-like structures (pointed by arrows in **Figure 3.1**) on top of nanotubes which were Zn crystals deposits from the hydrothermal treatment (confirmed by EDS, described later). The Zn crystals were found to be randomly distributed throughout the surface with certain areas having higher concentration of crystals [17]. Further, SEM images revealed that NTSr surfaces had larger rod-shaped crystals (pointed by arrows in **Figure 3.1**). These crystals were significantly larger in size compared to the Zn crystals on the NTZn surface. During the Sr doping by hydrothermal treatment, Sr ions from the strontium acetate octahydrate form $SrTiO_3$ (confirmed by XRD spectra analysis, described later) with TiO_2 that results into large crystals. A small amount of SrF_2 is also formed during this stage by the reaction between residual F^- ions from anodization and Sr ions (confirmed by XPS, described later). The formed crystals were mostly evenly distributed throughout the surface. Like the NTZn surface, certain areas on NTSr surfaces had higher concentration of these crystals.

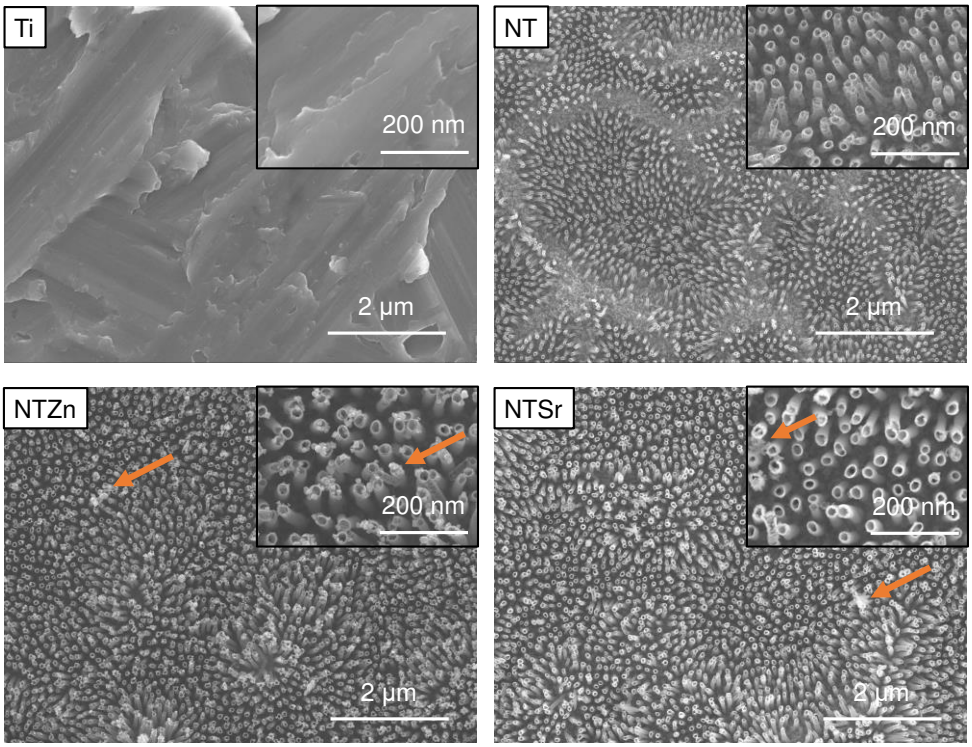

Figure 3.1. SEM images of different surfaces.

Uniform distribution of Zn and Sr on the surfaces is important to ensure a consistent surface for better osseointegration. Energy dispersive X-ray spectroscopy (EDS) maps were collected to understand the Zn and Sr distribution on different surfaces. The EDS maps can also confirm whether the crystals observed in SEM were Zn and Sr or not. EDS maps presented in **Figure 3.2** showed the Zn and Sr distributions. The results confirmed that observed crystals in SEM images were indeed Zn and Sr (confirmed by the purple-colored Zn and yellow-colored Sr maps). The images also indicated that the ions were evenly distributed throughout the surfaces with some area of higher concentrations. These results support the findings from SEM images.

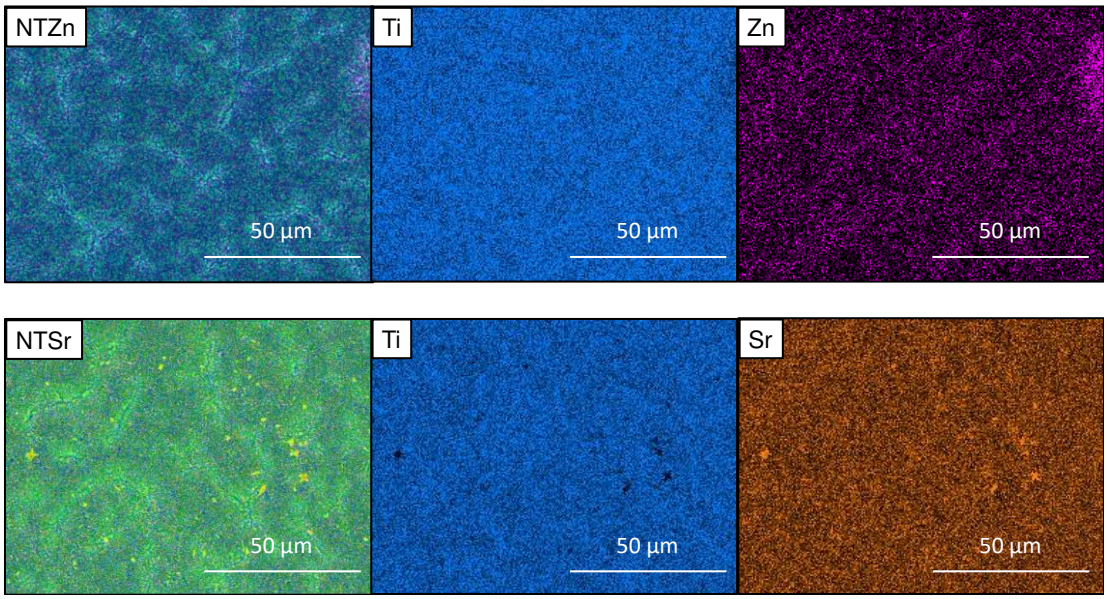

Figure 3.2. EDS maps of Ti, Zn and Sr on NTZn and NTSr surfaces.

Surface chemistry analysis is an important aspect to understand the successful chemical modification on different surfaces. To understand the surface chemistry, XPS spectra were collected for all the surfaces (**Figure 3.3**). Metal oxides such as TiO_2 is formed on metals as a natural process when the metal surface is in contact with atmospheric oxygen. The anodization process helps to enhance this oxide formation while the presence of fluoride (F^-) ion in the electrolyte etches the oxide layer to form nanotubes. So, the surface chemistry of the NT should not be drastically different than Ti, which was confirmed from the XPS spectra (**Figure 3.3**). However, after Zn and Sr doping, new peaks were formed on the surfaces. Zn2p peaks were identified at 1016 eV and 1021 eV binding energy, which confirmed the presence of Zn ions on the NTZn surface. On the other hand, Sr3s and Sr3p peaks were identified at 357 eV and 268 eV on the NTSr surface, confirming the presence of Sr on this surface. NTSr also had an additional peak at 133 eV. This peak indicates the presence of SrF_2 which formed during the hydrothermal process. It is possible that some residual F^- ions might have remained on the surface after

anodization and interreacted with the Sr ions during the hydrothermal process to form SrF_2. Since the amount of F^- was significantly less in the final NTSr surface, it should not possess any cytotoxicity towards human cells (confirmed by cytotoxicity test, described later).

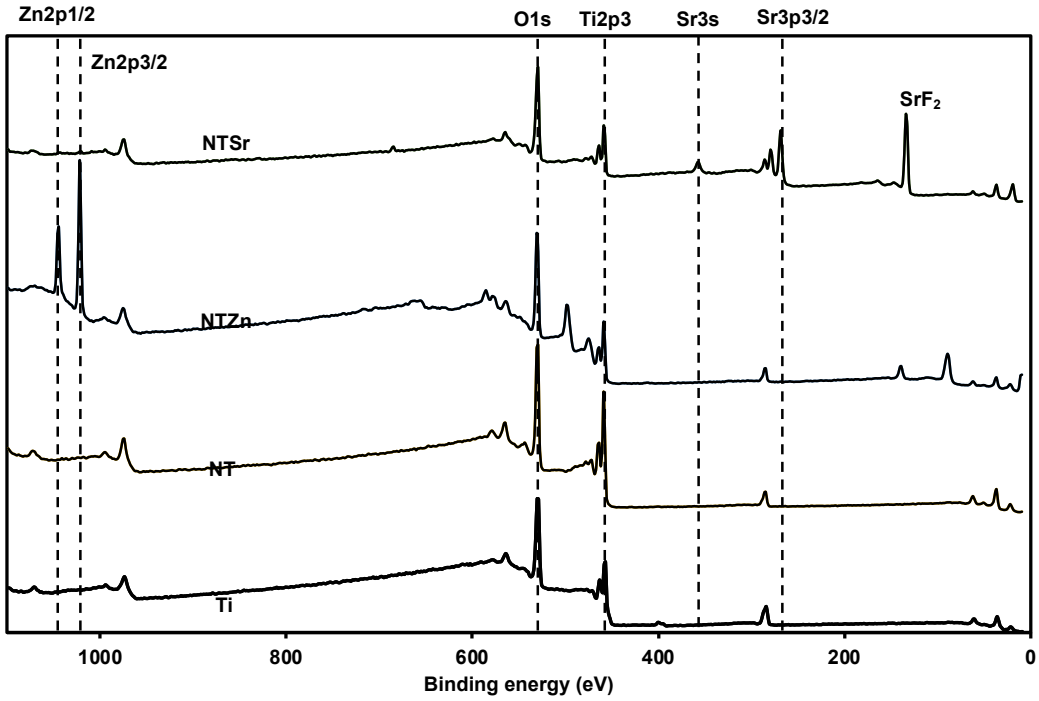

Figure 3.3. XPS spectra of different surfaces.

Relative atomic weight percentage (at%) of different elements on the surfaces was calculated from the XPS survey spectra (**Table 3.1**). The at% for Zn was 22% on NTZn, while Sr was 16% on NTSr. The Sr at % of was a bit lower compared to Zn probably due to the lower concentration of strontium acetate octahydrate during the hydrothermal process. These at% can be optimized by changing the concentrations of the acetates, temperature, and time used during the hydrothermal process. However, a thorough cytotoxicity analysis should follow because a higher Zn or Sr concentration can be toxic to the human cells. The presence of F on the NTSr surface was confirmed to be very low (0.8%).

Table 3.1. Elemental composition of different surfaces from XPS survey spectra. The compositions are expressed as relative atomic weight percentage (at%).

Surface	% Zn	% Sr	% F
Ti	0	0	0
NT	0	0	0
NT_{hyt}	22	0	0
NT_{Sr}	0	16.1	0.8

Surface wettability is an important material property that can influence cell adhesion, proliferation, and differentiation to osteoblasts. Previous studies have suggested that a superhydrophilic surface can improve cell adhesion [22-23]. Other studies also suggest that superhydrophilic surfaces can reduce bacteria adhesion and proliferation, thus reducing the risk of bacterial infection owing to the surgical procedures of implant insertion in the host [24]. When the contact angle is less than 10°, then the surface is superhydrophilic. The static water contact angle of NT and NTSr was measured as 0°, confirming these surfaces were superhydrophilic (**Figure 3.4**). The NTZn surface was hydrophilic since the contact angle was a little bit higher (17°) than NT and NTSr surfaces. Due to the presence of tubular structures on the NT surfaces, water molecules get trapped between the empty spaces of the tubes, creating a thin water layer on the surface that makes the surfaces superhydrophilic. However, when Zn crystals were deposited on the NT, they likely disrupted the thin hydrophilic layer and reduced the hydrophilic properties.

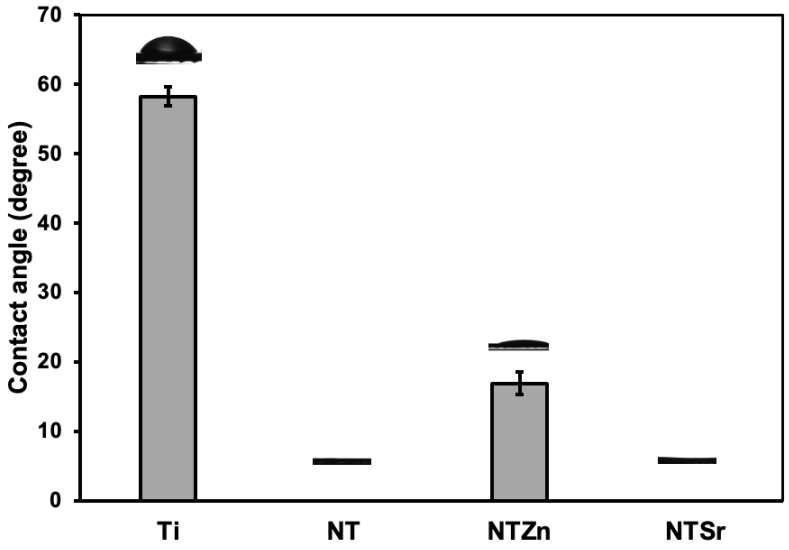

Figure 3.4. Static water contact angle measurements of the surfaces.

Surface crystallinity affects the stem cell adhesion, growth, and differentiation [25]. Thus, determining crystalline phases of the modified Ti surfaces is important to understand the probability of the cell compatibility of these surfaces. As a metal, Ti creates a thin oxide layer of TiO_2 on its surface, which mostly constitutes of anatase phase (**Figure 3.5**). During the anodization process, this thin TiO_2 layer was etched by the F^- ion and NT shapes were achieved. However, the NTs were amorphous in this stage. So, to stabilize the structure for further applications, annealing was conducted at 530°C which converted the amorphous regions to crystalline phases. In previous reports it was identified that when both anatase and rutile phases are present in the TiO_2 layer, cell spreading, and differentiation can improve [25]. Similarly, in this study, both anatase and rutile phases were observed on the NT surfaces at 2θ values of 25°, 48° and 27°, 55° respectively. The result aligned with the previously reported peaks for TiO_2 [26]. NTSr had prominent $SrTiO_3$ peaks at 32.55° and 46.68° that confirmed the presence of Sr on the surface. On the other hand, NTZn had a very small ZnO peak at 31.72°.

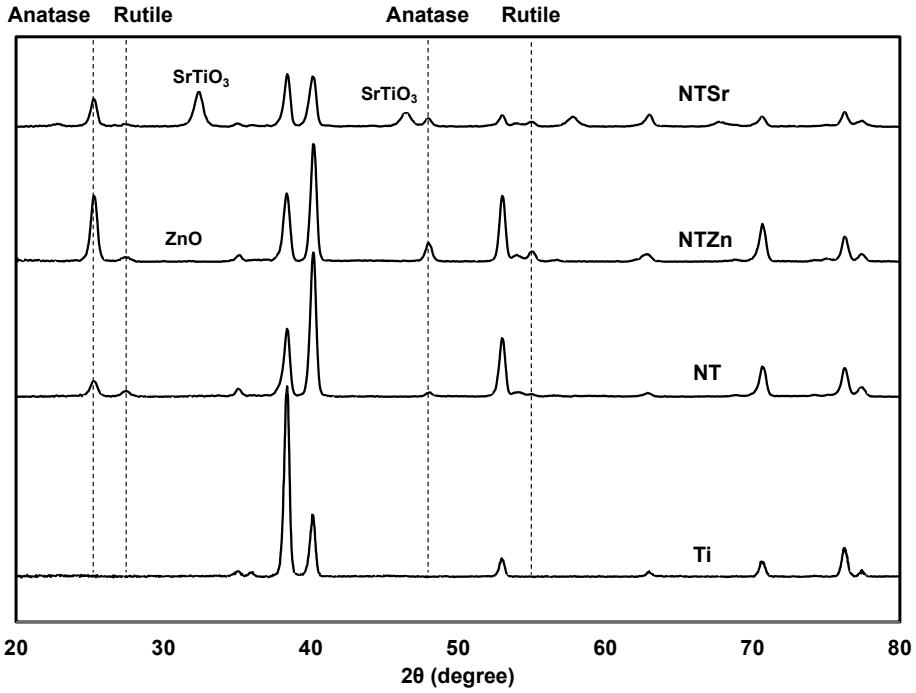

Figure 3.5. XRD spectra of different surfaces.

Mechanical properties of a material surface deeply influence the bioactivity towards the stem cells. Besides, mechanical property analysis can also provide valuable information about the characteristics of the surface important for orthopedic implant applications where constant dynamic load is a factor. Since the surfaces used in this study have nanoscale characteristics, a traditional Instron Tester was deemed unable to identify key mechanical properties owing to the nanofeatures on these surfaces. For that reason, nanoindentation technique was applied to calculate surface hardness (H) and elastic modulus (E). All the NT surfaces (NT, NTZn, and NTSr) had lower H and E compared to the Ti surface as shown in **Table 3.2**. Since the nanotubes are flexible in nature, they probably deflected the nanoindenter and accommodated the applied force, resulting in a softer surface. These flexible and softer surfaces are imperative for the spreading, growth, and differentiation of stem cells to osteoblasts. Previous reports indicated that a softer surface could accommodate mechanical responses coming from the adhered cells which influences the specific

phenotypic differentiation [27]. The elastic modulus and nanoindentation hardness of human trabecular bone is reported as 13.4 GPa and 0.47 GPa [28]. The NT surfaces, especially the NTSr surface has the closest values, thus resembling the mechanical properties of human trabecular bone. Moreover, since the NTs are flexible in nature, they can accommodate the mechanoresponse of ADSCs and help to improve the differentiation these cells to osteoblasts.

Table 3.2. Nanoindentation hardness (H) and elastic modulus (E) values of different surfaces.

Surface	**Nanoindentation Hardness (GPa)**	**Elastic Modulus (GPa)**
Ti	2.52±0.35	138.41±15.96
NT	0.51±0.06	53.17±3.93
NTZn	0.29±0.02	45.19±3.18
NTSr	0.25±0.05	37.64±4.58

Stability of doped Zn and Sr is a crucial for long term effectiveness of implant surfaces. Further, inability of the surfaces to release these important signaling elements to the surrounding environment will reduce the efficacy of the implants. For that reason, stability of the modified surfaces was evaluated by analyzing XPS survey spectra after 0 and 28 days of incubation with DI Water. At day 0, atomic weight % of Zn on NTZn surface was around 23% (**Figure 3.6**). However, it reduced to approximately 5% after 28 days. This indicates that significant amount of Zn was released in the surrounding DI water. A similar trend was observed for the Sr on NTSr surface. At day 0, the atomic weight % of Sr was around 22%, however it was reduced to 10 % after 28 days.

These results strongly indicate that the NTZn and NTSr surfaces release Zn and Sr respectively in the surrounding environment that may enhance signaling effects for cell differentiation.

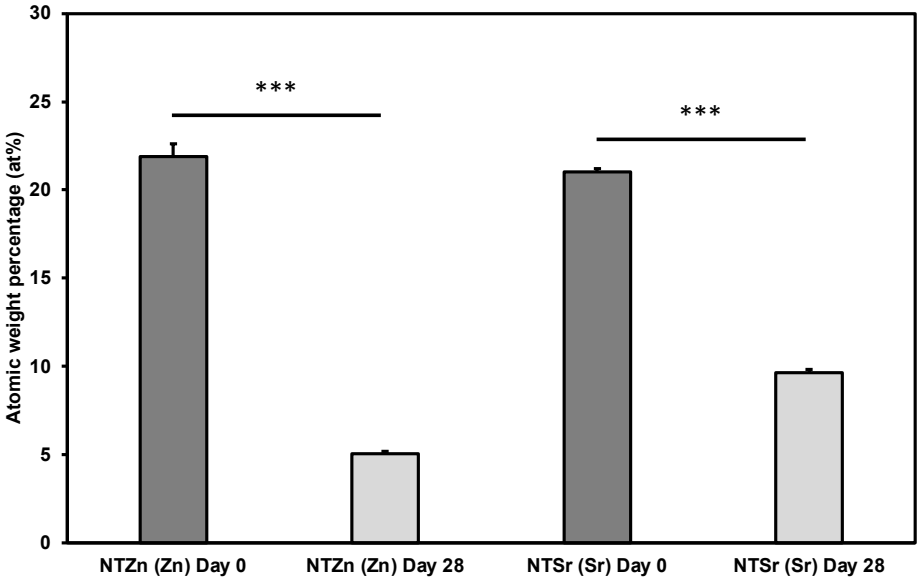

Figure 3.6. Atomic weight percentages (at%) of Zn and Sr on the surfaces after 0 and 28 days of incubation with DI water. Statistical significances (p-value) were represented as *** $p < 0.001$.

Since Zn and Sr surfaces are released from the modified surfaces, it is important to evaluate the cytotoxicity of these surfaces. This is because Zn and Sr overdose can cause toxicity towards surrounding cell and tissue [29-30]. To evaluate cytotoxicity, lactate dehydrogenase (LDH) based indicator assay was used since damaged mammalian cells release LDH enzyme into the surrounding cell media [31]. Two controls were used to evaluate the cytotoxicity of the surfaces: spontaneous LDH release (SR) and maximum LDH release (MR). SR absorbance values were calculated by culturing the ADSCs without any surface, whereas MR values were calculated by damaging all the cultured cells using a 10x lysis buffer. Therefore, MR provided the maximum amount of LDH released from the ADSCs in a culture which indicate the maximum cytotoxicity. On the other hand, SR values indicated no cytotoxicity because no ADSCs were damaged. All the modified surfaces in this study had absorbance values comparable to SR and significantly lower

than MR (**Figure 3.7**), confirming that the surfaces do not exhibit any apparent cytotoxicity towards ADSCs.

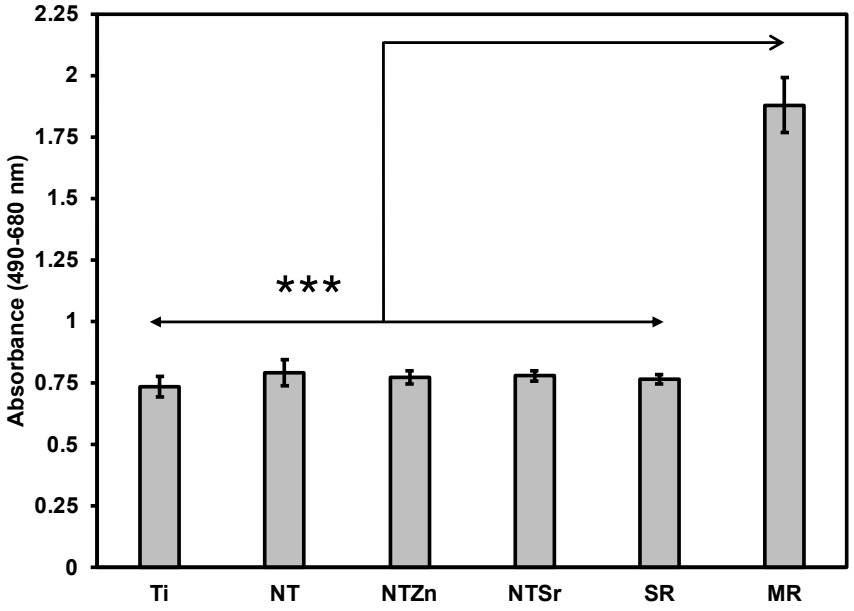

Figure 3.7. Cytotoxicity evaluation of different surfaces. SR=spontaneous LDH release, MR=maximum LDH release. Statistical significances (*p*-value) were represented as *** $p < 0.001$.

Orthopedic implants are extrinsic materials to the host. So, an immediate immune response occurs when an orthopedic implant is placed inside the host. However, if the surface of the implant resembles the host body chemistry, then the immune response slows down and the implant gets acclimated to the host environment which helps in bone healing. For a successful bone healing process, cell adhesion, spread, and proliferation to the implant surface is necessary. Enhanced cell adhesion and proliferation on the implant surface can result in better osteogenic differentiation in later stage which influence better bone regeneration and healing process. ADSCs were cultured with the surfaces for 4 and 7 days to evaluate cell adhesion and proliferation. The fluorescence microscopy images (**Figure 3.8**) showed that all the surfaces had successful cell adhesion after the culture period. However, a closer look reveals that the NTSr surfaces had more cell adhesion

compared to the other surfaces. Also, adhered cells on the NT surfaces (NT, NTZn, and NTSr) covered more area compared to the Ti, indicating better cell proliferation.

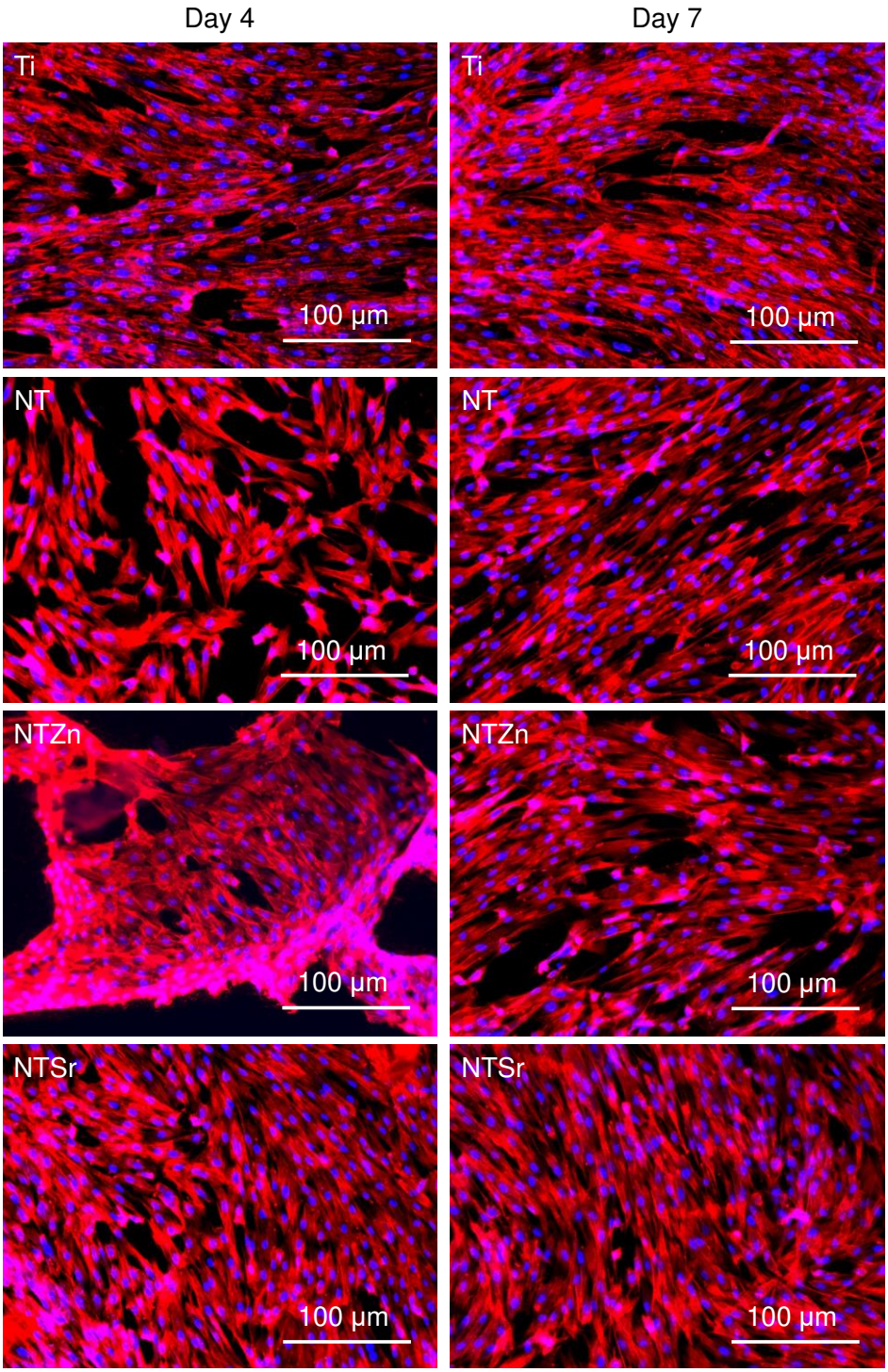

Figure 3.8. Fluorescence microscope images of the surfaces after 4 and 7 days of incubation with ADSCs.

The number of adhered cells were counted from the fluorescence microscopy images. It was observed that at day 4, all the modified surfaces (NT, NTZn, and NTSr) had higher cell adhesion compared to the Ti surface (**Figure 3.9**). The result aligned with the fluorescence images and indicated that the Zn and Sr doping on surfaces could successfully facilitate higher cell adhesion. At day 7, the Ti surface however caught up to the modified surfaces. The reason behind this can be explained from the surface area and cell proliferation capability. Since NTs provide better anchoring points for the cells to adhere to the surface, they spread better on the surfaces overtime which may also help in better osteogenic differentiation. After 7 days of incubation, adhered cells captured almost all the surface area and due to more spreading of cells on the NT surfaces, the number of cells seemed lower in calculation.

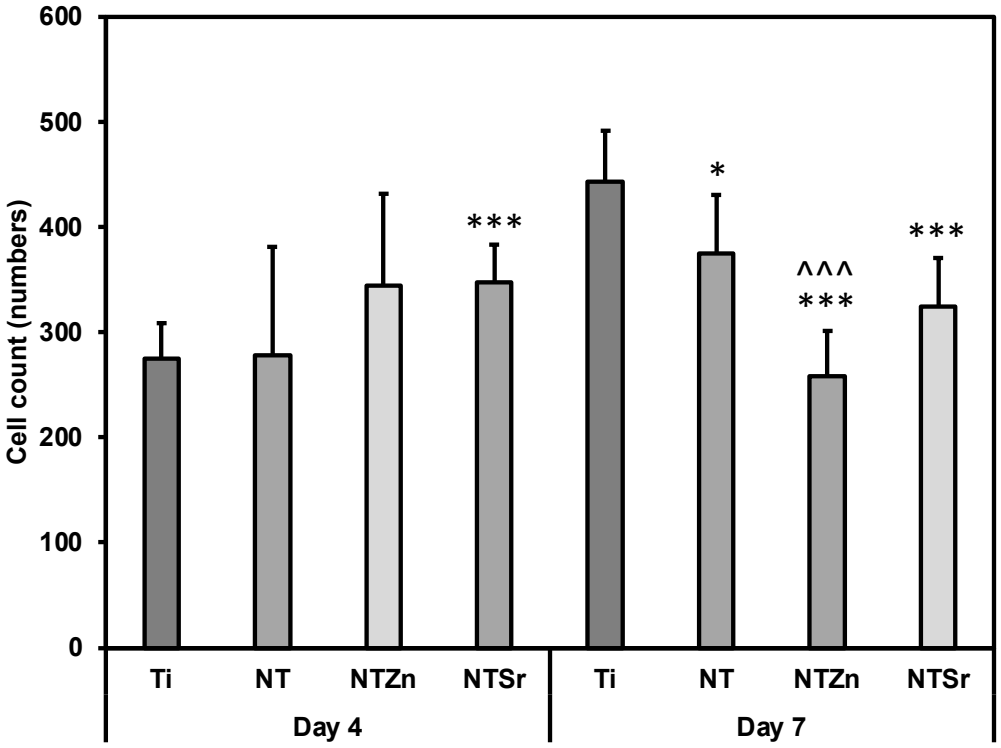

Figure 3.9. ADSC count on each surface after 4 and 7 days of incubation calculated from the fluorescence images. Statistical significances (p-value) were represented as * $p < 0.05$ and *** $p < 0.001$ when compared to Ti, and ^^^ $p < 0.001$ when compared to NT.

To understand the cell morphology on the surfaces, SEM images were collected after 4 and 7 days of incubation (**Figure 3.10**). The relatively dark areas on the SEM images represents the adhered cells. The adhered cells on the Ti surfaces had very thin morphology compared to the NT surfaces. Interestingly, the adhered cells on the NTZn and NTSr surfaces had long extensions which may have resulted from better anchorage provided by the nanotube architecture. These extensions also facilitated better cell communication and spreading which can influence osteoblastic differentiation when suitable environment is provided. After 7 days of incubation, all the surfaces were mostly covered by the cells. But the NTZn and NTSr surfaces still showed the extension like structures which matched the results observed after 4 days of incubation.

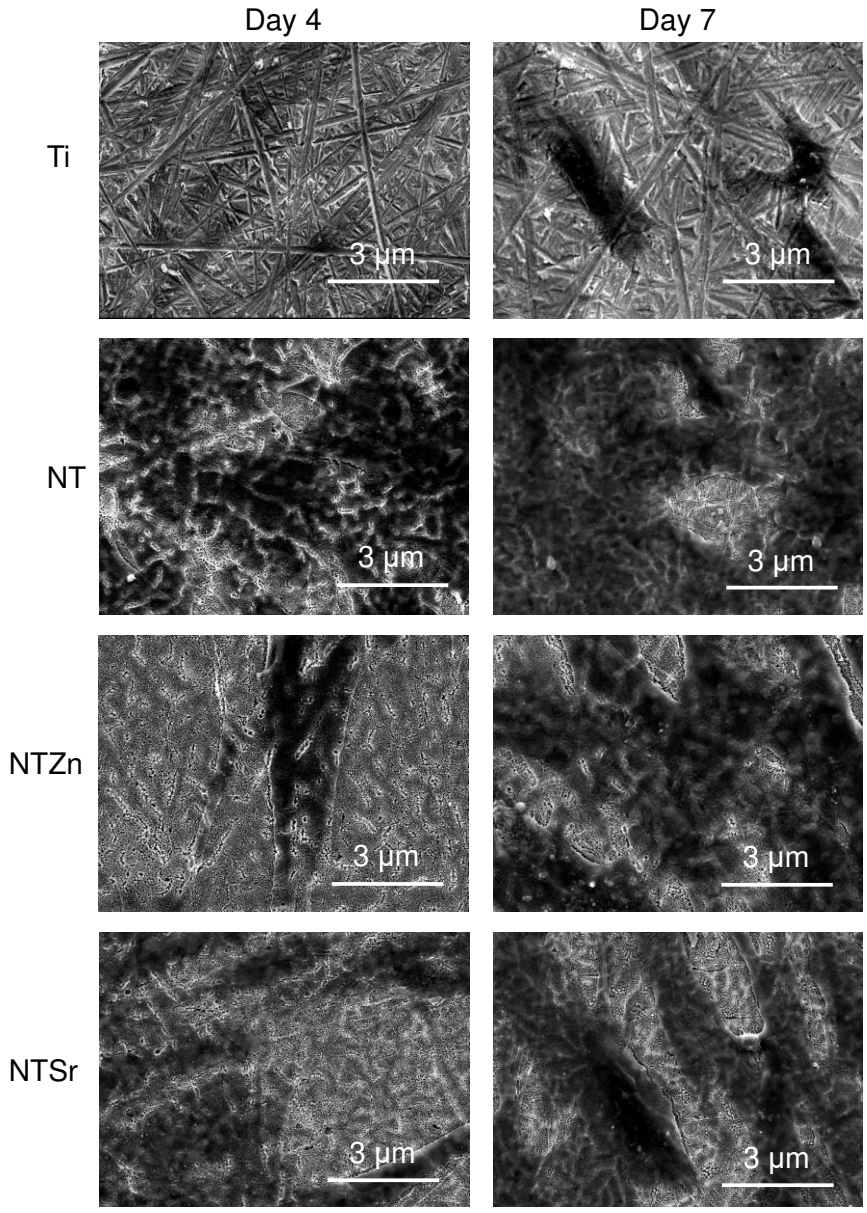

Figure 3.10. SEM images of the surfaces after 4 and 7 days of incubation with ADSCs.

To promote cell differentiation on different surfaces, differentiation media was introduced to the cells after 7 days of culture on all surfaces. Then, after 1 and 3 weeks of culture in differentiation media, several biochemical assays were used to understand the cell differentiation potential. Firstly, alkaline phosphatase (ALP) activity of the differentiated cells was evaluated (**Figure 3.11**). ALP activity is considered as an early indication of osteoblast differentiation since

the ALP activity peaks just before bone mineralization begins [32]. Hydroxyapatite is the mineral phase of bone and increased ALP activity indicates increased level of inorganic phosphate, which is a major component of hydroxyapatite [4, 32]. All the surfaces had similar level of ALP activity after 1 week (**Figure 3.11**). However, the average ALP activity was higher for the NT surfaces compared to the Ti surface. After 3 weeks, NTZn had the highest ALP activity of all the surfaces. NTSr had lower ALP activity compared to the Ti surface which indicated that the ALP activity reduced because mineralization had already begun, which aligns with the early mineralization activity by NTSr confirmed by SEM images (discussed later). From the results, it was evident that ALP activity was higher in modified surfaces which is a good indication of ADSC differentiation on these surfaces.

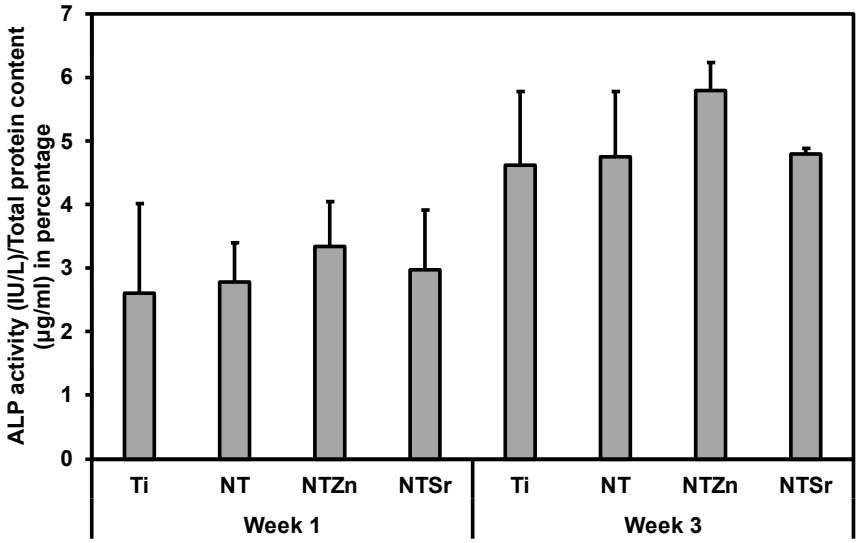

Figure 3.11. ALP activity of differentiated ADSCs on different surfaces after 1 and 3 weeks, normalized by the total protein content.

Then osteocalcin expression from the differentiated ADSCs was evaluated. Osteocalcin is a hormone released by matured osteoblasts and is a good indication of differentiation into osteoblasts [33]. Immunofluorescence images were utilized to understand the osteocalcin

expression as shown in **Figure 3.12**. The green areas are expressed osteocalcin from the differentiated ADSCs. After 1 week, osteocalcin expressed from Ti and NT surfaces were very low. However, osteocalcin released from both NTZn and NTSr were higher than the Ti surface, indicating a faster ADSC differentiation to osteoblasts on these surfaces.

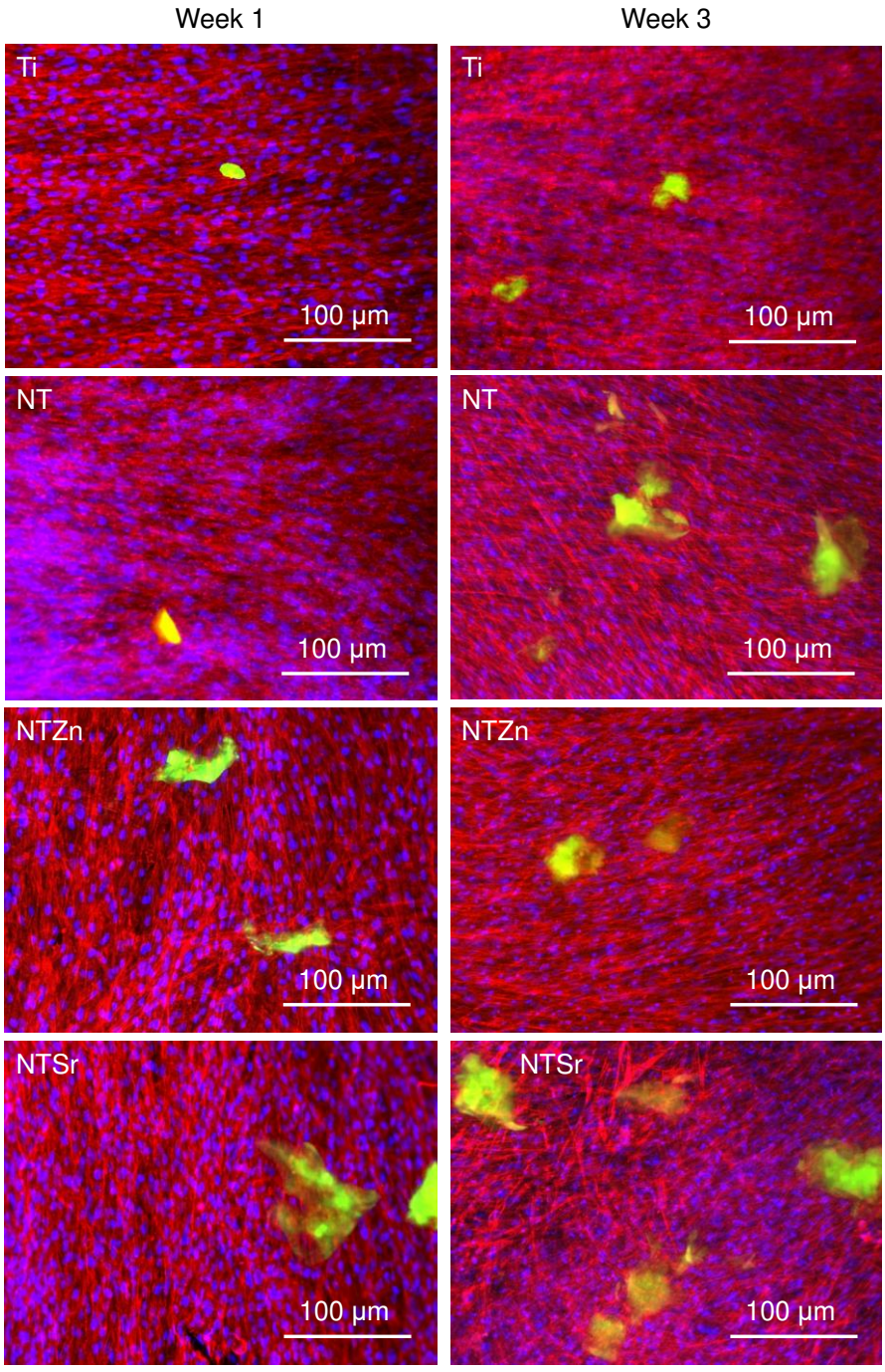

Figure 3.12. Immunofluorescence microscopic images of the surfaces after 1 and 3 weeks of culturing ADSCs with differentiation media. The green color represents osteocalcin expression by the differentiated ADSCs.

Then quantitative analysis was conducted by calculating the osteocalcin area coverage on the images normalized by the attached cells (**Figure 3.13**). NTZn and NTSr surfaces had significantly higher osteocalcin expression after 1 week, which is a strong indication of ADSC differentiation to osteoblasts. After 3 weeks, all the NT surfaces expressed significantly higher osteocalcin than unmodified Ti surface. NTSr surface had the significantly higher osteocalcin expression among the modified surfaces. From the result, it is evident that modified surfaces, especially NTSr help in better ADSC differentiation compared to unmodified Ti surface which may have resulted from the better ADSC adhesion and spreading.

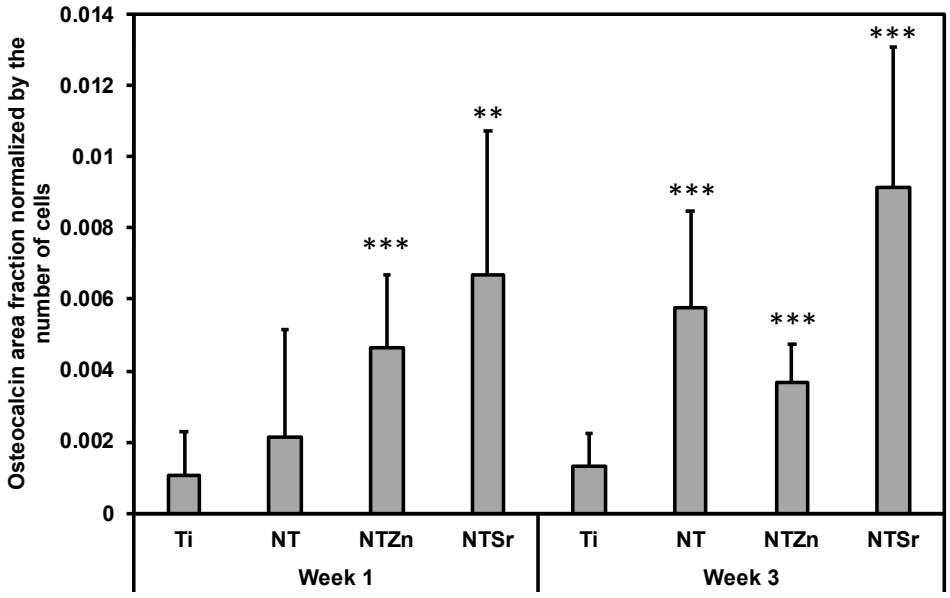

Figure 3.13. Osteocalcin area fraction normalized by the number of adhered ADSCs to the surfaces. Statistical significances (p-value) were represented as ** $p < 0.01$ and *** $p < 0.001$.

Mineralization initiates when osteoblasts start producing hydroxyapatite (HA) that is composed of calcium and phosphorus [33]. Released ALP from the osteoblasts reacts with the

contents from differentiation media resulting in HA crystals that are deposited on the surfaces as minerals [33]. These crystals are easily visible by SEM images (**Figure 3.14**). Additionally, EDS mapping is a crucial tool to confirm the contents of HA crystals. After 1 week of ADSC culturing with the differentiation media, no surfaces had any HA crystal deposition except for NTSr. (**Figure 3.14, arrow marked**). This is another strong indication of early ADSC differentiation and mineralization on the NTSr surface confirming the findings in ALP activity. After 3 weeks, all the surfaces had increased amount of crystal deposition (white circular shapes, arrow marked in **Figure 3.14**). However, the modified surfaces showed enhanced mineral deposition compared to the pure Ti surface, confirming improved ADSC differentiation and new bone matrix formation by the modified surfaces. To confirm the elemental composition of these crystals, EDS maps were collected (**Figure 3.14)**. It was observed that all the minerals were composed of calcium (Ca) and phosphorus (P), which confirmed the mineralization of ADSCs resulting from differentiation of these cells into osteoblasts. From the Ca and P maps, it was also identified that the amount of Ca and P was much higher than Ti and NT surfaces, indicating a strong influence of Zn and Sr on the ADSC differentiation.

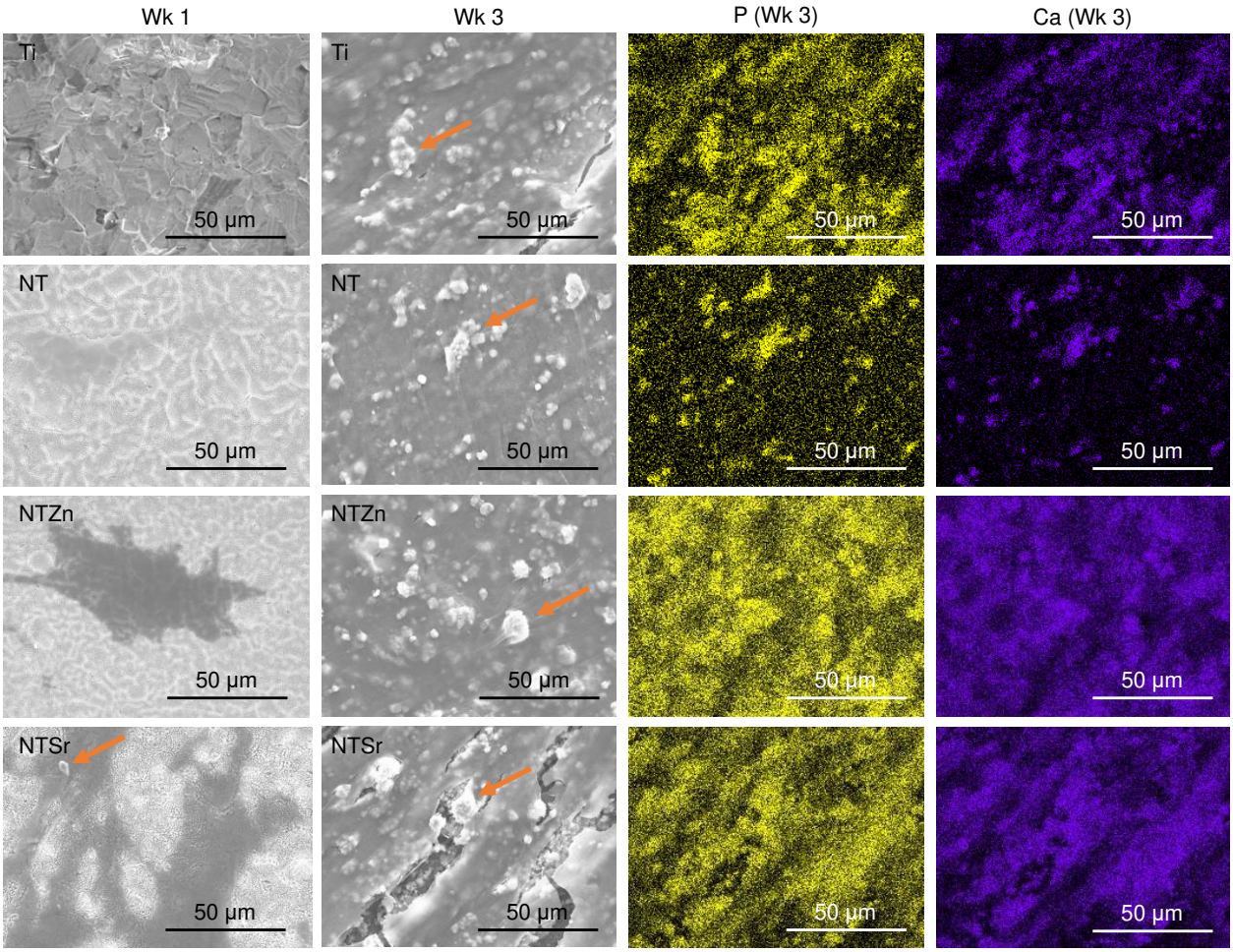

Figure 3.14. SEM images and EDS maps of the surfaces after introducing osteoblast differentiation to ADSCs. Arrow marks show the HA crystal deposition on the surfaces.

3.4 Conclusions

Nanosurface modification of titanium orthopedic implants have promising implications to improve their performance. In this work, TiO_2 nanotube (NT) arrays were fabricated on pure titanium (Ti) and doped with important signaling elements such as zinc (Zn) and strontium (Sr). Differences in surface morphology were identified from the SEM images. Both the NTZn and NTSr surfaces had crystal like structures but the shape and size of these crystals were different. EDS maps confirmed an even distribution of the doped elements with regions of high concentration. XPS spectra confirmed successful doping of the Zn and Sr along with their release

profile over a 28-day period. XRD analysis confirmed the presence of rutile and anatase phases on the modified surfaces that can help in cell compatibility. Nanoindentation technique was utilized to evaluate indentation hardness and elastic modulus of the modified surfaces. It was observed that the modified surfaces were flexible in nature that can help in accommodating dynamic response coming from the cells during cell adhesion, proliferation, and growth. Studies with ADSCs revealed enhanced cell adhesion, proliferation, and growth properties of the modified surfaces, especially the NTSr, confirming the efficacy of signaling element. The differentiation assays revealed that NTSr performed significantly better to start early and faster differentiation of the adhered ADSCs into osteoblasts. This study provided an interesting approach to fabricate titanium orthopedic implants with NTs and important signaling elements like Zn and Sr that holds potential to effectively improve the performance of orthopedic implants by improving osseointegration.

REFERENCES

1. Ralston SH. Bone structure and metabolism. Medicine. 2013 Oct 1;41(10):581-5. https://doi.org/10.1016/j.mpmed.2013.07.007
2. Albrektsson T, Johansson C. Osteoinduction, osteoconduction and osseointegration. European spine journal. 2001 Oct;10(Suppl 2):S96-101. https://doi.org/10.1007/s005860100282
3. Frassica MT, Jones SK, Diaz-Rodriguez P, Hahn MS, Grunlan MA. Incorporation of a silicon-based polymer to PEG-DA templated hydrogel scaffolds for bioactivity and osteoinductivity. Acta biomaterialia. 2019 Nov 1;99:100-9. https://doi.org/10.1016/j.actbio.2019.09.018
4. Sabino RM, Mondini G, Kipper MJ, Martins AF, Popat KC. Tanfloc/heparin polyelectrolyte multilayers improve osteogenic differentiation of adipose-derived stem cells on titania nanotube surfaces. Carbohydrate polymers. 2021 Jan 1;251:117079. https://doi.org/10.1016/j.carbpol.2020.117079
5. Gibon E, Amanatullah DF, Loi F, Pajarinen J, Nabeshima A, Yao Z, Hamadouche M, Goodman SB. The biological response to orthopaedic implants for joint replacement: Part I: Metals. Journal of Biomedical Materials Research Part B: Applied Biomaterials. 2017 Oct;105(7):2162-73. https://doi.org/10.1002/jbm.b.33734
6. Smith BS, Yoriya S, Grissom L, Grimes CA, Popat KC. Hemocompatibility of titania nanotube arrays. Journal of biomedical materials research Part A. 2010 Nov;95(2):350-60. https://doi.org/10.1002/jbm.a.32853
7. Souza JC, Sordi MB, Kanazawa M, Ravindran S, Henriques B, Silva FS, Aparicio C, Cooper LF. Nano-scale modification of titanium implant surfaces to enhance osseointegration. Acta biomaterialia. 2019 Aug 1;94:112-31. https://doi.org/10.1016/j.actbio.2019.05.045

8. Manivasagam VK, Sabino RM, Kantam P, Popat KC. Surface modification strategies to improve titanium hemocompatibility: A comprehensive review. Materials Advances. 2021;2(18):5824-42. https://doi.org/10.1039/D1MA00367D
9. Popat KC, Leoni L, Grimes CA, Desai TA. Influence of engineered titania nanotubular surfaces on bone cells. Biomaterials. 2007 Jul 1;28(21):3188-97. https://doi.org/10.1016/j.biomaterials.2007.03.020
10. Smith BS, Capellato P, Kelley S, Gonzalez-Juarrero M, Popat KC. Reduced in vitro immune response on titania nanotube arrays compared to titanium surface. Biomaterials Science. 2013;1(3):322-32. https://doi.org/10.1039/C2BM00079B
11. Chen D, Waite LC, Pierce WM. In vitro effects of zinc on markers of bone formation. Biological trace element research. 1999 Jun;68:225-34. https://doi.org/10.1007/BF02783905
12. Huo K, Zhang X, Wang H, Zhao L, Liu X, Chu PK. Osteogenic activity and antibacterial effects on titanium surfaces modified with Zn-incorporated nanotube arrays. Biomaterials. 2013 Apr 1;34(13):3467-78. https://doi.org/10.1016/j.biomaterials.2013.01.071
13. Li Y, Xiong W, Zhang C, Gao B, Guan H, Cheng H, Fu J, Li F. Enhanced osseointegration and antibacterial action of zinc-loaded titania-nanotube-coated titanium substrates: In vitro and in vivo studies. Journal of Biomedical Materials Research Part A. 2014 Nov;102(11):3939-50. https://doi.org/10.1002/jbm.a.35060
14. Shi J, Li Y, Gu Y, Qiao S, Zhang X, Lai H. Effect of titanium implants with strontium incorporation on bone apposition in animal models: A systematic review and meta-analysis. Scientific Reports. 2017 Nov 14;7(1):15563. https://doi.org/10.1038/s41598-017-15488-1
15. Gao C, Li C, Wang C, Qin Y, Wang Z, Yang F, Liu H, Chang F, Wang J. Advances in the induction of osteogenesis by zinc surface modification based on titanium alloy substrates for

medical implants. Journal of Alloys and Compounds. 2017 Dec 5;726:1072-84. https://doi.org/10.1016/j.jallcom.2017.08.078

16. Bhattacharjee A, Goodall E, Pereira BL, Soares P, Popat KC. Zinc (Zn) Doping by Hydrothermal and Alkaline Heat-Treatment Methods on Titania Nanotube Arrays for Enhanced Antibacterial Activity. Nanomaterials. 2023 May 10;13(10):1606. https://doi.org/10.3390/nano13101606
17. Tsuji W, Rubin JP, Marra KG. Adipose-derived stem cells: Implications in tissue regeneration. World journal of stem cells. 2014 Jul 7;6(3):312. http://dx.doi.org/10.4252/wjsc.v6.i3.312
18. Le Guehennec L, Lopez-Heredia MA, Enkel B, Weiss P, Amouriq Y, Layrolle P. Osteoblastic cell behaviour on different titanium implant surfaces. Acta biomaterialia. 2008 May 1;4(3):535-43. https://doi.org/10.1016/j.actbio.2007.12.002
19. Zareidoost A, Yousefpour M, Ghaseme B, Amanzadeh A. The relationship of surface roughness and cell response of chemical surface modification of titanium. Journal of Materials Science: Materials in Medicine. 2012 Jun;23:1479-88. https://doi.org/10.1007/s10856-012-4611-9
20. Chouirfa H, Bouloussa H, Migonney V, Falentin-Daudré C. Review of titanium surface modification techniques and coatings for antibacterial applications. Acta biomaterialia. 2019 Jan 1;83:37-54. https://doi.org/10.1016/j.actbio.2018.10.036
21. Benjwal P, Kar KK. One-step synthesis of Zn doped titania nanotubes and investigation of their visible photocatalytic activity. Materials Chemistry and Physics. 2015 Jun 15;160:279-88. https://doi.org/10.1016/j.matchemphys.2015.04.038

22. Meng J, Yang G, Liu L, Song Y, Jiang L, Wang S. Cell adhesive spectra along surface wettability gradient from superhydrophilicity to superhydrophobicity. Science China Chemistry. 2017 May;60:614-20. https://doi.org/10.1007/s11426-016-9031-8

23. Fan H, Guo Z. Bioinspired surfaces with wettability: biomolecule adhesion behaviors. Biomaterials science. 2020;8(6):1502-35. https://doi.org/10.1039/C9BM01729A

24. Dou XQ, Zhang D, Feng C, Jiang L. Bioinspired hierarchical surface structures with tunable wettability for regulating bacteria adhesion. ACS nano. 2015 Nov 24;9(11):10664-72. https://doi.org/10.1021/acsnano.5b04231

25. Wang G, Li J, Lv K, Zhang W, Ding X, Yang G, Liu X, Jiang X. Surface thermal oxidation on titanium implants to enhance osteogenic activity and in vivo osseointegration. Scientific reports. 2016 Aug 22;6(1):31769. https://doi.org/10.1038/srep31769

26. Thamaphat K, Limsuwan P, Ngotawornchai B. Phase characterization of TiO_2 powder by XRD and TEM. Agriculture and Natural Resources. 2008 Dec 31;42(5):357-61. https://li01.tci-thaijo.org/index.php/anres/article/view/244620

27. Sun Q, Hou Y, Chu Z, Wei Q. Soft overcomes the hard: Flexible materials adapt to cell adhesion to promote cell mechanotransduction. Bioactive Materials. 2022 Apr 1;10:397-404. https://doi.org/10.1016/j.bioactmat.2021.08.026

28. Rho JY, Tsui TY, Pharr GM. Elastic properties of human cortical and trabecular lamellar bone measured by nanoindentation. Biomaterials. 1997 Oct 1;18(20):1325-30. https://doi.org/10.1016/S0142-9612(97)00073-2

29. Piao F, Yokoyama K, Ma N, Yamauchi T. Subacute toxic effects of zinc on various tissues and organs of rats. Toxicology letters. 2003 Nov 1;145(1):28-35.https://doi.org/10.1016/S0378-4274(03)00261-3

30. Nielsen SP. The biological role of strontium. Bone. 2004 Sep 1;35(3):583-8. https://doi.org/10.1016/j.bone.2004.04.026

31. Uchide N, Ohyama K, Bessho T, Toyoda H. Lactate dehydrogenase leakage as a marker for apoptotic cell degradation induced by influenza virus infection in human fetal membrane cells. Intervirology. 2009 Jun 10;52(3):164-73. https://doi.org/10.1159/000224644

32. Cowden K, Dias-Netipanyj MF, Popat KC. Effects of titania nanotube surfaces on osteogenic differentiation of human adipose-derived stem cells. Nanomedicine: Nanotechnology, Biology and Medicine. 2019 Apr 1;17:380-90. https://doi.org/10.1016/j.nano.2019.01.008

33. Moser SC, van der Eerden BC. Osteocalcin—A versatile bone-derived hormone. Frontiers in endocrinology. 2019 Jan 10;9:794. https://doi.org/10.3389/fendo.2018.00794

CHAPTER 4/DUAL DOPING OF ZINC AND STRONTIUM ON TITANIA NANOTUBE SURFACES FOR SIMULTANEOUS ANTIBACTERIAL ACTIVITY WITH IMPROVED STEM CELL COMPATIBILITY

4.1 Introduction

Orthopedic implants are wonders of modern science to treat bone related injuries and damages. Mostly, these implants are made of metals such as stainless steel, chromium-cobalt alloys, or titanium and their alloys. Titanium (Ti) implants offers unique advantages over other materials owing to their superior biocompatibility and biological inertness along with lightweight and excellent corrosion resistance properties [1]. These properties made Ti a popular choice for orthopedic implant applications in recent years. However, these implants often suffer from two major complications- bacterial infection and poor osseointegration. These failure points and potential remedies utilizing the nanotechnology were discussed in the earlier chapters.

During implant surgery, bacteria can adhere to the implant surface and start proliferating on the surface using the nutrients from surrounding tissues. The bacteria biofilm layer is formed as a result which provides a safe environment for the proliferating bacteria. For this reason, bone progenitor cells such as mesenchymal stem cells (MSC) cannot adhere to the implant surface, resulting in implant failure. The implant failure can also happen due to poor osseointegration which is defined as a failed anchorage between the implant and bone tissue. Since implants are foreign material to host, an immediate immune response takes place to cover the surface with fibrous tissue instead of MSCs. The fibrous capsule deters new bone tissue formation around the implant surface and thus the implant fails.

To overcome these implant failures, the use of nanotechnology to fabricate TiO_2 nanotube arrays (NT) was discussed in **Chapter 2**. NT significantly influences the surface properties of Ti-

based implants. NT surfaces are superhydrophilic compared to the pure Ti surface. The NTs also make the implant surface softer and allows the adhering stem cells to spread more by providing effective anchorage points. When important trace elements such as zinc (Zn) and strontium (Sr) were doped on the surfaces, unique morphological features were observed. Zn doped NTZn surface could significantly reduce Gram-positive *S. aureus* and Gram-negative *P. aeruginosa* adhesion to the surface. These results were discussed in **Chapter 2**. After that, Zn and Sr were separately doped on NT surfaces using hydrothermal treatment to evaluate cell compatibility. The results indicated that NTZn and NTSr could significantly improve the osseointegration properties of the implants by allowing early osteogenic differentiation of adipose derived stem cells (ADSC). These results were discussed thoroughly in **Chapter 3**.

The next goal of the project was to fabricate a NT surface by simultaneous doping of Zn and Sr to evaluate both the antibacterial activity and cell compatibility. Simultaneous doping of multiple trace elements for achieving various bioactivity is lacking in the literature. Often, researchers use complex and multiple doping techniques to prepare bioactive implant surface. However, the hydrothermal method utilized in this study is a simple and easy process for element doping on Ti surfaces that can provide effective results. Therefore, Zn and Sr were simultaneously doped on NT by using the hydrothermal process to prepare NTZnSr surface. Surface morphology, elemental composition, and wettability were evaluated using scanning electron microscopy (SEM), X-ray photoelectron spectroscopy (XPS), and contact angle measurements. Then the surfaces were evaluated for antibacterial activity by incubating with Gram-positive *S. aureus* and Gram-negative *P. aeruginosa* for 24 h. Results indicated that the NTZnSr could significantly reduce both bacteria adhesion and biofilm formation. Then ADSCs were cultured on the surface for 4 and 7 days to evaluate cell adhesion, proliferation, and differentiation properties to

osteoblasts. The results indicated that NTZnSr initially had lower cell adhesion compared to Ti, but the cell differentiation was faster and higher confirmed by osteocalcin expression and osteoblast mineralization studies. These results clearly indicate that simultaneous doping of Zn and Sr by the easy hydrothermal treatment is an effective way to improve the bioactivity of Ti implants.

4.2 Materials and methods

4.2.1 TiO_2 nanotube fabrication

TiO_2 nanotube arrays were fabricated on commercially available pure Ti surfaces following a method described earlier [2]. Firstly, 2 cm X 2 cm Ti surfaces were cut and polished using silicon carbide sheets. Then they were soaked in acetone for 3 min to clean oil, wax, and other impurities from the surface. Then they were sonicated with acetone for 10 min in a bath sonicator for thorough cleaning. After that the surfaces were cleaned further with DI water, soap, and isopropyl alcohol. Then the surfaces were sonicated with isopropyl alcohol and DI water for 10 min each. Then the surfaces were cleaned again with DI water and dried inside a hood. An electrolytic cell was used for anodization where a solution containing 95% diethylene glycol (DEG, Thermo Fisher Scientific Chemicals Inc., Ward Hill, MA, USA), 2% hydrofluoric acid (HF, 48%, KMG Electronic Chemicals, Inc., Houston, TX, USA), and 3% DI water was used. Cleaned Ti surfaces were hooked to the electrolytic cell as anodes and similar sized cleaned platinum surfaces were hooked as cathode using alligator clips. 55 kV of electrical voltage was supplied to the electrolytic cells for 22 h. After that, the surfaces were cleaned thoroughly with running DI water and isopropyl alcohol and dried inside a hood. A set of control NT sample was prepared after that by annealing the

surfaces at 530º C for 3 h with 15º C/min of temperature increment. Cleaned Ti surfaces were also used as controls.

4.2.2 Simultaneous doping of zinc and strontium

Zinc (Zn) and strontium (Sr) were doped on the as anodized surfaces using a hydrothermal method. After anodization, firstly, the surfaces were taken into a polytetrafluoroethylene (PTFE) lined hydrothermal autoclave reactor with a solution containing 0.1 M zinc acetate. Then the reactor was heated inside an oven at 200º C for 1 h. After that, the Zn doped surfaces were cleaned thoroughly with running DI water to remove excess Zn. Then the surfaces were taken inside another PTFE lined hydrothermal autoclave reactor with a solution containing 0.02 M strontium acetate octahydrate and heated inside an oven at 200º C for 1 h. After that, the surfaces were cleaned again thoroughly with running DI water to remove excess Sr. Finally, the surfaces were annealed at 530º C for 3 h with 15º C/min of temperature increment using a furnace to prepare NTZnSr.

4.2.3 Surface characterization

- Surface morphology of Ti, NT, and NTZnSr was characterized using a JEOL JSM-6500F field emission scanning electron microscope (FESEM). The probe current during image collection was 7 A with an operating voltage of 15 kV. Different magnifications ranging from 500x to 20,000x were used to collect scanning electron microscopic (SEM) images. Working distance, contrast, and brightness were adjusted as needed to ensure high-quality image collection.

- To evaluate doped Zn and Sr distribution, energy-dispersive X-ray spectroscopy (EDS) maps were collected using an Oxford SDD EDS detector connected to the FESEM. EDS spectra, layered images, and elemental maps were collected and analyzed using the Oxford Aztec software.
- Surface chemistry was analyzed by evaluating X-ray photoelectron spectroscopy (XPS) survey spectra collected by using a PHI Physical Electronics PE-5800 X-ray Photoelectron Spectrometer with an Al Kα X-ray source. The survey spectra for each surface were collected from 0 V to 1100 V. MultiPak (version 9.6.1.7) software was used to analyze the spectra and calculate relative atomic weight % (at%) of each element on the surfaces.
- Wettability of the surfaces were evaluated by collecting static water contact angle using a Ramé-Hart goniometer (Ramé-Hart Instrument Co., Succasunna, NJ, USA). A water droplet of approximately 10 µl was dropped on each surface was dropped on each surface using a micrometer syringe and an image of the droplet was collected using the camera system of the goniometer. Then DROPimage software was used to measure the contact angle value from the image.

4.2.4 Bacteria culture

Gram-positive *Staphylococcus aures* (*S. aureus*, ATCC6538) and Gram-negative *Pseudomonas aeruginosa* (*P. aeruginosa*, ATCC10145) bacterial strains were cultured in tryptic soy broth (TSB) for at 37º C. The bacterial concentration was monitored by taking absorbance values of the bacteria culture at 562 nm using a plate reader. The bacteria culture was continued until a bacterial concentration of 10^9 colony forming units (CFU)/ml was achieved. Prior to bacterial adhesion and morphological studies, the surfaces were taken into 48-well plates and

sterilized for 10 min using 70% ethanol. Then the surfaces were thoroughly washed with DI water for 3 times followed by further sterilization under UV light for 30 min inside a biosafety hood. Then the surfaces were further washed 2 times with phosphate buffer saline (PBS) and dried inside the hood. The bacterial culture was diluted to 10^6 CFU/ml using TSB media. Then the surfaces were incubated with the diluted bacteria solution for 6 h and 24 h at 37º C inside an incubator.

4.2.5 Bacteria adhesion

After 6 h and 24 h of incubation, bacteria solution was removed, and the surfaces were washed for 3 times using PBS to remove any unadhered bacteria to the surface. Then the surfaces were incubated at room temperature for 15 min in a stain solution containing a 1:1 ratio of propidium iodide (dead bacteria stain) and Syto 9 (live bacterial stain) (3 µL/mL in PBS, ThermoFisher Scientific, Waltham, MA, USA). Then the stain solution was removed, and the surfaces were washed with PBS to remove excess stain. After that the adhered bacteria were fixed by incubating the surfaces with 3.7% formaldehyde (Fisher Chemical, Fair Lawn, NJ, USA) for 15 min at room temperature. Then formaldehyde was removed, and the surfaces were washed with PBS twice. Immediately, the surfaces were imaged using a fluorescence microscope. ImageJ software was used to analyze the area fraction coverage by the bacteria on each surface. All the procedures from staining to image collection were conducted in dark.

4.2.6 Bacteria morphology

After 6 h and 24 h incubation with bacteria solution, the surfaces were washed with PBS for 3 times. Then the surfaces were incubated with a primary fixative solution containing 3% glutaraldehyde (Sigma-Aldrich, St. Louis, MO, USA), 0.1 M sucrose (Sigma-Aldrich, St. Louis,

MO, USA), and 0.1 M sodium cacodylate (Electron Microscopy Sciences, Hatfield, PA, USA) in DI water for 45 min. After that the surfaces were incubated for 10 min with a buffer solution containing the fixative solution but without the glutaraldehyde. Then the surfaces were dehydrated in 35%, 50%, 70%, and 100% ethanol for 10 min each. Then, SEM images were collected from each surface using the FESEM. Prior to imaging, the surfaces were gold coated (10 nm) using a Denton Vacuum Desk II Gold Sputter Coater to improve the conductivity.

4.2.7 Adipose derived stem cell (ADSC) culture

Adipose derived stem cells (ADSC) were generously donated to the lab by Dr. Kimberly Cox-York from the Department of Food Science and Human Nutrition at the Colorado State University. The cells were cultured in a growth media at 37°C inside an incubator. The growth media was prepared by mixing 90% MEM Alpha Modification (1×, cytiva, Marlborough, MA, USA), 9% fetal bovine serum (FBS), and 1% penicillin-streptomycin. Prior to cell seeding, the surfaces were sterilized following the method described above. Finally, the ADSCs were seeded on the surfaces at a final concentration of 20,000 ADSC/well.

4.2.8 Cytotoxicity evaluation of the surfaces

Cytotoxicity of the surfaces were evaluated by using a lactate dehydrogenase (LDH) based indicator assay. First, ADSC (passage 5) were cultured using the growth media. Then sterilized surfaces were seeded with cells maintaining a final concentration of 20,000 cells/well. After that the surfaces were incubated with seeded cells at 37°C for 48 h inside an incubator. 2 control samples were produced- spontaneous release where cells were seeded in an empty well, and maximum release where cells were seeded in an empty well but were lysed using a 10% lysis

buffer after 24 h of cell culture. Then 50 µl of cell suspension was taken out from each well and taken into a 96 well plate. After that manufacturer's protocol was followed to collect absorbance values for each surface which corresponds to the cytotoxicity imparted by the surfaces towards the cells.

4.2.9 Cell adhesion, proliferation, and morphology

Cell adhesion and proliferation on the surfaces were evaluated by fluorescence microscopy. After 4 and 7 days of culturing the surfaces with ADSCs, the surfaces were rinsed with PBS for 3 times to remove unadhered cells. Then adhered cells were fixed to the surfaces using 3.7% formaldehyde in PBS for 15 min followed by 3 times wash with PBS. Then the cells were permealized using 1% triton-X in PBS followed by 2 times wash with PBS. After that, actin filaments of the adhered cells were stained using 70 nM rhodamine phalloidin (Cytoskeleton, Inc., Denver, CO, USA) for 25 min. Then 300 nm nuclear stain DAPI (ThermoFisher Scientific, Waltham, MA, USA) was added to stain the nucleus of the adhered cells. After that the stain solution was removed the surfaces were washed with PBS for 2 times. Then a fluorescence microscope was used to collect images of the surfaces. ImageJ software was used to quantify the number of adhered cells to the surfaces.

For evaluating the morphology of the surfaces, a procedure similar to the bacterial morphology evaluation was followed that is described earlier.

4.2.10 Osteogenic differentiation of ADSC

Osteogenic differentiation was introduced to the ADSCs after 7 days of culture with the growth media. The differentiation media prepared by supplementing the growth media with 10^{-8}

M dexamethasone (Sigma, 98 %), 50 μg/mL ascorbic acid (Sigma, 100 %), and 6 mM β-glycerol phosphate (Sigma, 98 %) and added to the wells after 7 days of culture. The differentiation media was changed every other day for 1 and 3 weeks. After 1 and 3 weeks of culture with the differentiation media, alkaline phosphatase (ALP) activity, total protein content, immunofluorescence (IF) microscopic images, SEM images, and EDS maps were collected to evaluate ADSC differentiation to osteoblasts when cultured with the surfaces.

- After 1 and 3 weeks, QuantiChrom™ Alkaline Phosphatase Assay Kit (DALP-250) (BioAssay Systems, Hayward, CA) was used for colorimetric determination of serum alkaline phosphatase. To evaluate total protein content, a Micro BCA Protein Assay Kit (ThermoFisher Scientific, Waltham, MA, USA) was used. Then serum alkaline phosphatase was normalized by the total protein content to evaluate ALP activity.
- IF images from each surface were collected after 1 and 3 weeks to evaluate osteocalcin expression by the differentiated ADSCs. At first, the surfaces were washed 3 times with PBS after the culture. Then adhered cells were fixed with 3.7% formaldehyde in PBS for 15 min followed by 3 rinses with PBS. Then the cells were permealized using 1% triton-X in PBS followed by two rinses with PBS. After that, a blocking serum containing 10% bovine serum albumin (BSA) in PBS was added. The cells were incubated with the blocking serum for 30 min followed by a rinse with PBS. Then the cells were incubated with a primary osteocalcin antibody solution (1:100 in 1% BSA) followed by 3 times wash with PBS. Then the cells were incubated with a secondary FITC conjugated antibody (1:200 in 1% BSA) for 45 min followed by two PBS rinses. After that the cells were incubated with actin filament stain rhodamine phalloidin and nuclear stain DAPI following the procedure described earlier. Then IF images were collected using a fluorescence

microscope. ImageJ software was used to evaluate osteocalcin expression coverage area normalized by adhered cell numbers for each surface.

- SEM images were collected to analyze mineralization of osteoblasts that forms hydroxyapatite crystals on the surfaces. After 1 and 3 weeks, the surfaces were washed with PBS for 3 times followed by the cell fixation procedure for SEM image collection described earlier. EDS maps were also collected followed by the procedure described earlier to confirm mineral content of the deposited crystals on the surfaces.

4.2.11 Statistical analysis

For morphological analysis, at least 5 SEM images were collected from each group (n_{min}=5). For rest of the surface characterization (EDS, XPS, contact angle) at least 3 samples were used from each group (n_{min}=3). For bacteria study, at least 9 fluorescence microscopic images (n_{min}=9) and 5 SEM images (n_{min}=5) were collected from each group. For cell adhesion and proliferation study, at least 9 fluorescence microscopic images (n_{min}=9) and 5 SEM images (n_{min}=5) were collected from each group. At least 3 samples from each group were used for ALP activity, total protein, and calcium assays (n_{min}=3). Finally, at least 9 immunofluorescence microscopic images (n_{min}=9) and at least 5 SEM images (n_{min}=5) were collected for cell differentiation studies. To evaluate statistically significant difference between sample groups, analysis of variance (ANOVA) was conducted followed by post-hoc T-test ($\alpha = 0.05$).

4.3 Results and discussions

Titanium (Ti) implants are often used for orthopedic implant applications due to their superior mechanical properties. But they often suffer from poor antibacterial and osseointegration

properties. Several studies were conducted to improve antibacterial activity or osseointegration properties of Ti surfaces, but there remains a lack of studies that focused on improving both properties simultaneously. To achieve the goal of improving both antibacterial and osseointegration properties of Ti implants, first TiO_2 nanotubes (NT) were fabricated on pure Ti surfaces in this work. Then important antibacterial and cell signaling elements, zinc (Zn) and strontium (Sr) were doped simultaneously on the NT surfaces using a very simple hydrothermal method. Morphological analysis of the surfaces revealed that Ti surfaces did not have any unique surface properties, rather had a relatively smooth surface (**Figure 4.1**). After the nanotube fabrication, tubular shaped nanotubes were found on the NT surface that were evenly distributed throughout the surface. These nanotubes were 80-100 nm long with a diameter ranging from 30 to 50 nm. The nanotubes were formed as a result of continuous anodization and etching processes. When Ti is anodized in an electrolytic cell, a TiO_2 layer is produced and simultaneously pits formed on this layer due to the electric field dissolution of the oxide layer. At the same time, fluoride (F^-) ions from the hydrofluoric acid (HF) in the electrolyte solution starts etching the TiO_2 layer and over a period of 22 h forms the evenly distributed nanotube arrays on the surface [3-4]. Then hydrothermal treatment was conducted to dope Zn and Sr ions on these NT surfaces. During the first treatment, Zn ions from the zinc acetate solution forms ZnO that gets embedded to the TiO_2 layer. After that, during the Sr doping process, Sr ions from the strontium acetate octahydrate solution forms $SrTiO_3$ that also gets embedded to the TiO_2 layer. SEM images revealed that the NTZnSr surface possess both the small hexagonal Zn crystals and longer Sr crystals (**Figure 4.1**) which match with the earlier works (**Chapter 2 and 3**).

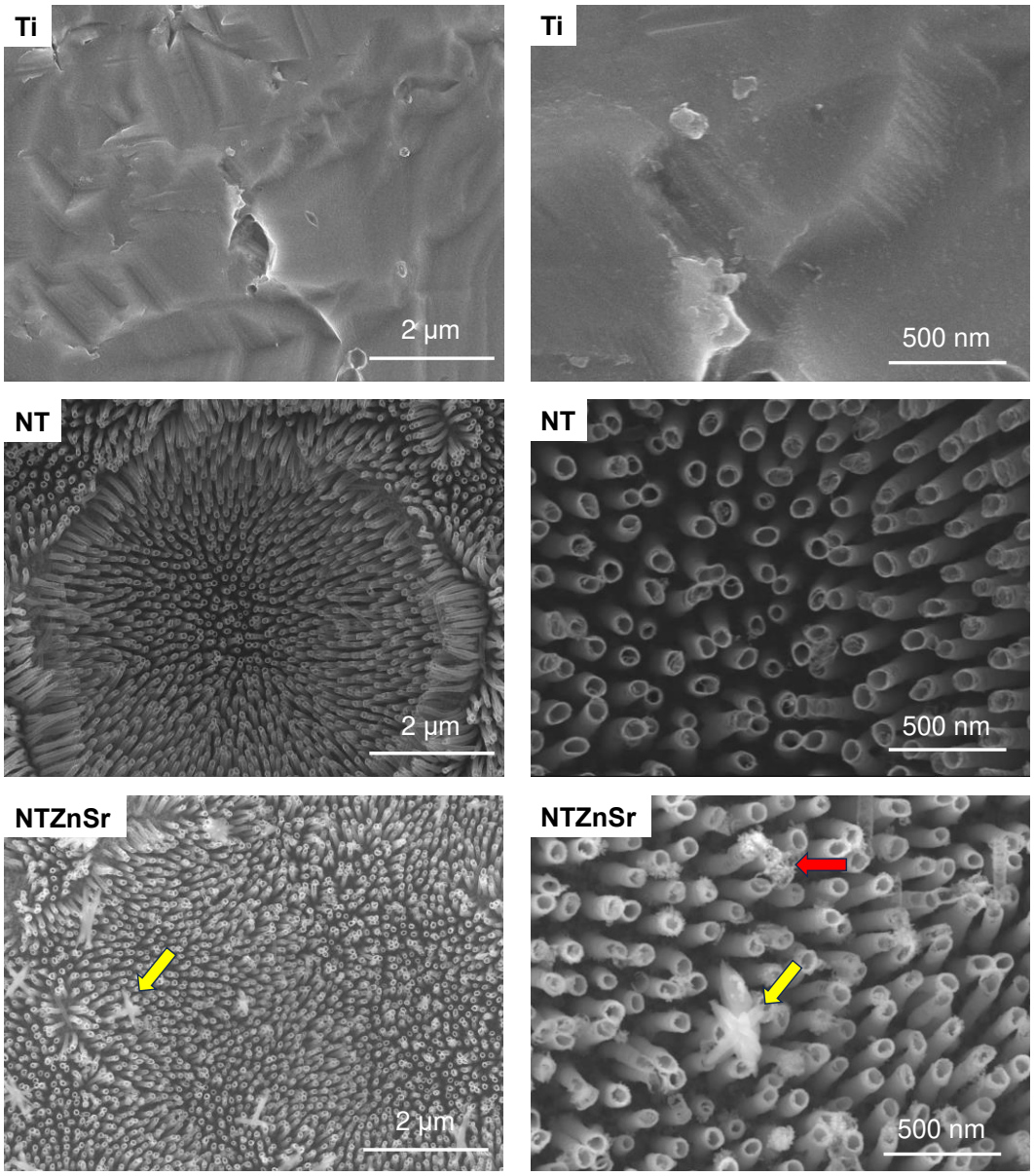

Figure 4.1. SEM images of different surfaces. Zn and Sr crystals are indicated by red and yellow arrows respectively.

Antibacterial activity and cell compatibility of the modified surfaces depends on a uniform distribution of important bactericidal and cell signaling element distribution throughout the surface. To evaluate Zn and Sr ion distribution on NTZnSr surface, EDS maps of these elements were collected. **Figure 4.2** shows the Zn and Sr elemental maps on NTZnSr surface. Zn and Sr were found evenly distributed throughout the surface. A trace amount of fluoride (F) was observed

on the surface which resulted from SrF_2 (confirmed by XPS later) which formed during the hydrothermal treatment by a reaction between residual F^- ion from anodization and Sr ion from strontium acetate octahydrate solution.

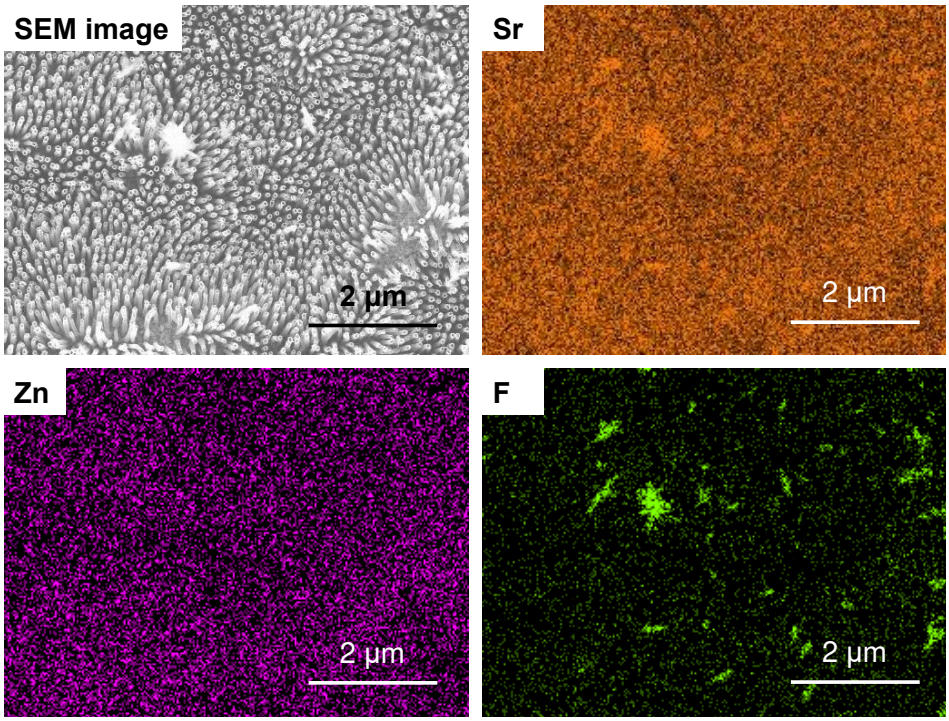

Figure 4.2. Elemental EDS maps of NTZnSr surface.

Since the EDS maps confirmed a uniform distribution of Zn and Sr on the NTZnSr surface, it was imperative to evaluate the concentration of these elements on the surface by taking XPS survey spectra (**Figure 4.3**). The NTZnSr spectra had Zn2p peaks at 1023 and 1043 eV which indicates the presence of Zn on the surface. The spectra also had peaks at 354 and 267 eV that are peaks for Sr3s and Sr3p2 respectively that confirmed the presence of Sr on the surface. These peaks were absent on the Ti and NT surfaces. The Ti2p and O1s at 458 and 530 eV peaks were present on all the surfaces. On the NTZnSr, a peak at 133 eV indicates the presence of SrF_2, which aligns with the EDS finding discussed earlier.

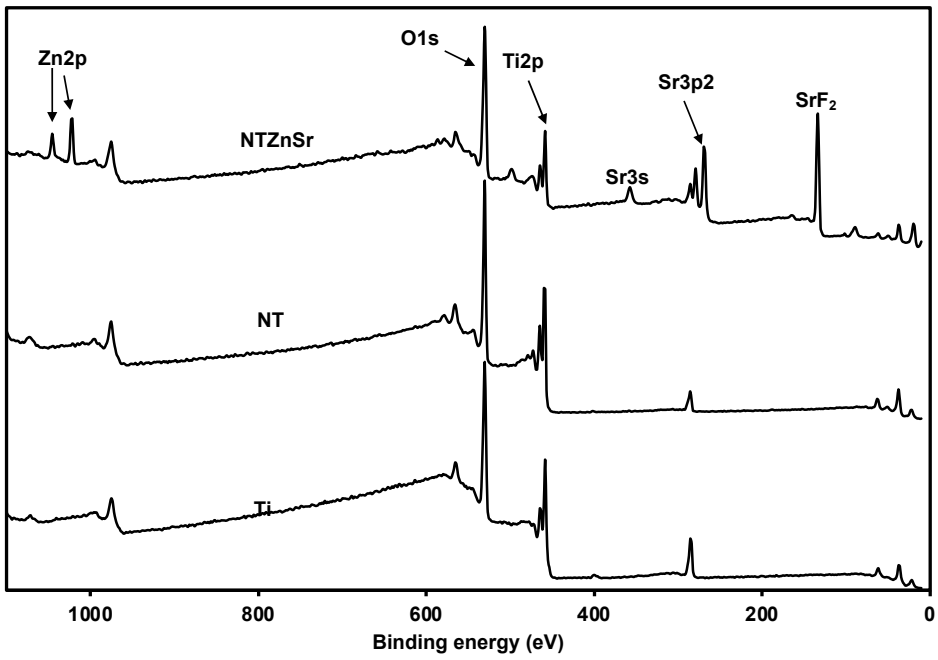

Figure 4.3. XPS survey spectra and relative atomic weight percentage (at%) of different elements on the surfaces.

When relative atomic weight percentage (at%) was calculated from the survey spectra, approximately 17% Sr and 6.4% Zn was found on the surface (**Table 4.1**). Due to the secondary hydrothermal treatment with strontium acetate that increased the amount of Sr on the surface, relative Zn amount was reduced on NTZnSr. These percentages are highly controllable by changing the concentration of the hydrothermal solution and altering the doping sequence between Zn and Sr.

Table 4.1. Relative atomic weight percentages (at%) of different surfaces.

	Ti	NT	NTZnSr
Zn	0	0	17.03 ± 1.53
Sr	0	0	6.43 ± 1.63

Surface wettability is a crucial factor for implant surface. It has been reported that extremely wettable surfaces such as superhydrophilic and superhydrophobic surfaces can repel bacterial adhesion [5]. These surfaces also have been reported to increase cell adhesion in a previous study [6]. The wettability of the prepared NTZnSr surface was evaluated by taking static contact angle measurement. When the contact angle $\theta < 90°$, the surface is hydrophilic, but when $\theta < 10°$, then the surfaces are designated as superhydrophilic [1]. Ti had a θ value of around 60º, making it a hydrophilic surface (**Figure 4.4**). The contact angle for NT was 0º, making it a superhydrophilic surface. The nanotubular structures creates a capillary force on the water droplet that penetrates the droplet, and the contact angle reduces [1]. The NTZnSr surface also had a contact angle of 0º, due to a similar reason as NT surfaces where nanotubular structures penetrates the water droplet. Since the NTZnSr surface was superhydrophilic it may help in reducing bacterial adhesion but improve cell adhesion and differentiation.

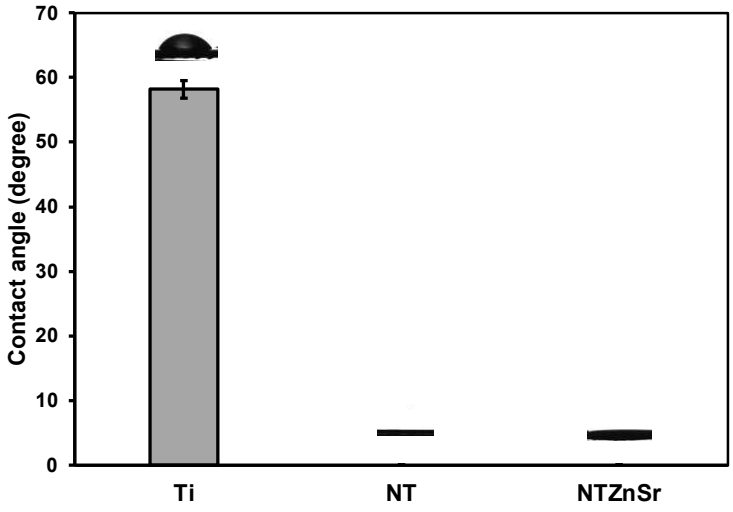

Figure 4.4. Wettability of different surfaces.

Antibacterial activity is a key factor to reduce bacterial infection and contamination on orthopedic implant surfaces. Surgery mediated implant infection is one of the major reason implant failures happen. However, if the implant surface can reduce the bacterial adhesion and biofilm formation on the surface at the early stage after implant surgery, the failure rate can be reduced. After 24 h of incubation with Gram-negative *P. aeruginosa*, Ti was almost covered with both live and dead *P. aeruginosa* adhered to the surfaces which was revealed by the live/dead fluorescence microscopic images (**Figure 4.5**). However, *P. aeruginosa* adhesion was lower on NT and NTZnSr surfaces. From the quantitative analysis, it was clear that NT and NTZnSr surfaces had significantly less live *P. aeruginosa* adhesion on these surfaces compared to Ti. For dead *P. aeruginosa*, NTZnSr had significantly lower *P. aeruginosa* adhesion compared to Ti. This result indicated that the inclusion of Zn on the NT surface helped in reducing *P. aeruginosa* adhesion significantly.

When the surfaces were incubated with Gram-positive *S. aureus*, a higher amount of bacteria adhesion was observed for all the surfaces compared to the Gram-negative *P. aeruginosa*.

This might have resulted due to the relative size difference of these two bacteria. *S. aureus* is a round-shaped bacteria that are relatively smaller in size compared to the rod-shaped *P. aeruginosa*. This size difference probably allowed *S. aureus* to colonize the gaps between nanotubes, especially in the grain boundaries where the gap is larger because of the upward orientation of the nanotubes. Interestingly, the number of adhered *S. aureus* were lower in NT and NTZnSr compared to Ti. When quantitative analysis was performed, it was evident that the number of adhered bacteria was significantly reduced by both NT and NTZnSr surfaces. From the quantitative analysis of both the bacterial adhesion studies, it was also observed that NTZnSr performed better that NT surfaces. This is because of the presence of Zn and strongly suggest the efficacy of Zn presence on the surface to impart antibacterial properties.

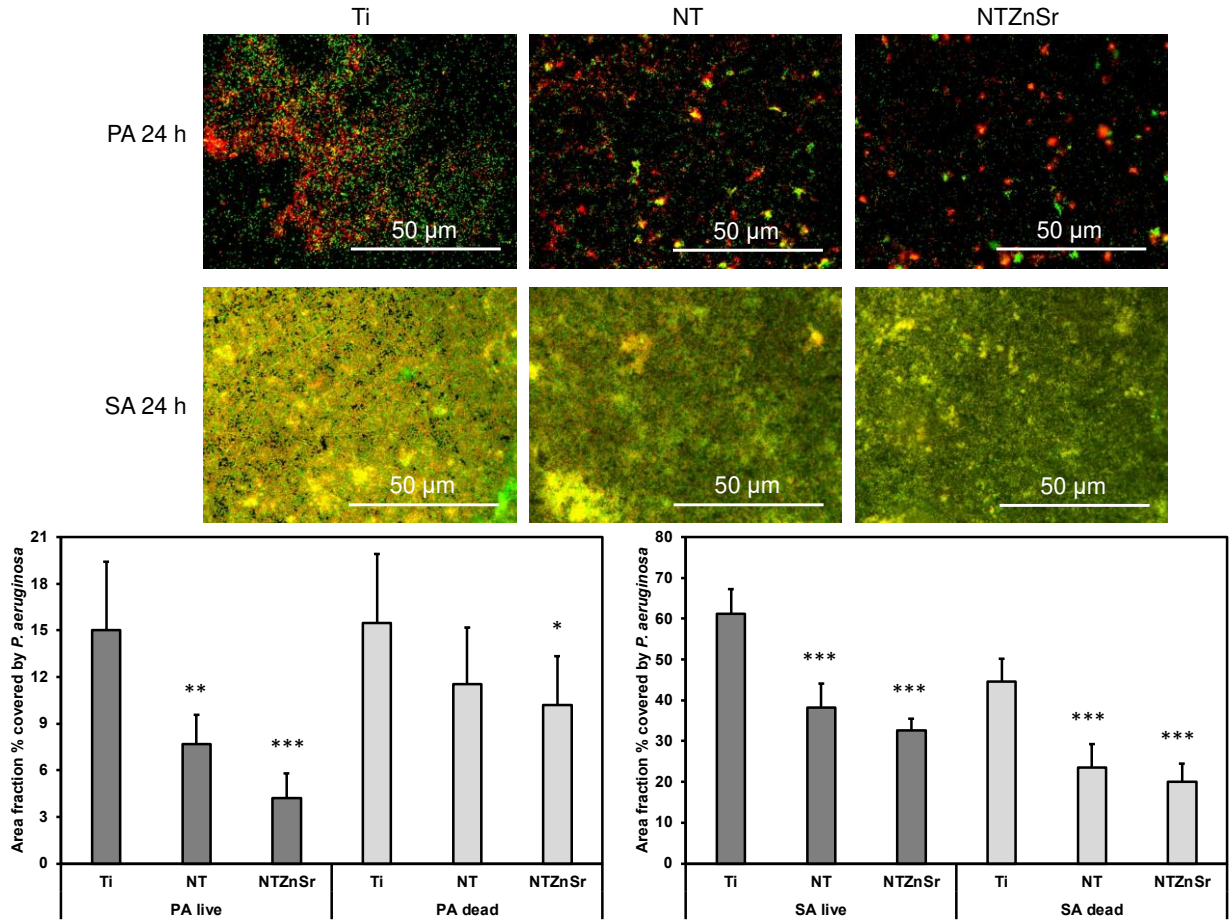

Figure 4.5. Fluorescence microscopic images of the surfaces after incubating 24 h with *P. aeruginosa* (PA) and *S. aureus* (SA). Quantitative analysis charts are also presented. Statistical significances (*p*-value) were represented as * $p < 0.05$, ** $p < 0.01$ and *** $p < 0.001$.

To evaluate morphological features of bacterial adhesion to the surfaces, SEM images were collected after 24 h of incubation with *P. aeruginosa* and *S. aureus* (**Figure 4.6**). After 24 h, *P. aeruginosa* could form a thick biofilm on the Ti surface, which indicates the inefficiency of Ti surface to reduce bacterial adhesion. However, NT and NTZnSr both reduced *P. aeruginosa* adhesion and biofilm formation during the same incubation period as Ti. A similar finding was observed for *S. aureus*, where Ti surfaces had a higher amount of *S. aureus* adhesion after 24 h of incubation. The adhered bacterial formed multiple layers of colony on the Ti surface. However, the adhesion was drastically reduced on NT and NTZnSr surfaces. These results align with the

observations from fluorescence microscopic images, confirming that NT and NTZnSr surfaces have better antibacterial activity compared to unmodified Ti surface.

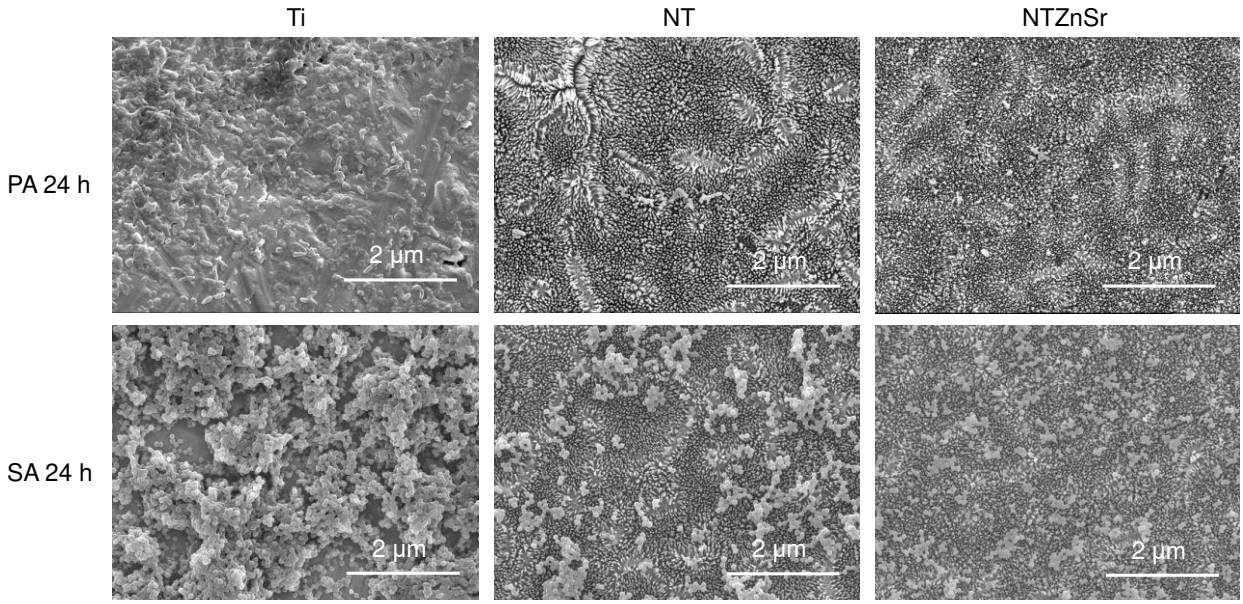

Figure 4.6. SEM images of different surfaces incubated for 24 h with *P. aeruginosa* (PA) and *S. aureus* (SA).

The modified NTZnSr surface had both Zn and Sr. Overdose of these elements have been reported to cause undesirable health complications. Previous reports also indicated that Zn and Sr are released from the surfaces to the surrounding environments. So, it was imperative to assess the cytotoxicity of the NTZnSr surface. Following the LDH assay protocol, the absorbance value of the NTZnSr surface was aligned with the spontaneous release (SR) absorbance value (**Figure 4.7**). SR indicates the cytotoxicity when no cells were damaged. So, being at the same level with SR value strongly suggest that NTZnSr surface do not provide any apparent cytotoxicity towards ADSCs. Also, the absorbance value for NTZnSr was significantly different than maximum release (MR). When all the cells were damaged by using a lysis buffer, maximum LDH get released to the environment and the absorbance value also gets higher. So, when the absorbance value of the

surface is significantly lower than the MR, it serves as a secondary confirmation for no apparent cytotoxicity.

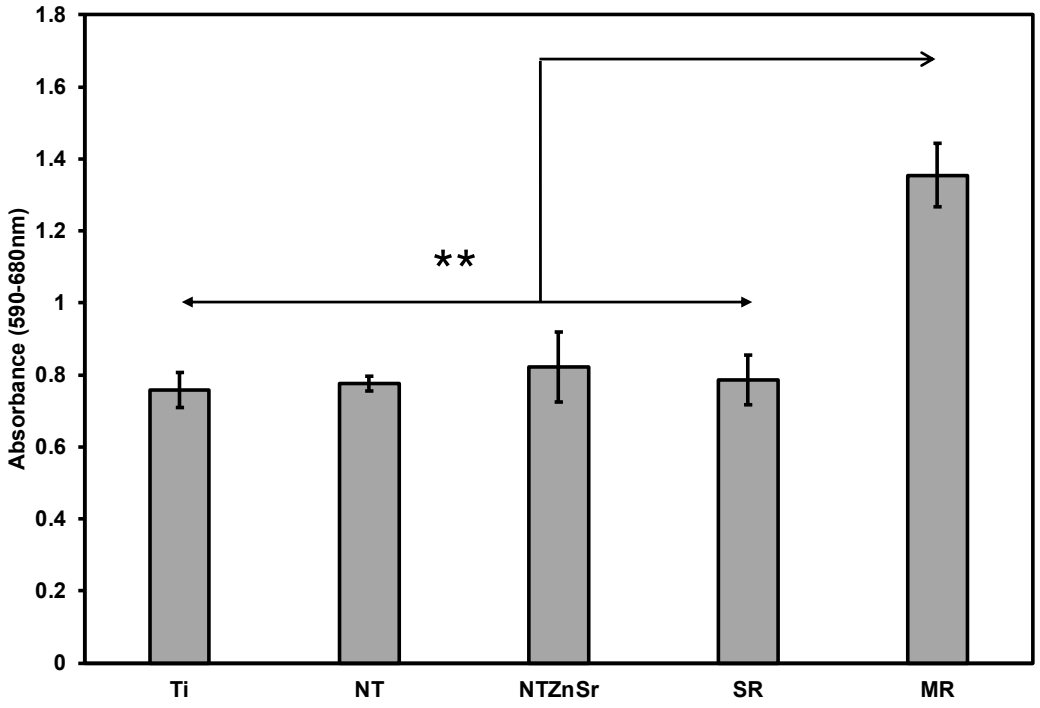

Figure 4.7. Cytotoxicity of different surfaces. Statistical significance (*p*-value) was represented as ** $p < 0.01$.

Next, cell compatibility studies were conducted on the surfaces to evaluate stem cell adhesion, proliferation, and morphology. After incubating the surfaces for 4 and 7 days with ADSCs, fluorescence microscopic images were collected (**Figure 4.8)**. During this period, Ti had the most ADSC adhesion compared to the modified surfaces. This is because the cells need to accommodate to the modified surfaces because of the presence of nanotubes and change in wettability. However, the cells created long extensions on the modified surfaces which was not missing for the cells on the Ti surface. This is a clear indication of better cell spreading on the modified surfaces which is helpful for cell differentiation in the later stages.

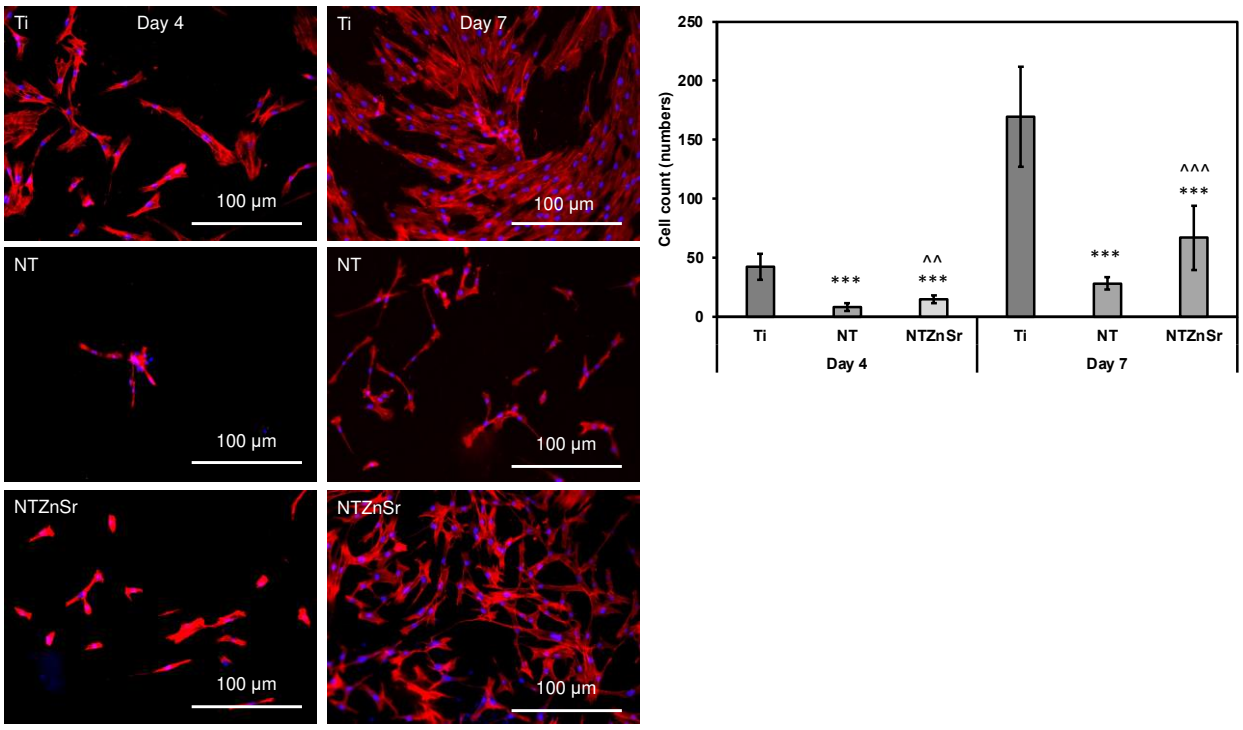

Figure 4.8. Fluorescence microscopic images of different surfaces. Statistical significances (*p*-value) were represented as *** $p < 0.001$ when compared to Ti; as ^^ $p < 0.01$ and ^^^ $p < 0.001$ when compared to NT.

Scanning electron microscopic (SEM) images were collected of the surfaces after 4 and 7 days of incubation. A similar observation was made from the SEM images (**Figure 4.9**). There was less cell adhered to the modified NT and NTZnSr surfaces compared to Ti. However, the cells long extensions. These long extensions can help in differentiation to osteoblastic phenotypes, which is desirable for orthopedic implants to enhance bone healing. From the SEM images it was also observed that the cells on the modified surfaces were thicker than the cells adhered to the Ti surfaces which can also help in enhancing differentiation of these cells to osteoblasts.

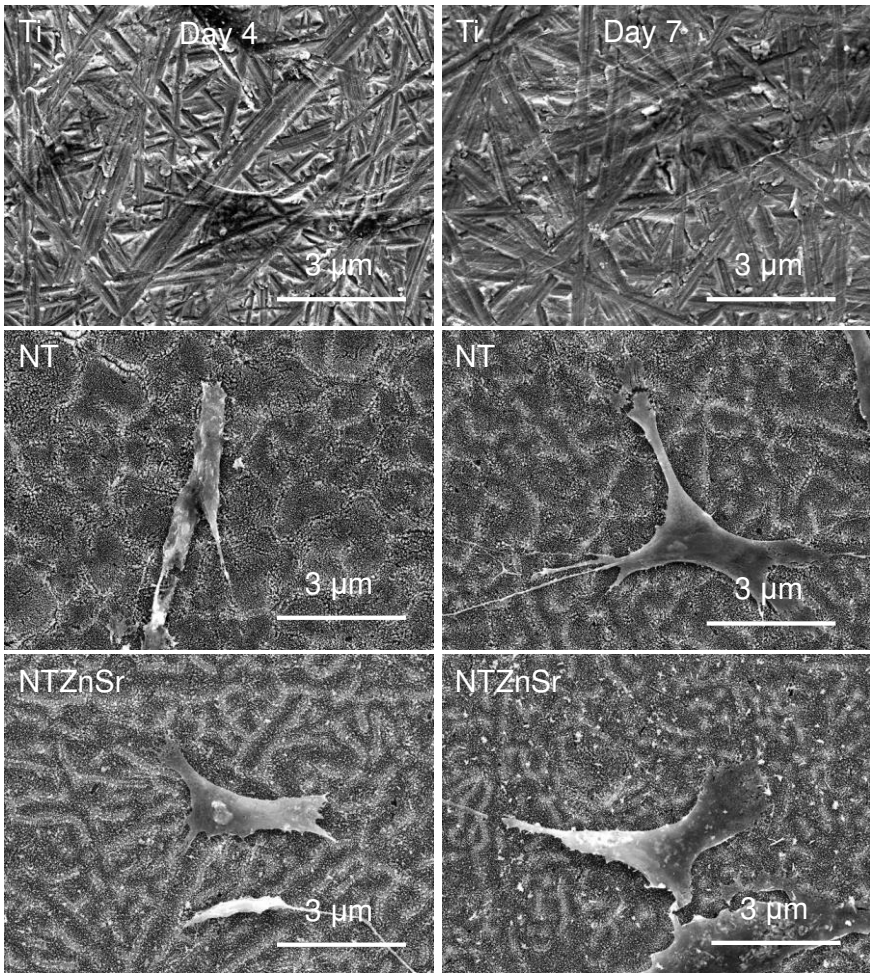

Figure 4.9. SEM images of different surfaces.

To evaluate cell differentiation capability of the surfaces, a differentiation media was added to the adhered cells to the surfaces. Alkaline phosphatase (ALP) activity is one of the early indicators of ADSC differentiation to osteoblasts. Differentiated ADSCs release ALP which is an enzyme in bone matrix and considered a key component for bone mineralization [7]. When ALP activity was evaluated for the surfaces, no significant difference was observed between the surfaces after 1 week (**Figure 4.10**). However, Ti showed higher ALP activity compared to the modified surfaces. Due to the early differentiation of ADSCs on the modified surfaces, the ALP activity was probably suppressed after 1 week. On the other hand, after 3 weeks, all the surfaces showed mostly

identical ALP activity which was lower than the values obtained after 1 week. This happened for the same reason as the ALP activity was suppressed after the mineralization process started the mature osteoblasts.

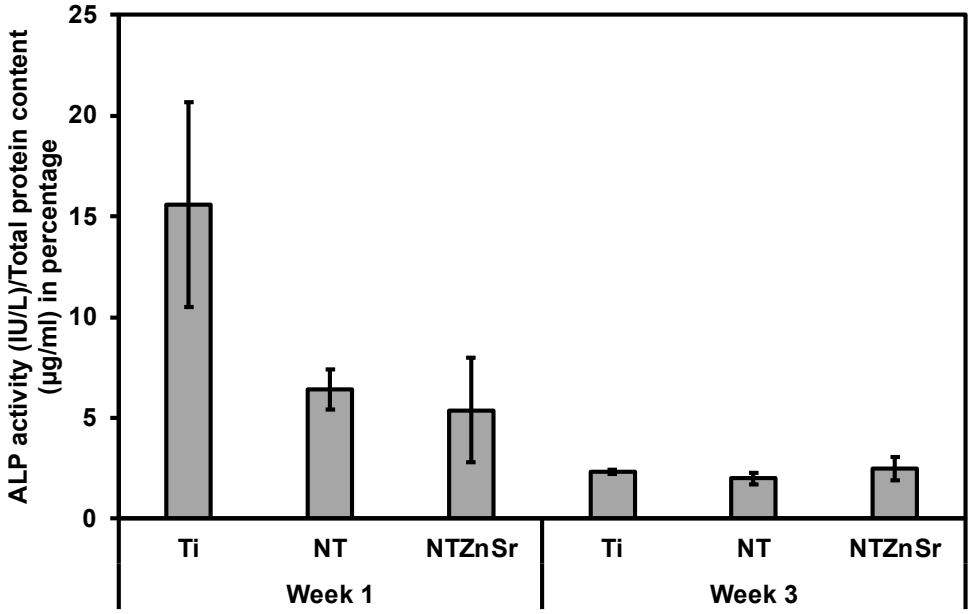

Figure 4.10. ALP activity normalized by total protein content of different surfaces.

Calcium deposition is another key indicator for ADSC differentiation to osteoblasts. Calcium content analysis indicates bone mineralization which results from hydroxyapatite (HA) formation by the differentiated osteoblasts [8]. Bone mineralization by HA is a late indicator and thus important to evaluate ADSC differentiation on different surfaces. After 1 week of culturing cells with the differentiated media, NTZnSr had significantly more calcium content compared to Ti (**Figure 4.11**). This indicates that the adhered cells to the NTZnSr surfaces already differentiated and started the cell mineralization. This is also an indicator of bone matrix formation by the differentiated cells. After 3 weeks, all the surfaces had similar calcium content as most of the cells have been differentiated by this time.

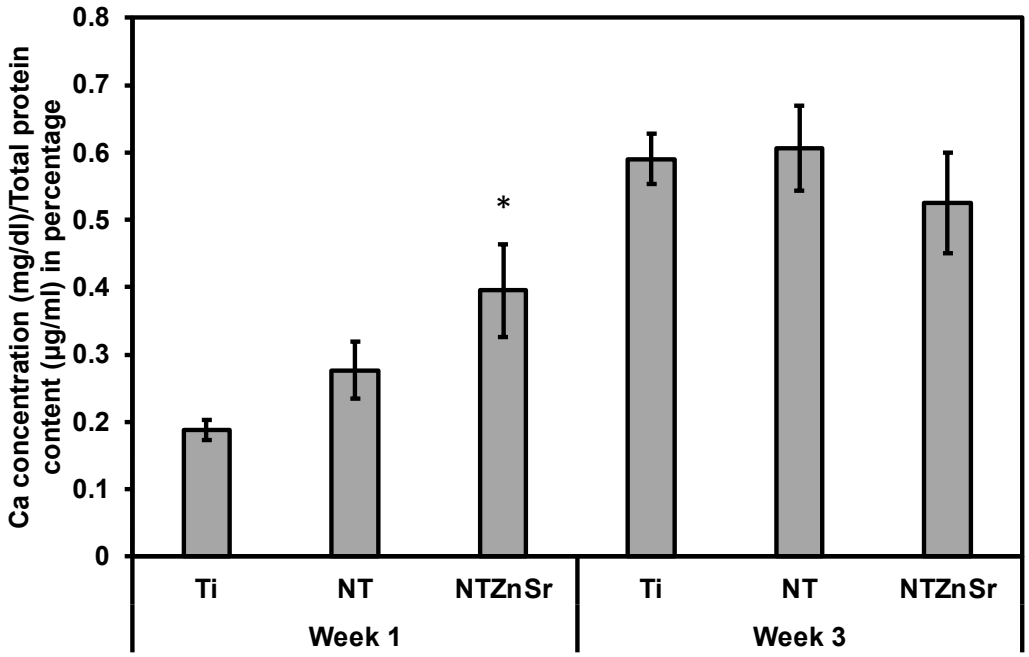

Figure 4.11. Calcium content normalized by total protein content of differentiated ADSCs. Statistical significance (*p*-value) was represented as * $p < 0.05$.

Osteocalcin is a hormone released by the matured osteoblasts. Higher osteocalcin expression refers to better ADSC differentiation to osteoblasts and effective osseointegration properties. After 1 week incubation with the osteogenic differentiation media, the NTZnSr showed significantly higher osteocalcin expression compared to the Ti and NT surfaces (**Figure 4.12**).

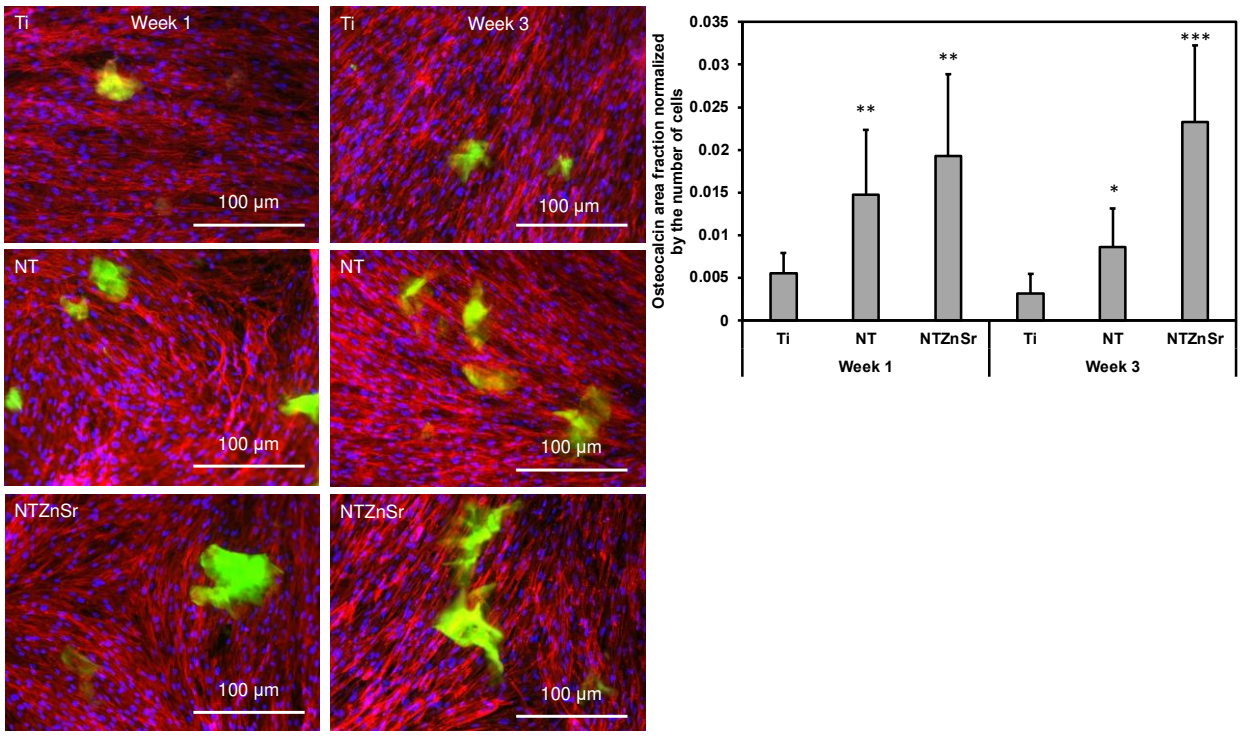

Figure 4.12. Immunofluorescence images of different surfaces and osteocalcin expression area normalized by the number of cells. Statistical significances (*p*-value) were represented as * $p < 0.05$, ** $p < 0.01$, and *** $p < 0.001$.

Matured osteoblasts undergo mineralization to form bone matrix that is important for bone healing. When the implant surfaces are cell compatible, they direct bone progenitor cells such as ADSCs to differentiate into osteoblasts. So, examining mineral deposition through SEM and EDS is a key identifier of ADSC differentiation on the surfaces. **Figure 4.13** presents the SEM images and EDS elemental maps after 1 and 3 weeks of incubating the cells with the differentiation media. After 1 week, Ti and NT surfaces had a lot of adhered cells, but no mineral deposition were found. Since the deposited minerals are hydroxyapatite crystals formed by calcium (Ca) and phosphorus (P), the EDS maps were tracking these elements. Interestingly, the NTZnSr surface had trace amount of Ca identified in EDS (arrow marked in **Figure 4.13**), which is a strong indication of early ADSC differentiation to osteoblasts and aligns with the findings from ALP activity, Ca content and osteocalcin expression. After 3 weeks, all the surfaces had increased amount of mineral

deposition (**Figure 4.13, arrow marked**). EDS maps confirmed these minerals are mainly Ca and P confirming the osteoblast differentiation of adhered ADSCs.

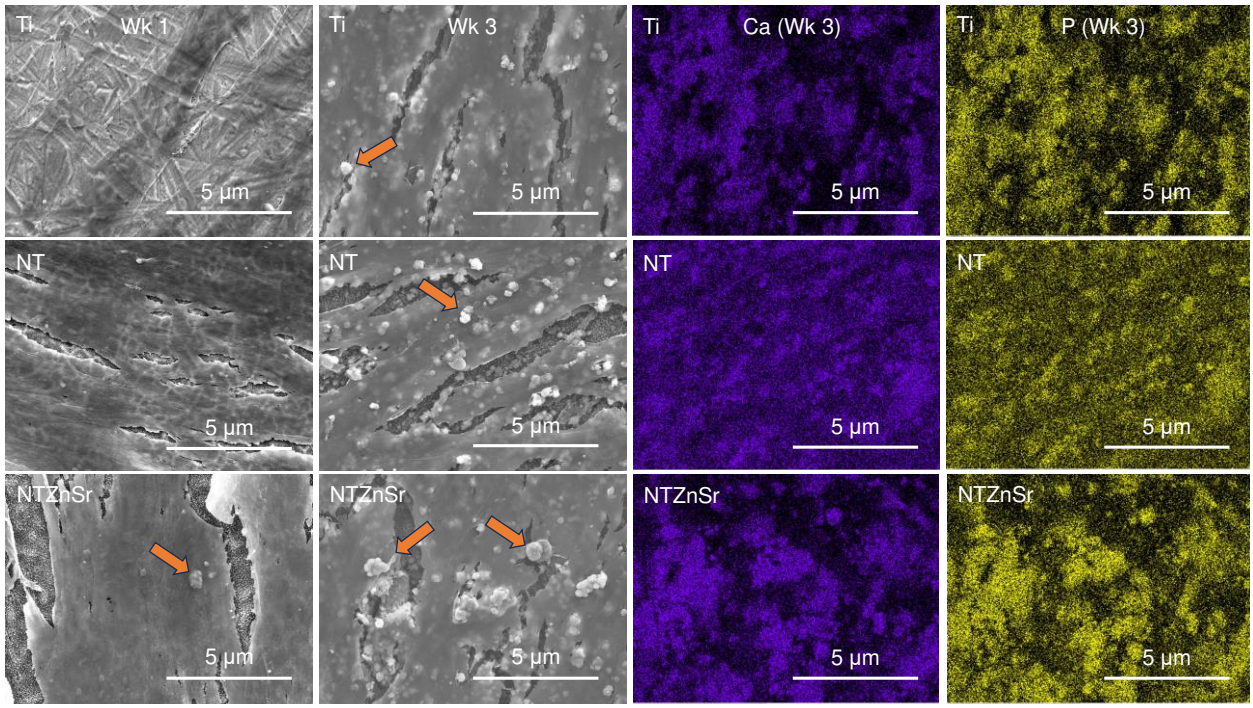

Figure 4.13. SEM images after 1 and 3 weeks of incubation with differentiation media. EDS maps of Ca and P are also presented after 3 weeks of incubation.

4.4 Conclusions

Titanium is a popular material for orthopedic implant applications due to its excellent corrosion resistance, lightweight properties, and superior biocompatibility. However, often these implants fail due to poor osseointegration and bacterial adhesion, causing revision surgeries for the patients which is painful and burdensome. To overcome these problems, nanostructured surface modification approaches had been investigated previously that improved the antibacterial activity and cell adhesion properties. However, these nanostructured surfaces could not provide important biological signals for the adhered stem cells to differentiate into osteoblasts to form bone matrix around the implant surface. In this work, two important signaling and antibacterial elements (Zn

and Sr) were deposited on the TiO_2 nanotube (NT) surface by using hydrothermal treatment method. This process is relatively simple to dope NT surfaces with the Zn and Sr and does not require complex machineries. The prepared NTZnSr exhibited interesting morphological characteristics where both Zn and Sr had unique crystal structures. The XPS and EDS revealed that around 17% Sr and 6% Zn were present on the surface. When the surface was incubated with bacteria for 24 h, it was found that NTZnSr significantly reduced both Gram-positive and Gram-negative bacteria adhesion and biofilm formation on the surface. The NTZnSr also showed enhanced cell adhesion compared to the NT surface. The adhered cells had long extension identified through the fluorescence images that indicates better cell spreading on the NTZnSr surface. Finally, the adhered cells to the NTZnSr could undergo excellent and faster differentiation identified from the ALP activity, Ca content, and osteocalcin expression, mineralization studies. These results strongly suggest the efficacy of the Zn and Sr presence on the NT surfaces to improve both antibacterial activity and osseointegration properties of the orthopedic implants.

REFERENCES

1. Sabino, R. M., Mondini, G., Kipper, M. J., Martins, A. F., & Popat, K. C. (2021). Tanfloc/heparin polyelectrolyte multilayers improve osteogenic differentiation of adipose-derived stem cells on titania nanotube surfaces. *Carbohydrate polymers*, *251*, 117079. https://doi.org/10.1016/j.carbpol.2020.117079
2. Smith, B. S., Yoriya, S., Grissom, L., Grimes, C. A., & Popat, K. C. (2010). Hemocompatibility of titania nanotube arrays. *Journal of biomedical materials research Part A*, *95*(2), 350-360. https://doi.org/10.1002/jbm.a.32853
3. Bai, J., Zhou, B., Li, L., Liu, Y., Zheng, Q., Shao, J., ... & Zou, L. (2008). The formation mechanism of titania nanotube arrays in hydrofluoric acid electrolyte. *Journal of materials science*, *43*, 1880-1884. https://doi.org/10.1007/s10853-007-2418-8
4. Benjwal, P., & Kar, K. K. (2015). One-step synthesis of Zn doped titania nanotubes and investigation of their visible photocatalytic activity. *Materials Chemistry and Physics*, *160*, 279-288. https://doi.org/10.1016/j.matchemphys.2015.04.038
5. Dou, X. Q., Zhang, D., Feng, C., & Jiang, L. (2015). Bioinspired hierarchical surface structures with tunable wettability for regulating bacteria adhesion. *ACS nano*, *9*(11), 10664-10672. https://doi.org/10.1021/acsnano.5b04231
6. Meng, J., Yang, G., Liu, L., Song, Y., Jiang, L., & Wang, S. (2017). Cell adhesive spectra along surface wettability gradient from superhydrophilicity to superhydrophobicity. *Science China Chemistry*, *60*, 614-620. https://doi.org/10.1007/s11426-016-9031-8

7. Sugawara, Y., Suzuki, K., Koshikawa, M., Ando, M., & Iida, J. (2002). Necessity of enzymatic activity of alkaline phosphatase for mineralization of osteoblastic cells. *Japanese Journal of Pharmacology*, *88*(3), 262-269. https://doi.org/10.1254/jjp.88.262
8. de Souza, R. F. B., de Souza, F. C. B., Thorpe, A., Mantovani, D., Popat, K. C., & Moraes, Â. M. (2020). Phosphorylation of chitosan to improve osteoinduction of chitosan/xanthan-based scaffolds for periosteal tissue engineering. *International journal of biological macromolecules*, *143*, 619-632. https://doi.org/10.1016/j.ijbiomac.2019.12.004

CHAPTER 5/SELECTIVE DETECTION OF GRAM-NEGATIVE BACTERIA AND ANTIBACTERIAL PROPERTIES OF COLORIMETRIC POLYDIACETYLENE NANOFIBERS[1]

5.1 Introduction

Colorimetric biosensors made by polydiacetylene nanofibers have been of great interest in developing novel strategies of rapid and in situ detection to bacterial infection that is a major concern for human fatalities around the world. Previous studies have focused on bacterial detection and the sensitivity of the detection that the PDA biosensors can offer. However, the selectivity of the detection to different bacterial strains has not been well understood. With the recent emergence of multiple drug-resistance bacterial strains, selective detection of bacteria demands more attention and cutting-edge tools. In this study, a polydiacetylene (PDA) nanofiber biosensor prepared via electrospinning was found effectively to offer selective detection of Gram-negative bacteria such as *Escherichia coli* and *Pseudomonas aeruginosa* via a rapid blue-to-red colorimetric change. The quantification of the colorimetric changes suggested that the biosensor selectivity was effective in identifying with Gram-negative bacteria over Gram-positive bacteria (*Staphylococcus aureus*). The selectivity was likely due to structural differences between Gram-positive bacteria and Gram-negative bacteria such as cell outer layer thickness, as well as different extracellular polymeric substances (EPS) released by different bacteria. In addition, the nanofiber biosensor demonstrated superior antibacterial properties that were evaluated using bacteria staining and electron

[1]This work was published in *Journal of Materials Science* and is reproduced here with permission [1].

microscopic techniques. A comprehensive analysis of the interaction between the PDA nanofibers and different bacteria was presented to provide insightful understanding of selective detection and antibacterial properties of the PDA nanofibers. The results suggested that PDA nanofibers have great potential in medical textiles, personal protective equipment, and other biomedical applications.

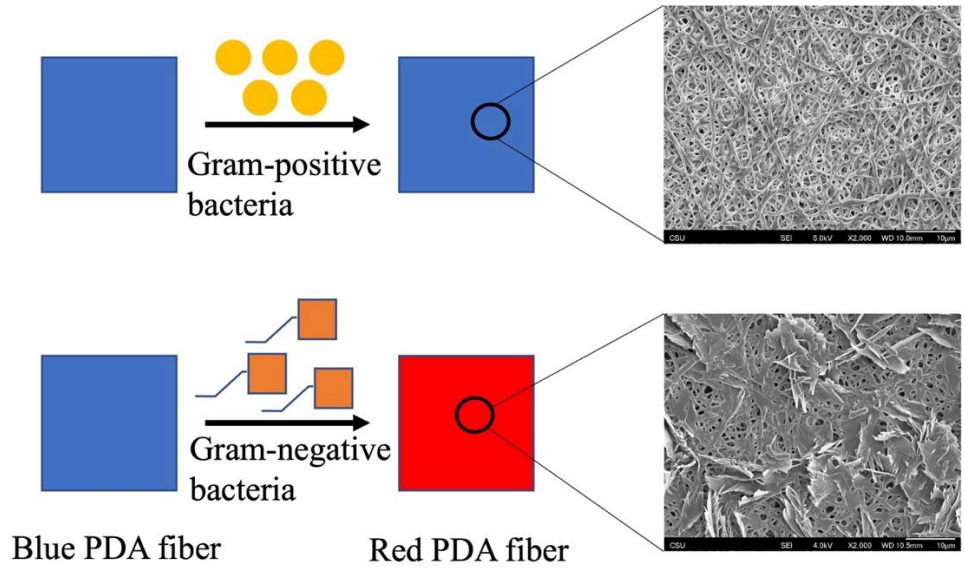

Figure 5.1. Graphical abstract.

Communicable diseases such as bacterial infection are one of the leading causes of deaths around the world [2]. In low-income countries, the probability of human death is even higher due to the communicable diseases [2]. Communicable diseases are also the leading cause of newborn mortality. According to a report published by WHO, the leading causes of death for children under 5 are pneumonia, diarrhea, and malaria that are mostly caused by bacterial infection [3]. Furthermore, with the emergence of new drug-resistant bacterial strains, human mortality due to the resistant bacterial strains is projected to increase significantly. For example, extended-spectrum beta lactamase (ESBL) producing *Escherichia coli* (*E. coli*) bacteria are reported to be often

resistant toward all orally administered antibiotics [4]. Rapid and selective bacteria detection can help in mitigating this enormous burden of bacterial infection on human health.

Bacteria can be classified into different categories. One popular system is based on the Gram staining technique developed by the Danish bacteriologist Hans Christian Gram in 1882 [5]. In this classification system, the bacteria can be grouped in two categories: Gram-negative and Gram-positive. Gram-positive bacteria have a thick outer layer mainly composed of peptidoglycan that retains the primary violet stain and exhibits a purple color during Gram staining technique [6]. Gram-negative bacteria do not have a thick peptidoglycan layer and do not retain the primary violet stain, instead retain the counter red stain, and exhibit red or pink color in the Gram staining technique [6]. A common model Gram-negative bacteria is *Escherichia coli* (*E. coli*), which can be found in human guts and are generally beneficial for keeping the gut healthy. However, several strains of *E. coli* can produce toxins that are detrimental for human health. A common model Gram-positive bacterium is *Staphylococcus aureus* (*S. aureus*), which is also hosted by human, especially in the upper respiratory track and skin. This bacterium is also a leading cause of human death due to different pathogenic strains. While comparing white blood cell count, C-reactive protein (CRP), interleukin (IL)-6 blood level, and clinical course of routine ICU patients with bacteremia, Abe and co-workers found that the Gram-negative bacteria induced a higher inflammatory response in the patients than the Gram-positive bacteria [7]. According to the antibiotic resistant priority pathogen list published by the World Health Organization (WHO) in 2017, majority of the pathogens of concerns are Gram-negative bacteria [8]. Therefore, quick and efficient detection of Gram-negative bacteria without laboratory pathological testing can be critically beneficial in healthcare practices.

Conventional bacteria detection technique includes a plate colony counting method, which is time consuming, requires highly trained personnel and are economically not viable for mass screening during an epidemic [9-10]. Recent bacteria detection techniques utilize polymerase chain reaction (PCR), enzyme-linked immunosorbent assays (ELISA), mass spectroscopy, and flow cytometry, which are highly sensitive but possess various shortcomings such as high cost, long output time, and difficulties for use in resource-limited settings [11]. The use of nanotechnology can offer tremendous advantages in bacteria detection and can help in overcoming the existing drawbacks. Due to the emergence of drug-resistant bacterial strains, it is imperative to prepare effective bacteria detection methods that can provide a selective detection for a specific bacterial strain. Rapid identification is also necessary along with selectivity because conventional bacteria detection technologies take long output time to selectively detect a specific bacteria strain [9, 10, 12]. Some novel sensors have been reported to offer selective bacteria detection, such as polypyrrole (OPPy) film [10, 13], modified gold electrodes with active layers of graphene oxide/polyethylenimine [12], dielectrophoretic impedance measurement [14], magnetic nanoparticle with TiO_2 coating and a target aptamer [15]. Recently, a nanofiber-based biosensor made by polydiacetylene (PDA) was reported to provide rapid and efficient colorimetric detection to bacteria due to high surface area of the nanofibers as well as high molecular orientation of the electrospun fibers [16-22]. Valdez et al. and Vidal et al. utilized Forcespinning® technique to prepare PDA-based nanofibers that could detect bacteria and food spoilage via a chromatic change in the fibers [23-24]. Flexible nanofiber-based biosensors prepared by electrospinning were also reported to rapidly detect *E. coli* via colorimetric indications [16, 19]. The colorimetric biosensors were fabricated using polydiacetylene (PDA) incorporated with a supporting matrix polymer such as polyurethane (PU) via an electrospinning method. PDA is gaining popularity in biosensing

applications due to its vivid colorimetric properties and has been utilized in developing sensors for heat change [25], pH change [19], bacteria contamination [16, 17, 19], and viral proteins [26]. The sensitivity of the PDA nanofiber composites had been studied, suggesting a rapid colorimetric change (from blue to red) with a short responding time of 3 min [16]. However, previous work was primarily focused on detection sensitivity to a specific bacteria type, but not for a selective detection by comparing with different bacterial strains or types. Although PDA-based nanofibers have been reported to detect bacteria [16, 19, 24], the selectivity of the PDA nanofiber-based biosensors in detecting a specific bacteria group has not been fully evaluated. Although the PDA fibers were reported to be superhydrophobic [27] due to the presence of PU, it was still unknown the interaction of bacteria and PDA fibers as well as the impact of the interaction on bacterial adhesion and bacterial morphology when colorimetric detection occurred. In addition, it is important to understand whether the interaction between the PDA nanofibers and bacteria would inhibit bacterial growth, which is of great interest for medical textiles and biomedical engineering applications.

In this report, selective detection of Gram-negative bacteria by the PDA fiber was first assessed. PU-PDA nanofiber composites were prepared via electrospinning and photopolymerization techniques. Colorimetric responses of the PU-PDA nanofibers were studied with Gram-negative and Gram-positive bacteria strains. Rapid colorimetric change from blue to red was found in the PDA fibers when tested with Gram-negative strains *E. coli* and *Pseudomonas aeruginosa* (*P. aeruginosa*), while no colorimetric change was observed in the PDA fibers when tested with Gram-positive strain *Staphylococcus aureus* (*S. aureus*). The results suggested that the PDA nanofiber composites offered a selective detection of Gram-negative bacteria over Gram-positive bacteria. Contact angle measurements indicated the PDA nanofiber composites were

hydrophobic, which allowed negligible bacteria adhesion and proliferation on nanofiber surface, suggesting significant antibacterial activities which can be beneficial in biomedical, sensing, wound dressing, and hygiene industries.

5.2 Experimental section

5.2.1 Materials

10, 12-Pentacosadiynoic acid (PCDA) was purchased from GFS Organics (Columbus, OH). Matrix polymer polyurethane (PU) was purchased from the Lubrizol Corporation (Wickliffe, OH). N, N-dimethylformamide (DMF) was purchased from Fisher Scientific (Waltham, MA). *Escherichia coli* (*E. coli*, ATCC 25,922) and *Staphylococcus aureus* (*S. aureus*, ATCC6538) pellets were purchased from ATCC (Manassas, VA). *Pseudomonas aeruginosa* (*P. aeruginosa*, P01) was obtained from agar plate culture.

5.2.2 PU-PDA nanofiber preparation

PU-PDA nanofibers were prepared via a method adapted from the report published by Bhattacharjee et al. [16]. Briefly, a 16% (w/v) solution was prepared by mixing the required amount of PU chips and PCDA powders (2:1 by weight) in DMF. The solution was mixed by a rigorous stirring on a hot-plate stirrer at 55 ºC for 24 h, resulting in a homogenously pink mixture after 24 h. The solution was then used to prepare nanofibers using an electrospinning method. The electrospinning was conducted at an injection rate of 0.12 mL/hour, a voltage of 20 kV, a collecting distance of 17 cm, and a collecting time of 1 h, resulting in white PU-PCDA nanofiber mats. Then, each nanofiber mat sample was photopolymerized using UV light (Spectroline, LONGLIFE filter, New York, USA) at 254 nm for 3 min. The fibers became blue after the photopolymerization

because the PCDA monomers were polymerized, resulting in the macromolecules of PDAs mixed in the nanofiber matrix of PU. The PU-PDA nanofiber mats were stored in the dark to avoid additional changes due to light.

5.2.3 Fiber characterization

The morphology of the fibers was investigated using a JEOL JSM-6500 field emission scanning electron microscope (SEM) at 3 kV. To improve conductivity, the fibers were gold coated (10 nm) using a Denton Vacuum-DESK 2 Sputter Coater. Average diameter of the fibers was calculated based on the SEM images using ImageJ software. In addition, contact angle measurements were made to evaluate hydrophilicity/hydrophobicity of the fiber mats using a Ramé-Hart goniometer.

5.2.4 Bacteria culture

Two culture media were used to prepare bacteria culture solutions, Luria Bertani (LB) broth and beef extract-peptone-based nutrient media. The beef extract-peptone-based media recipe was derived from the AATCC (American Association of Textile Chemists and Colorists) method 147, and the media was denoted as AM media henceforth. AM media was prepared by mixing 3 g beef extract, 5 g peptone, and 8 g NaCl in 1L distilled water, followed by sterilization at 121 ºC temperature and 23 PSI pressure. To prepare LB broth, 5 g yeast extract, 10 g NaCl, and 10 g tryptone were dissolved in 1L distilled water, followed by sterilization at 121 ºC temperature and 23 PSI pressure. *E. coli* and *S. aureus* pellets were added to the hydration fluid provided by the manufacturer. 2 mL bacteria–hydration fluid mixture was mixed in 500 mL LB media and cultured for 24 h at 37 ºC in a stationary incubator. Then, the cultured solution was used to inoculate an

agar plate for 24 h at 37 ºC in a stationary incubator. One colony extracted from the agar plate was used to culture bacteria in both AM and LB media. The bacteria were cultured until a 10^9 colony-forming unit (CFU)/mL of bacteria concentration was obtained after 48 h of incubation at 37 ºC. Following notations are used henceforth for clarity: *E. coli* cultured in LB broth—EC-LB; *E. coli* cultured in AM media—EC-AM; *S. aureus* cultured in LB—SA-LB; and *S. aureus* cultured in AM—SA-AM. For *P. aeruginosa*, one colony was inoculated from the agar plate and cultured for 48 h in the AM media at 37 ºC inside a stationary incubator. Bacteria concentrations were determined by serial dilution and plating technique.

5.2.5 Colorimetric responses of PU-PDA fibers

Gram-negative *E. coli* and Gram-positive *S. aureus* cultures of 10^9 CFU/mL concentrations were used to investigate colorimetric responses of PU-PDA fibers. 2 inch X 2 inch PU-PDA fiber mats were cut and put in sterile petri dishes where 25 mL *E. coli* or *S. aureus* bacteria cultures were added to the petri dishes. Colorimetric responses of the fibers were recorded by taking photographs from time = 0 min and then every 30 min for 3 h. To quantify the color changes in the PDA fibers when incubated with bacteria cultures, absorbance spectra of the fiber mats were collected by a ColorQuest spectrophotometer. The absorbance spectra for the fibers were collected every 30 min from 0 to 3 h of incubation followed by an additional spectrum after 24 h incubation. For Gram-negative *P. aeruginosa* culture, only photographs were taken to verify colorimetric responses of the fibers. In the spectrophotometer measurements, colorimetric responses (CR%) were quantitatively measured using the protocol described by Yapor et al. [19].

5.2.6 Bacteria morphology and biofilm formation on PDA fibers

Scanning electron microscope (SEM) was used to study the bacteria morphology and biofilm formation on the PDA fiber surfaces. *E. coli* and *S. aureus* were cultured in AM media. Three circular PDA fiber mats with 2 mm diameter were cut and kept inside a 24-well plate. Aluminum foil (AL) and polystyrene (PS) samples were used as control samples in the well plate. The samples were first incubated with diluted *E. coli* and *S. aureus* culture (10^7 CFU/mL) for 6 h and 24 h, respectively. After incubation with bacteria, the samples were incubated for 45 min in a fixative solution containing 3% glutaraldehyde, 0.1 M sucrose, and 0.1 M sodium cacodylate in DI water. Then, the samples were incubated for 10 min in a buffer solution, which was the fixative solution without the glutaraldehyde. After that, the samples were dehydrated using 35%, 50%, and 70% ethanol solution for 10 min, respectively. Before SEM imaging, the samples were gold coated before SEM images were taken. Two repeated experiments were conducted for each strain of bacteria.

5.2.7 Bacteria adhesion on PDA fibers

Fluorescent microscopic images were taken to understand the bacteria adhesion on PDA fibers. *E. coli* and *S. aureus* were only cultured in AM media. 3 circular PDA fibers with 2 mm diameter were put in a 24- well plate. AL and PS samples were also used as controls in the plate. The samples were first incubated with diluted *E. coli* and *S. aureus* culture (10^7 CFU/mL) for 6 h and 24 h, respectively. After the incubation, the bacteria solution was aspirated from the well plates and the samples were rinsed with PBS for 3 times to remove any non-adhered bacteria. The samples were incubated for 15 min at room temperature in dark with a stain solution containing 3μL/mL propidium iodide and Syto 9 stains (1:1) in PBS. After the incubation with the stain

solution, the samples were rinsed and incubated with 3.7% formaldehyde solution for 15 min. Lastly, the samples were washed with PBS for 3 times and immediately imaged using a fluorescent microscope. Two repeated experiments were conducted for each strain of bacteria.

5.3 Results and discussion

5.3.1 PU-PDA nanofiber characterization

White PU-PDA fiber mats were prepared via electrospinning and photopolymerization techniques. After the photopolymerization, the white fiber mats became blue, suggesting successful photopolymerization of PCDAs into PDAs [28]. **Figure 5.2** shows SEM images of blue PU-PDA fibers. The fibers had scale-like surfaces with an average diameter of 550 ± 125 nm that was in good agreement with the diameter range of the fiber reported previously [16, 19]. The contact angle measurements of the fiber mats showed that the fiber mats had an average contact angle of 144º ± 3º which suggested superhydrophobic nature of the fibers (**Figure 5.2**).

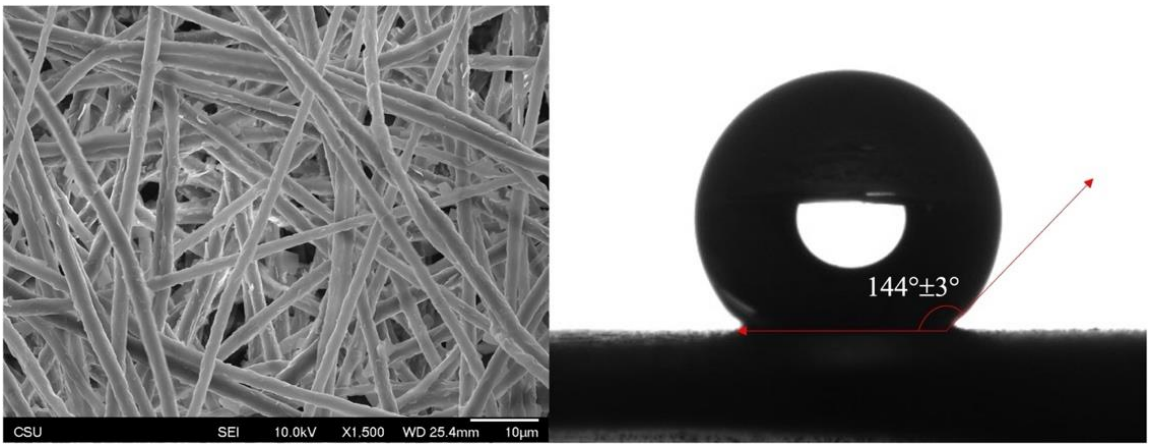

Figure 5.2. A SEM image of PU-PDA fibers. A water drop image is shown in inset for contact angle measurements.

5.3.2 Colorimetric behaviors of PDA fibers

Two culture media were used in bacteria culture—LB broth and AM media, to study the colorimetric responses of PU-PDA fibers to bacterial detection. The reasoning behind choosing two media was to examine if bacterial detection offered by the fibers was dependent on changes in bacteria culture. When a bacteria solution of 10^9 CFU/mL was poured into a petri dish containing a PU-PDA fiber mat, colorimetric responses were documented. **Figure 5.3** shows the photographs of the fibers that were immersed in bacteria cultures and control solutions before and after 24 h incubation. When the Gram-negative *E. coli* cultures (EC-LB and EC-AM) were introduced to the PDA fibers, the color of the fibers started turning into red immediately. At the beginning, the color changes started from the edge of the fiber mat and then the full fiber mat gradually changed from blue to red. The fibers were also tested with culture media only solutions (LB and AM), and no color changes were observed. Therefore, the colorimetric responses were primarily due to the interaction between the Gram-negative bacteria and the PU-PDA fibers. In addition, because the color changes of the PU-PDA fibers were found in both the EC-LB and EC-AM cultures, it indicated that the color-changing characteristics of the fibers were independent on culture media.

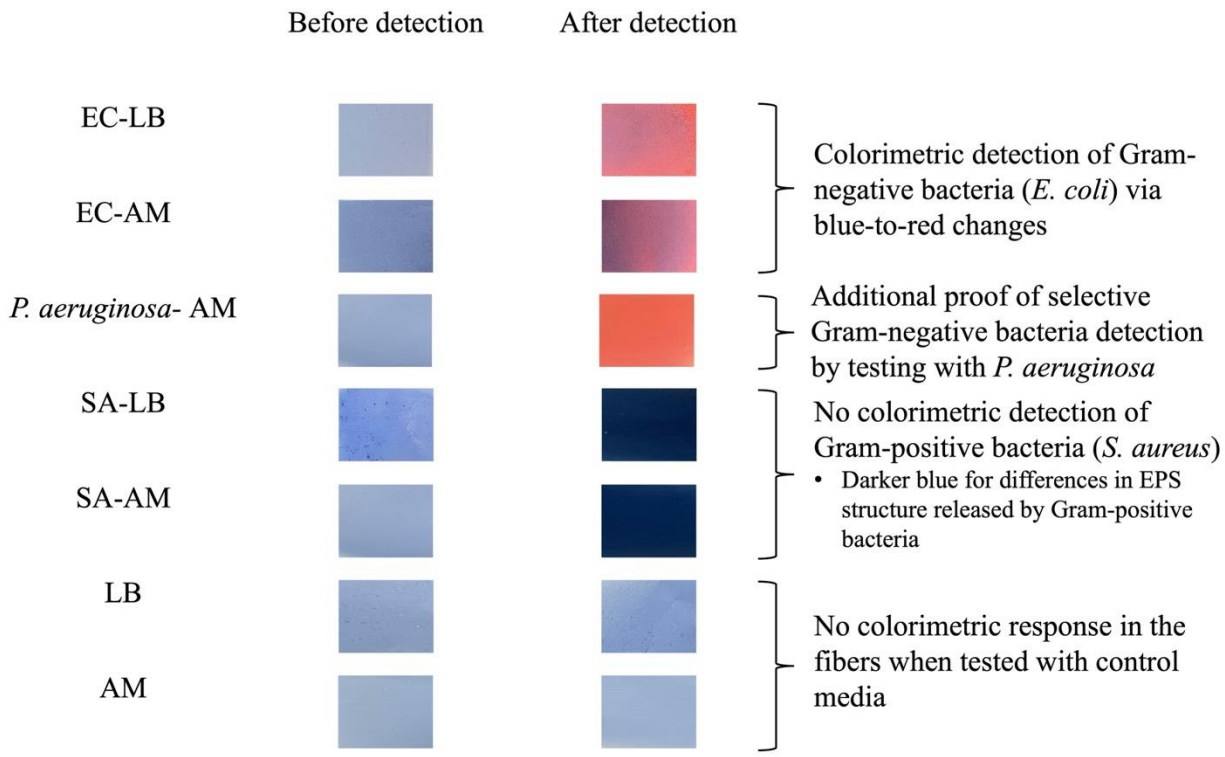

Figure 5.3. Colorimetric behaviors of PDA fibers interacting with different bacteria and control solutions.

On the other hand, *S. aureus*, the Gram-positive bacteria, cultured in both LB and AM was tested by interacting with PU-PDA fibers. No color change was observed in the PDA fibers (**Figure 5.3**). The light blue fibers seemed to turn darker after 24 h incubation, but no blue-to-red changes were found throughout the testing time (24 h). There are structural differences between Gram-positive and Gram-negative bacteria due to the presence of a thick peptidoglycan layer on Gram-positive bacteria. Additionally, the extracellular polymeric substances (EPS) released by the Gram-positive bacteria can differ from those released by the Gram-negative. The dark blue color on the PDA fibers when tested with Gram-positive *S. aureus* was different than Gram-negative *E. coli* and the control samples, which might suggest the differences in EPS environment. Future investigations can be focused on the EPS contents released by different bacteria and hence further

understand the correlation of colorimetric changes and chemical changes in the PDA fibers due to the interactions between the PDA and bacteria.

In addition, another Gram-negative bacteria *P. aeruginosa* was cultured in AM media for 48 h. When PU-PDA fibers were immersed in the *P. aeruginosa* solution, a vivid red was quickly observed in the fibers that were blue. The colorimetric responses strongly confirmed that the PDA fibers were able to selectively detect Gram-negative bacteria over Gram-positive bacteria via blue-to-red colorimetric responses.

5.3.3 Quantitative analysis of color change in the fiber

Two representative absorbance spectra are shown in **Figure 5.4** for the PU-PDA fiber mats immersed in Gram-negative *E. coli* and in Gram-positive *S. aureus*, respectively. The absorbance spectra for all the samples shown in **Figure 5.4** can be found in Supplementary Document. Blue PDA fibers showed a distinct absorbance spectrum where a prominent peak at 650 nm was found. When the color of the PDA fibers changed to red when the fibers were interacting with *E. coli*, the peak at 650 nm shifts to 550 nm on the absorbance spectra [19]. The peak shift occurred to the fibers interacting with *E. coli* in both media. However, no such peak shift was found in the fibers interacting with *S. aureus* cultures. The spectra showed that 650 nm peak remained for the entire testing period, which is in good agreement with the color-changing behaviors observed in the photographic images.

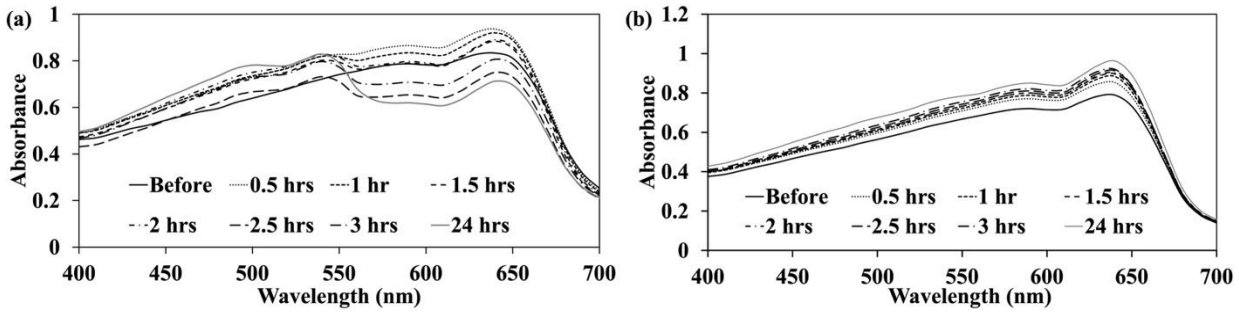

Figure 5.4. Absorbance spectra of PDA fibers when incubated with (a) EC-AM and (b) SA-AM.

Colorimetric response percentage (CR %) calculated using the method described by [19] is shown in **Figure 5.5**. A CR% of 14–18% was found in the fibers tested with EC-LB and EC-AM after 24 h incubation, whereas there was no significant CR % between the SA-LB and SA-AM cultures. The CR % for the EC-AM sample was higher initially than that for the EC-LB samples; however, after the 24 h incubation, the EC-LB sample showed higher CR %. Bacteria produces biofilms during growth which is composed of bacteria cells and extracellular polymeric substances (EPS). A previous study reported that the EPS from Gram-negative *E. coli* played an important role in colorimetric changes of PDA fibers [16]. The initial CR% difference between EC-LB and EC-AM was likely due to the different composition of the EPS released by the Gram-negative *E. coli*. A hypothesis is that EC-AM culture produced more EPS than EC-LB culture and hence resulted in a fast color change of PDA fibers in EC-AM culture. The quantity of EPS production by Gram-negative *E. coli* when cultured in various nutritious media can be investigated further to understand the differences in colorimetric responses of the PDA fibers.

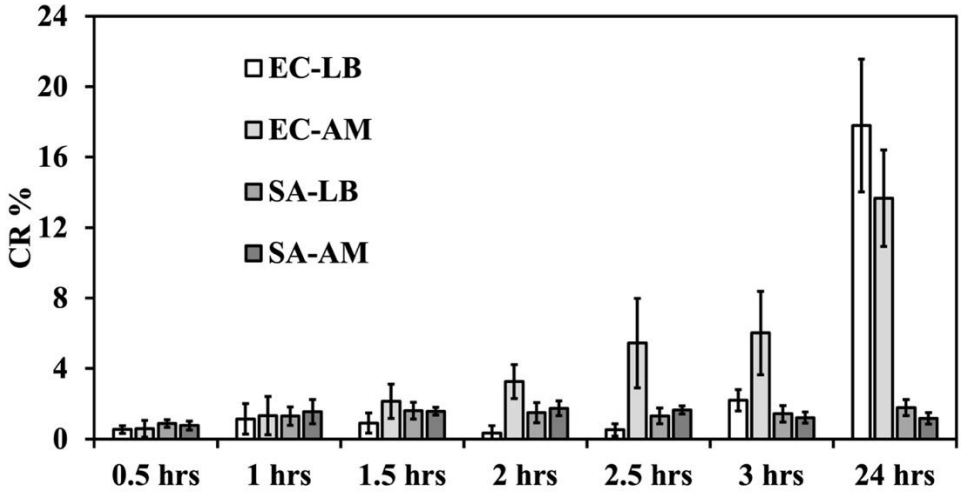

Figure 5.5. CR% of PDA fibers after incubation with bacteria cultures.

Another hypothesis is due to the different thickness of the outer layer mostly comprised of lipopolysaccharides (LPS) of bacteria. Generally, Gram-negative bacteria such as *E. coli* have a thin outer layer, while Gram-positive bacteria such as *S. aureus* have a thick outer layer [29]. When bacteria start stationary or death phase during growth period, they shed this LPS layer with other secreted proteins in the surrounding environment. When the PU-PDA fibers were incubated with the bacteria culture for 24 h at room temperature, the bacteria started their stationery and death phase due to no additional nutrient. The bacteria likely started shedding the LPS layer, which changed the color of the fiber gradually. The hypothesis aligned with the CR% result presented in **Figure 5.4**. To induce a significant color change in the fiber, the *E. coli* culture needed responding time which was about 30 min to 1 h. In addition, the death phase started faster for *E. coli* in AM media than in LB media because AM media had lower nutrients than LB media. As a result, a faster color change was observed in AM media than in LB media, as shown in **Figure 5.4**. On the other hand, no colorimetric responses in the fibers were found for Gram-positive bacteria during testing because the Gram-positive bacteria do not possess an LPS layer and hence no such interaction between the PDA fiber and LPS occurred. Moreover, Gram-positive bacteria has thick

outer layer composed of peptidoglycan. Therefore, the selective detection of Gram-negative bacteria was likely due to the structural differences between the two different categories of bacteria.

5.3.4 Bacteria morphology on PDA fibers

To further understand the interaction between bacteria and the fibers, SEM images were taken after 6 h and 24 h incubation to study the morphologies of bacteria on the PDA fiber mats. To simplify the experiment, only AM media were used to culture bacteria. Polystyrene (PS) and aluminum foils (AL) were used as control surfaces to study bacteria morphology. The results for *E. coli* incubation are presented in **Figure 5.6**. At 6 h incubation, PS had the highest coverage of *E. coli* on the surface. AL had the less coverage of *E. coli* compared to PS. At 24 h incubation, the number of *E. coli* covering on the PS surface increased exponentially, while no significant increase in *E. coli* coverage was found on the AL surface. It was reported that AL was slightly antibacterial in nature [30] and hence bacteria were prevented from continuous growth on the AL surface. In comparison, the PDA fibers had lower number of *E. coli* covering the fiber surface than the PS and AL surfaces. At 6 h incubation, some *E. coli* was found to be attached to the fiber surface, mostly in the pores of the fiber mat where no significant morphological changes were found in the fibers. However, significant morphological changes were observed on the fiber surfaces after 24 h of incubation likely due to the interaction between the *E. coli* and the fibers. Previous works showed that the extracellular polymeric substances (EPS) of *E. coli* could induce a color change in PDA fibers [16]. As previously discussed, Gram-negative bacteria can shed their outer LPS layer in the surrounding environment. The EPS and LPS that were secreted from the *E. coli* might interact with the fibers and were able to alter the fiber morphology, which was visibly unfolded via colorimetric

responses from blue to red. The amount of the EPS and LPS released from *E. coli* was time dependent. Therefore, more significant morphological changes were found on the fiber surfaces after 24 h incubation than 6 h incubation. In addition, previous reports suggested the colorimetric changes in PDA are due to a configuration change occurring in the PDA macromolecules, which might subsequently change the morphology of the PU-PDA fibers [16, 19, 25].

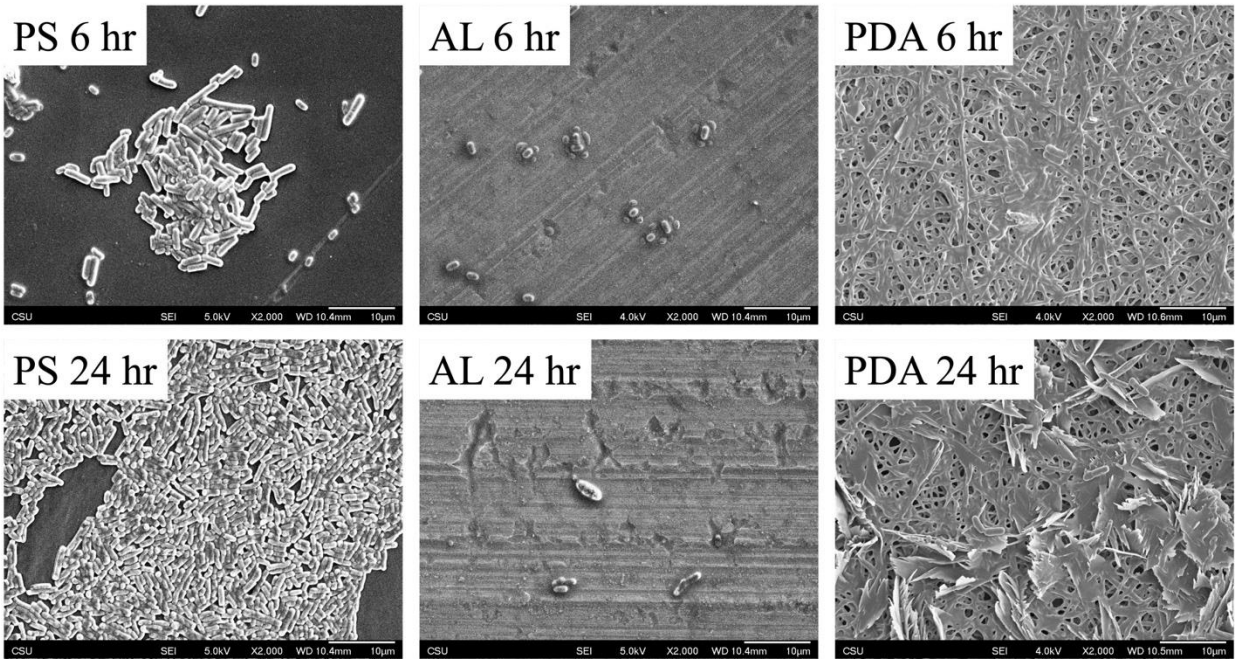

Figure 5.6. SEM images of *E. coli* coverage on aluminum foil (AL), polystyrene (PS), and PDA fibers.

The Gram-positive *S. aureus* morphologies on PS, AL, and PDA fiber surfaces are presented in **Figure 5.7**. PS was also found to be covered with the most *S. aureus* which was like *E. coli*. There were very few *S. aureus* attached to the AL surface after 6 h incubation. However, the coverage was significantly increased after 24 h incubation. Compared to the PS and AL, the PDA fiber had lower number of *S. aureus* attached to the surface. At the 6 h incubation, nearly no bacteria were found on the PDA fiber surface, which signified no color change observed in the fiber mat. After 24 h incubation, some *S. aureus* was found on the fiber surface but in a sporadic

manner. In comparison with *E. coli*, *S. aureus* was not able to change the fiber morphology after 24 h incubation. It was most likely because *S. aureus* did not secrete LPS or other proteins in the bacterial EPS system that can react with the PDAs in the fiber and induce a color change.

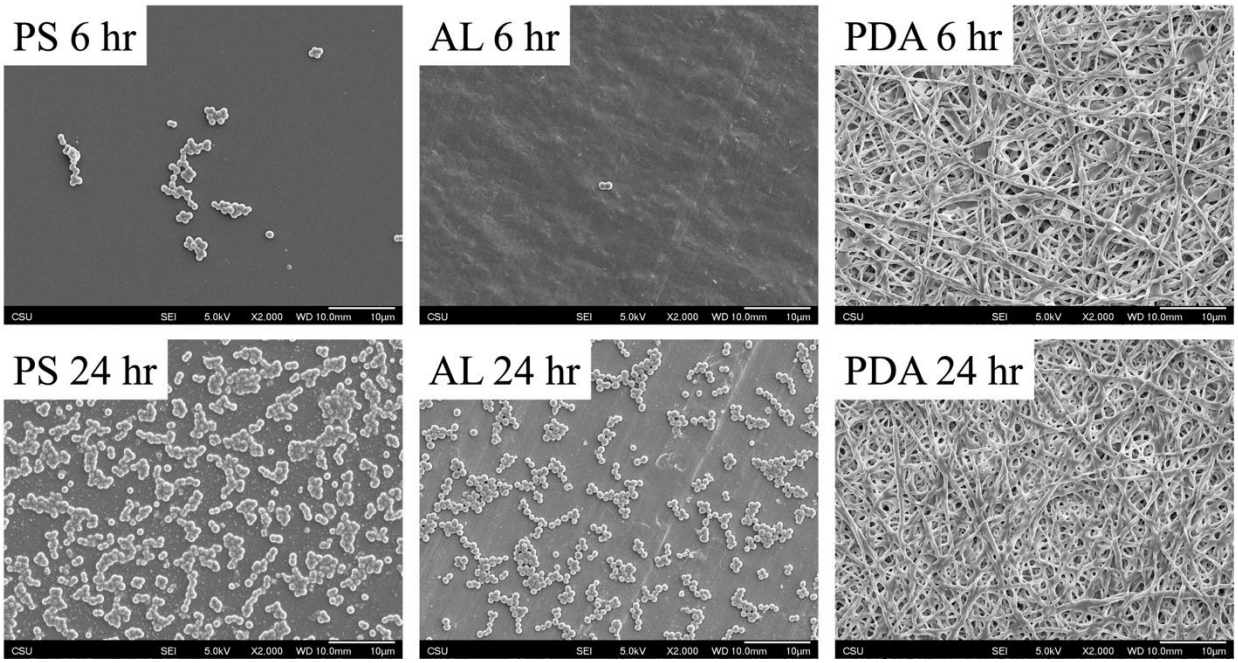

Figure 5.7. SEM images of *S. aureus* morphology on PDA fiber, aluminum foil, and polystyrene samples.

5.3.5 Bacteria adhesion on PDA surface

Quantitative analysis was also conducted to study bacteria attachment on PDA fibers as well as AL and PS surfaces. To understand if bacteria proliferated or died on the surfaces, a live/dead bacterium staining technique was used for this experiment. **Figure 5.8** shows the number of live/dead *E. coli* on the material surfaces where green color represents live bacteria and red indicates dead bacteria, respectively. Some colonies were yellow, indicating overlapping of both live and dead bacteria. Both PS and AL had significantly high numbers of live *E. coli* on the surface after 6 h of incubation. Although PS had low live *E. coli* at 6 h incubation, the number was increased significantly after 24 h incubation. PDA fibers had few live *E. coli* on surface at 6 h

incubation, but the number was even slightly reduced after 24 h incubation. Previous contact angle measurements suggested that the PU-PDA fiber is superhydrophobic, which prevented *E. coli* from growing on the fibers. In addition, the PDA fiber had the highest number of dead *E. coli* on fiber surface at 6 h incubation. After 24 h incubation, the number of dead *E. coli* on the PDA fiber surface was negligible compared to that on PS and AL surfaces. The results suggest that the PU-PDA fibers had excellent antibacterial properties.

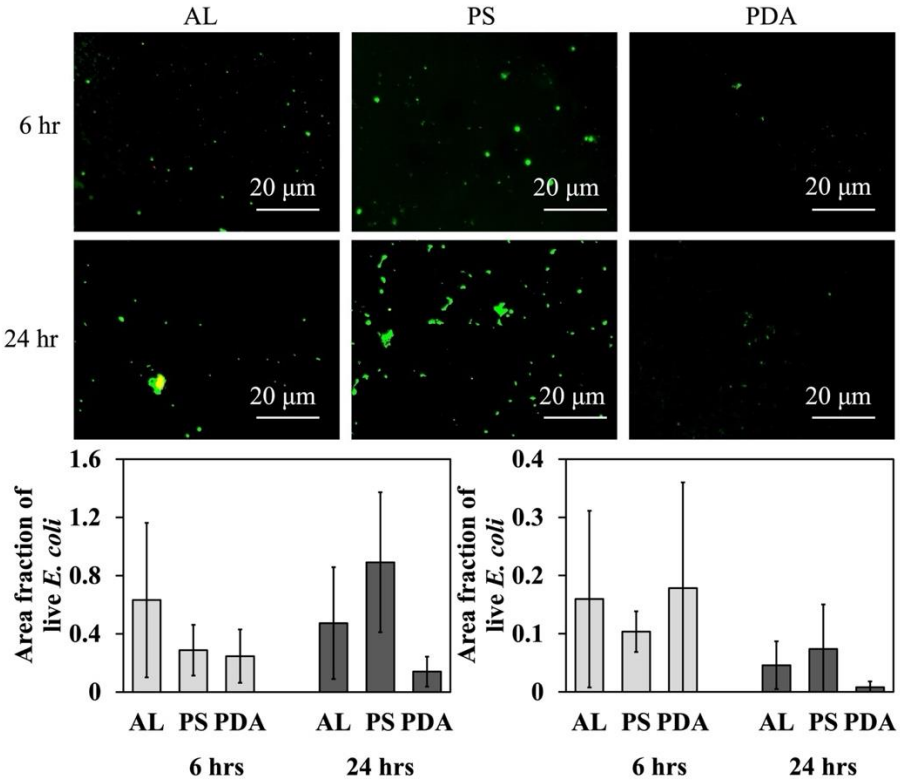

Figure 5.8. Fluorescent microscopic images of PDA fibers, aluminum foil, and polystyrene samples after incubating with *E. coli*, where green denotes live and red denotes dead bacteria. Area fractions of dead and live *E. coli* are presented in the bottom plots.

Similar results of antibacterial behaviors were found in PU-PDA fibers when the samples were incubated with Gram-positive *S. aureus* (**Figure 5.9**). PS had the most live *S. aureus* attached to the surface at both 6 h and 24 h incubation. There were a high number of dead *S. aureus* on the AL surface after 24 h incubation, indicating slight antibacterial properties of the AL foil [30]. The

number of both live and dead *S. aureus* on the PDA fiber surface was negligible, suggesting antibacterial properties against Gram-positive bacteria.

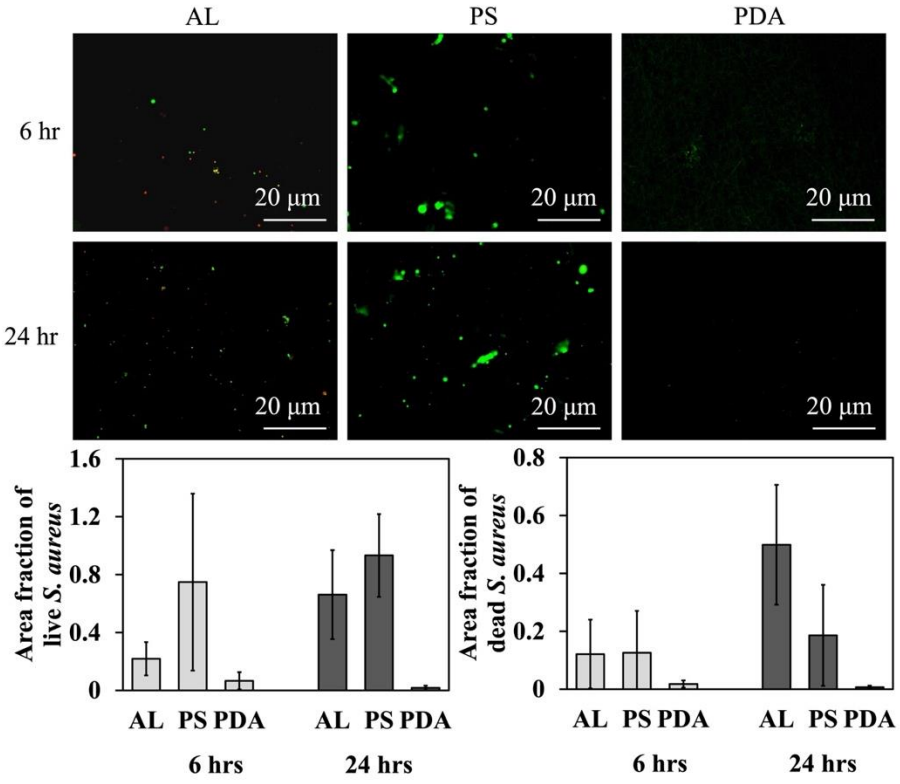

Figure 5.9. Fluorescent microscopic images of PDA fibers, aluminum foil, and polystyrene samples after incubating with *S. aureus*, where green denotes live and red denotes dead bacteria. Area fractions of dead and live *E. coli* are presented in the bottom plots.

In a summary, the staining technique provided both qualitative and quantitative analysis of the bacteria adhesion and antibacterial properties of PDA fibers. The PDA fiber mats had porous surfaces, and hence, a small number of bacteria might be first trapped in the pores. The trapped bacteria were not able to continuously grow in the pores, suggesting that the PDA fibers had excellent antibacterial properties.

5.4 Conclusions

In this study, a colorimetric biosensing platform was prepared to selectively detect Gram-negative bacteria. The biosensor was prepared by electrospun PDA nanofiber which was flexible and vividly blue after photopolymerization via UV light. The blue fibers changed to bright red when Gram-negative *E. coli* and *P. aeruginosa* strains were used for testing selective detection by the PDA fibers. In comparison, no blue-to-red responses were observed in the PDA nanofibers when Gram-positive strain *S. aureus* was tested. The quantification of color changes by using a spectrophotometer bolstered that the PDA nanofiber biosensor was able to selectively detect Gram-negative bacteria via a blue-to-red color transition. The selective detection was most likely due to structural differences between Gram-positive bacteria and Gram-negative bacteria as well as different EPS released by different bacteria. Additionally, the adhesion and morphology of the bacteria on the PDA nanofiber surface were evaluated by bacteria staining and microscopic image analysis. It was found that the PDA fibers were significantly antibacterial compared to the control AL and PS surfaces. The results suggested that the PDA nanofibers have great potential in developing smart medical textiles offering both selective detection of bacteria and antibacterial properties simultaneously.

REFERENCES

1. Bhattacharjee, A., Goodall, E., Popat, K. C., Zou, L., & Li, Y. V. (2023). Selective detection of Gram-negative bacteria and antibacterial properties of colorimetric polydiacetylene nanofibers. *Journal of Materials Science*, 1-13. https://doi.org/10.1007/s10853-023-08550-z
2. The top 10 causes of death. Geneva: WHO. 2022. https://www.who.int/news-room/fact-sheets/detail/the-top-10-causes-of-death
3. Newborn mortality. Geneva: WHO. 2022. https://www.who.int/news-room/fact-sheets/detail/levels-and-trends-in-child-mortality-report-2021
4. Infectious Diseases Society of America (IDSA) (2011) Combating antimicrobial resistance: Policy recommendations to save lives, clinical infectious diseases. Clin. Infect. Dis. 52(5): S397–S428.
5. Bartholomew JW, Mittwer T (1952) The Gram stain. Bacteriol Rev. 16(1): 1-29.
6. Smith AC, Hussey MA (2005) Gram stain protocols. American Society for Microbiology 1:14.
7. Abe R, Oda S, Sadahiro T, Nakamura M, Hirayama Y, Tateishi Y, Shinozaki K, Hirasawa H (2010) Gram-negative bacteremia induces greater magnitude of inflammatory response than Gram-positive bacteremia. Crit. Care 14: R27.
8. Breijyeh Z, Jubeh B, Karaman R (2020) Resistance of Gram-negative bacteria to current antibacterial agents and approaches to resolve it. Molecules 26(6): 1340.
9. Singh A, Arya S, Glass N, Hanifi-Moghaddam P, Naidoo R, Szymanski CM, Tanha J, Evoy S (2010) Bacteriophage tailspike proteins as molecular probes for sensitive and selective bacterial detection. Biosens. Bioelectron. 26(1): 131-138.

10. Tokonami S, Nakadoi Y, Takahashi M, Ikemizu M, Kadoma T, Saimatsu K, Dung LQ, Shiigi H, Nagaoka T (2013) Label-free and selective bacteria detection using a film with transferred bacterial configuration. Anal. Chem. 85(10): 4925–4929.
11. Zhu H, Sikora U, Ozcan A (2012) Quantum dot enabled detection of *Escherichia coli* using a cell-phone. Analyst 137: 2541-2544.
12. Jijie R, Kahlouche K, Barras A, Yamakawa N, Bouckaert J, Gharbi T, Szunerits S, Boukherroub R (2018) Reduced graphene oxide/polyethylenimine based immunosensor for the selective and sensitive electrochemical detection of uropathogenic *Escherichia coli*. Sensor Actuat. B-Chem. 260: 255-263.
13. Wu J, Wang R, Lu Y, Jia M, Yan J, Bian X (2019) Facile preparation of a bacteria imprinted artificial receptor for highly selective bacterial recognition and label-free impedimetric detection Anal. Chem. 91(1): 1027-1033.
14. Suehiro J, Hamada R, Noutomi D, Shutou M, Hara M (2003) Selective detection of viable bacteria using dielectrophoretic impedance measurement method. J. Electrostat. 57(2): 157-168.
15. Shen H, Wang J, Liu H, Li Z, Jiang F, Wang FB, Yuan Q (2016) Rapid and selective detection of pathogenic bacteria in bloodstream infections with aptamer-based recognition. ACS Appl. Mater. Interfaces 8(30): 19371–19378.
16. Bhattacharjee A, Clark R, Gentry-Weeks C, Li YV (2020) A novel receptor-free polydiacetylene nanofiber biosensor for detecting *E. coli* via colorimetric changes. Materials Advances 1:3387-3397.
17. Bhattacharjee A, Clark R, Gentry-Weeks C, Li YV (2020) Study of bacterial components activating a colorimetric transition in bacteria-detecting nanofiber wound dressing

applications. International Textile and Apparel Association Annual Conference Proceedings, 77(1).

18. Currie S, Shariatzadeh F, Singh H, Logsetty S, Liu S (2020) Highly sensitive bacteria-responsive membranes consisting of core–shell polyurethane polyvinylpyrrolidone electrospun nanofibers for in situ detection of bacterial infections. ACS Appl. Mater. Interfaces 12(41): 45859–45872.
19. Yapor JP, Alharby A, Gentry-Weeks C, Reynolds MM, Alam A, Li YV (2017) Polydiacetylene nanofiber composites as a colorimetric sensor responding to *Escherichia coli* and pH. ACS Omega 2(10): 7334-7342.
20. Luo Y, Nartker S, Wiederoder M, Miller H, Hochhalter D, Drzal L, Alocilja E (2012) Novel biosensor based on electrospun nanofiber and magnetic nanoparticles for the detection of *E. coli* O157:H7. IEEE T Nanotechnol 11(4): 676-681.
21. Song J, Lin X, Ee LY, Li SFY, Huang M (2022) A review on electrospinning as versatile supports for diverse nanofibers and their applications in environmental sensing. Adv. Fiber Mater 5:1-32.
22. Kang S, Zhao K, Yu D, Zheng X, Huang C (2022) Advances in biosensing and environmental monitoring based on electrospun nanofibers. Adv. Fiber Mater. 4:404-435.
23. Valdez M, Gupta SK, Lozano K, Mao Y (2019) ForceSpun polydiacetylene nanofibers as colorimetric sensor for food spoilage detection. Sensor Actuat B-Chem. 297: 126734.
24. Vidal P, Martinez M, Hernandez C, Adhikari AR, Mao Y, Materon L, Lozano K (2019) Development of chromatic biosensor for quick bacterial detection based on polyvinyl butyrate-polydiacetylene nonwoven fiber composites. Eur Polym J. 121:109284.

25. Alam A, Yapor JP, Reynolds MM, Li YV (2016) Study of polydiacetylene-poly (ethylene oxide) electrospun fibers used as biosensors. Materials 9(3):202.
26. Bhattacharjee A, Sabino RM, Gangwish J, Manivasagam VK, James S, Popat KC, Reynolds M, Li YV (2022) A novel colorimetric biosensor for detecting SARS-CoV-2 by utilizing the interaction between nucleocapsid antibody and spike proteins. In vitro models 1: 241-247.
27. Chen L, Wu F, Li Y, Wang Y, Si L, Lee KI, Fei B (2018) Robust and elastic superhydrophobic breathable fibrous membrane with *in situ* grown hierarchical structures. J. Membrane Sci. 547: 93-98.
28. Chae SK, Park H, Yoon J, Lee CH, Ahn DJ, Kim JM (2007) Polydiacetylene supramolecules in electrospun microfibers: fabrication, micropatterning, and sensor applications. Adv. Mater. 19(4): 521-524.
29. Eboigbodin K, Biggs C (2008) Characterization of the extracellular polymeric substances produced by *Escherichia coli* using infrared spectroscopic, proteomic, and aggregation studies. Biomacromolecules 9(2): 686–695.
30. Saadi N, Alotaibi K, Hassan L, Smith Q, Watanabe F, Khan AA, Karabacak T (2021) Enhancing the antibacterial efficacy of aluminum foil by nanostructuring its surface using hot water treatment. Nanotechnology 32(32): 325103.

CHAPTER 6/A NOVEL COLORIMETRIC BIOSENSOR FOR DETECTING SARS-COV-2 BY UTILIZING THE INTERACTION BETWEEN NUCLEOCAPSID ANTIBODY AND SPIKE PROTEINS[1]

6.1 Introduction

SARS-CoV-2 is a pandemic coronavirus that causes severe respiratory disease (COVID-19) in humans and is responsible for millions of deaths around the world since early 2020. The virus affects the human respiratory cells through its spike (S) proteins located at the outer shell. To monitor the rapid spreading of SARS-CoV-2 and to reduce the deaths from the COVID-19, early detection of SARS-CoV-2 is of utmost necessity. This report describes a flexible colorimetric biosensor capable of detecting the S protein of SARS-CoV-2. The colorimetric biosensor is made of polyurethane (PU) - polydiacetylene (PDA) nanofiber composite that was chemically functionalized to create a binding site for the receptor molecule – nucleocapsid antibody (anti-N) protein of SARS-CoV-2. After the anti-N protein conjugation to the functionalized PDA fibers, the PU-PDA-NHS-anti fiber was able to detect the S protein of SARS-CoV-2 at room temperature via a colorimetric transition from blue-to-red. The PU-PDA nanofiber-based biosensors are flexible and lightweight; do not require a power supply such as a battery when the colorimetric detection to S protein occurs, suggesting a sensing platform of wearable devices and personal protective equipment such as facemasks and medical gowns for real-time monitoring of virus contraction and contamination. The wearable biosensors could significantly power mass surveillance technologies to fight against the COVID-19 pandemic.

---

[1]This work was published in *in vitro Models* and is reproduced here with permission [1].

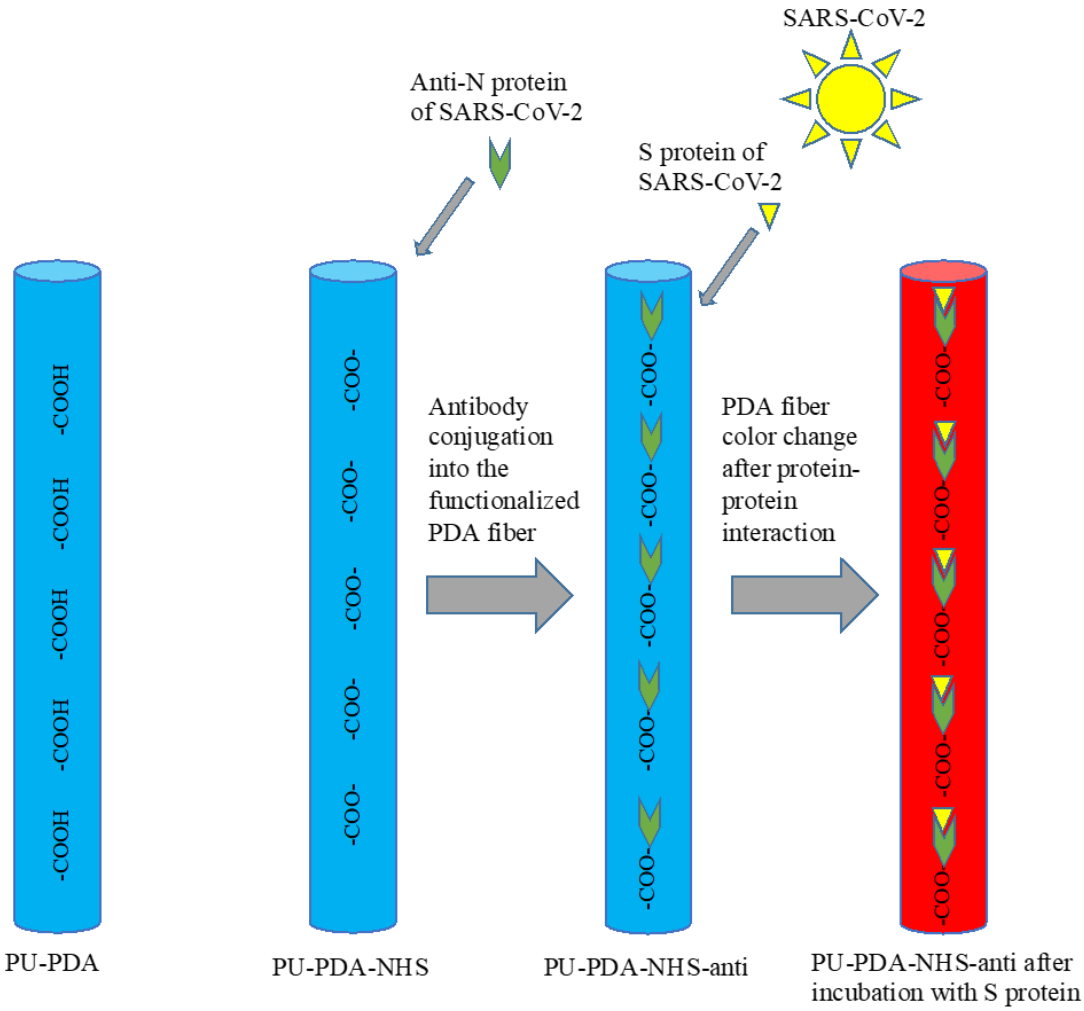

Figure 6.1. Graphical abstract.

Several coronaviruses from the family of *Coronaviridae* used to cause mild respiratory diseases until the Severe Acute Respiratory Syndrome Coronavirus (SARS-CoV) was transmitted from animal to human and caused the severe acute respiratory syndrome (SARS) disease in 2002 [2]. In December 2019, a cluster of patients with severe respiratory syndrome (pneumonia) was reported in Wuhan, China, and the associated pathogen was identified as a novel coronavirus [3], which was later named as SARS-CoV-2, and the disease was named as COVID-19. Since then, the COVID-19 cases have been reported in every continent including Antarctica. On 11 March 2020,

World Health Organization (WHO) declared the COVID-19 as a pandemic [4]. As of 15 November 2021, the total number of COVID-19 cases reported by WHO is more than 252 million with an associated death of more than 5 million individuals [5]. This novel coronavirus is the seventh edition in the *Coronaviridae* family of viruses that causes respiratory diseases in humans. The spreading capability of the new virus (SARS-CoV-2) is higher than all the other coronaviruses and new variants of SARS-CoV-2 spread even faster in humans than the original virus. SARS-CoV-2 has glycosylated spike (S) proteins [6] that binds to the Angiotensin-Converting Enzyme II (ACE2) receptor found in lower respiratory tracts of humans [7]. The virus can survive on plastic, metal, or cardboard surfaces for 4 hours up to 3 days, making it easier for the virus to spread [8]. To minimize the rapid spread of SARS-CoV-2, effective viral detection methods are necessary. The most popular method of SARS-CoV-2 detection is the real-time Reverse Transcription-Polymerase Chain Reaction (rRT-PCR). However, it has several limitations such as complex protocols, the need for trained personnel, long turnaround, and false-negative results [9]. Different detection techniques have been developed since 2019 including plasmonic-based colorimetric assays, antibody capture, and antigen-binding assays, paper-based biomolecular sensors, and thermoplasmonic chips [10]. However, there is still a need to develop effective, highly selective, and easy-to-use detection methods for SARS-CoV-2.

Recently, polymeric materials such as polydiacetylene (PDA) that have colorimetric responses to environmental stimuli have gained great interest in developing colorimetric biosensors [11-15]. Previous studies suggested that PDAs have demonstrated colorimetric transition responses to various bacteria and viruses [12, 16]. Charych et al. (1993) first reported a PDA-based sensor that could detect hemagglutinin of the influenza virus [17]. Lately, PDA-based sensors have been reported to detect influenza virus, hepatitis B, foot-and-mouth virus, bovine

viral diarrhea virus, feline calicivirus, and vaccinia virus [16, 18-19], suggesting a potential of using PDAs as a colorimetric sensor for coronavirus detection [20-22]. To the best of our knowledge, no report has been published that describes a PDA-based colorimetric sensor to detect SARS-CoV-2.

In this study, a PDA-based flexible biosensor was developed for detecting the S protein of SARS-CoV-2, resulting in biosensors for SARS-CoV-2. The anti-N is an antibody protein of nucleocapsid (N) structural protein of SARS-CoV-2 that is responsible for the viral replication in host cells [23]. The anti-N protein is more sensitive to detect early COVID-19 infection in comparison to the antibody protein specific to the spike protein [24]. Therefore, the PDA-based flexible biosensor was prepared by electrospinning PDA nanofiber composite with the conjugation of SARS-CoV-2 anti-N protein. The carboxylic acid group (–COOH) in the PDAs was transformed into an open ester bond (-COO-) that provided a binding site for the anti-N. When the anti-N conjugated PDA nanofiber (PU-PDA-NHS-anti) was introduced to the spike protein of the SARS-CoV-2, the nanofibers demonstrated a colorimetric transition from blue to red after incubation and the intensity of the color of red was increased after 24 hours of incubation. In a comparison with no color changes found in the non-functionalized PU-PDA fibers, the functionalized PU-PDA-NHS-anti fibers showed colorimetric responses to the S protein of SARS-CoV-2. The anti-N proteins in the PU-PDA-NHS-anti fibers probably interacted with the S protein which triggered the color change in the fiber. Because the PDA nanofibers were flexible and lightweight and did not require a power supply such as a battery when the colorimetric detection to S protein occurred, the PDA nanofibers could be used in developing wearable devices for detecting SARS-CoV-2. Wearable devices, which allow physiological signals to be continuously monitored, can be used in the early detection of asymptomatic and pre-symptomatic cases of COVID-19 [25]. Wearable

devices such as facemasks and medical gowns using the PDA nanofiber composites can be potentially developed to monitor in real-time the contamination of SARS-CoV-2.

6.2 Methodologies and discussions

To prepare the PU-PDA-NHS-anti nanofiber biosensor, at first the 10, 12-pentacosadiynoic acid (PCDA) monomer was chemically functionalized to PCDA-NHS (supplementary document). During this functionalization, the carboxylic acid groups (-COOH) of PCDAs were transformed into open ester bonds (-COO-). To confirm the functionalization, a Nicolet 6700 Fourier Transform Infrared spectroscopy (FTIR) spectrometer (Thermo Electron Corporation, Madison, WI, USA) was used to collect Attenuated Total Reflection (ATR)- FTIR spectra of the PCDA and PCDA-NHS powders. The FTIR spectra of PCDA-NHS powder had a peak at wavenumber 1723cm^{-1} that corresponds to ester bond (-COO-). This peak was not found in PCDA powders. The PCDA powders showed a peak at wavenumber 1689cm^{-1} corresponding to carboxylic acid (-COOH) stretching typical in PCDA [16] (**Figure 6.2**).

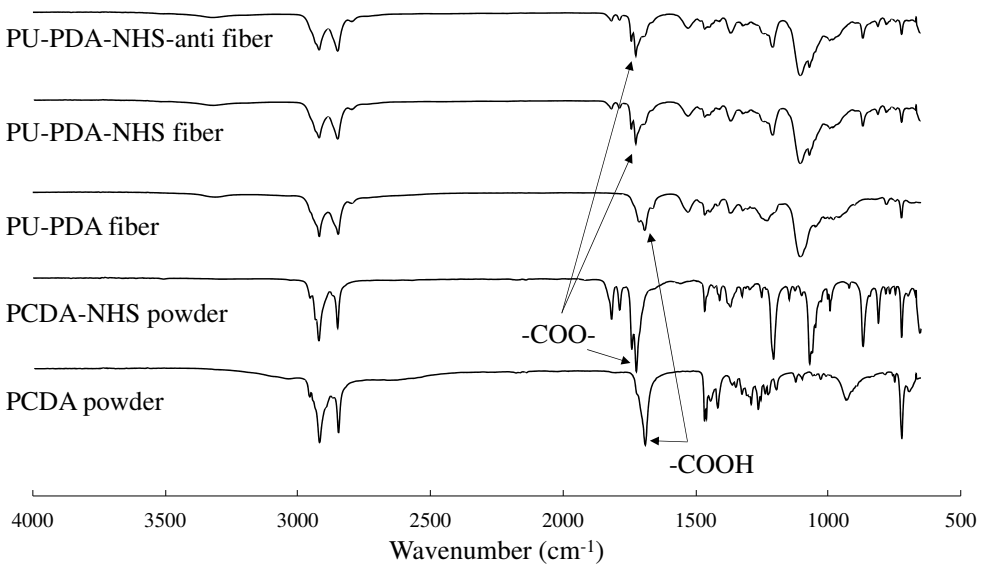

Figure 6.2. FTIR spectra of PCDA powders and PDA fiber samples.

Then, PCDA, and PCDA-NHS powders and polyurethane (PU) matrix polymer were used to prepare PU-PDA-NHS fiber mats via electrospinning technique. Additionally, control samples of PU-PDA fiber mats were prepared by the procedures described in our previous report [12]. Both PU-PDA and PU-PDA-NHS fiber mats were blue (**Figure 6.3a**). The fiber mats were peeled off from the aluminum foil as shown in **Figure 6.2b**. Fibers were highly stretchable and curled up after peeling from the aluminum foil, suggesting good flexibility (**Figure 6.3c**).

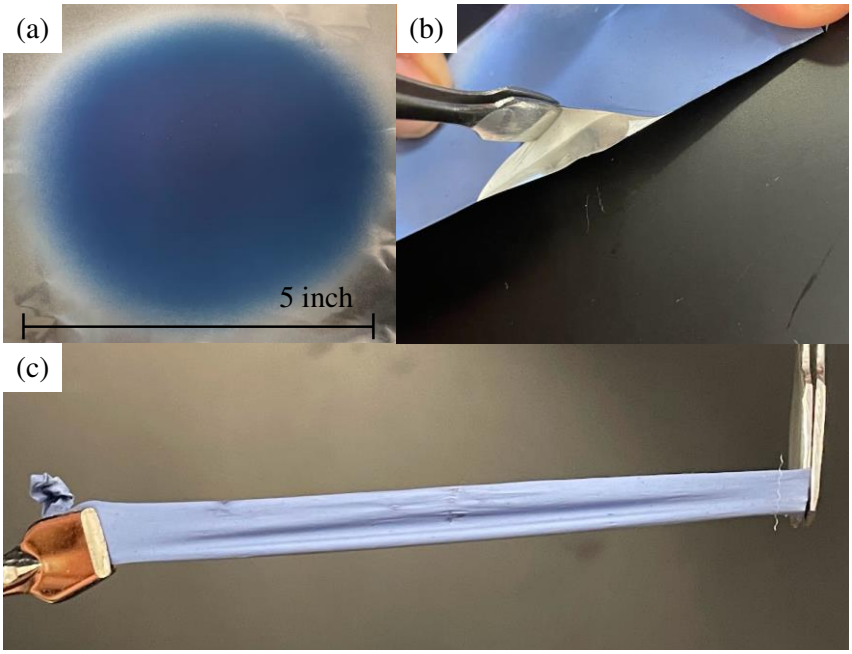

Figure 6.3. Images of (a) PDA nanofiber mat, (b) fiber mat during peeling off the aluminum foil, and (c) demonstration of high stretchability.

FTIR spectra of PU-PDA and PU-PDA-NHS fibers exhibited a similar trend as PCDA and PCDA-NHS powders. PU-PDA fibers showed a peak at wavenumber 1691cm^{-1} (-COOH) that was not present in PU-PDA-NHS fibers. Instead, a new peak at wavenumber 1725cm^{-1} (-COO-) was observed in PU-PDA-NHS fibers (**Figure 6.2**). The results confirmed the esterification of PCDAs as a binding site for the anti-N protein [16, 19]. Finally, PU-PDA-NHS fiber mats were incubated

with a solution containing 2μg/mL anti-N protein for 48 h at 4°C to prepare PU-PDA-NHS-anti fiber mats. No significant difference was found between the PU-PDA-NHS and PU-PDA-NHS-anti fibers when comparing the FTIR spectra (**Figure 6.2**).

To confirm the anti-N conjugation occurring to the PU-PDA-NHS fibers, FTIR spectra were collected for PDA-NHS powders without PU. PCDA-NHS powders were photopolymerized and then UV irradiated at 254 nm for 3 min, resulting in PDA-NHS powders. The PDA-NHS powders were incubated with anti-N and FTIR spectra were taken before and after the incubation. The result showed a significant increase in the N-H stretching peak (3360 cm^{-1}) (**Figure 6.4**, arrow marked), arising due to the presence of nitrogen (N) in anti-N protein composition. The presence of N-H stretching peak confirmed the successful anti-N conjugation with the PDA-NHS (**Figure 6.4**).

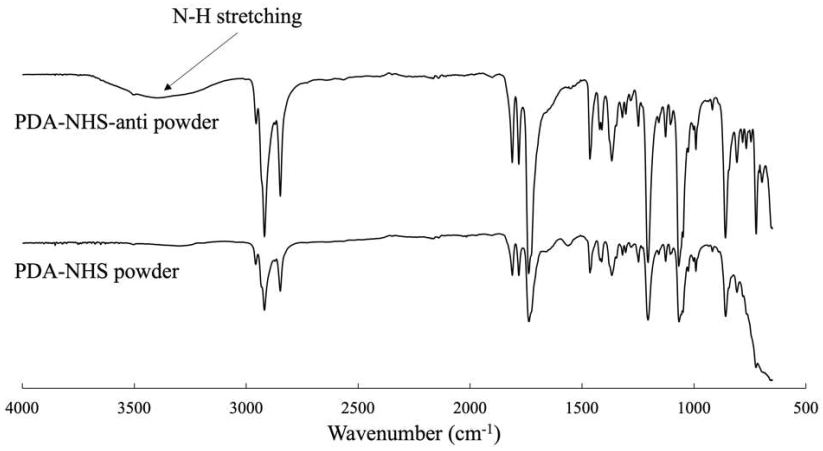

Figure 6.4. FTIR spectra of PDA-NHS and PDA-NHS-anti powders.

After the preparation of PU-PDA-NHS-anti nanofiber biosensor, circular fiber samples were cut to fit inside a 48-well plate. The fiber samples were washed using sterile water and PBS before they were incubated in SARS-CoV-2 S protein (SinoBiological, Wayne, PA) solution (1 μg/mL) using a low attachment 48-well plate at room temperature. The S protein solution was

diluted using a dilution factor suggested by the manufacturer. All the results reported here were obtained using the dilution factor of 1:500 that determined the protein concentration was 1 μg/mL. Previous report from our lab confirmed that PDA nanofibers do not change color at temperature less than 60°C [11], so temperature during testing condition did not affect the colorimetric or morphological properties of the PDA nanofibers. Control samples of PU-PDA, PU-PDA-NHS fibers were also incubated with S protein solution. Morphological analysis of the fibers was conducted before and after the S protein incubation using Scanning Electron Microscopic (SEM) images. A JEOL JSM-6500 Field Emission Scanning Electron Microscope was used to collect SEM images. The results showed that PU-PDA fibers had a scale-like structure on the fiber surface which confirmed the attachment of PDAs on the PU fibers [12-13] (**Figure 6.5**). PU-PDA-NHS fibers had a similar morphology on the surface (**Figure 6.5**). The PU-PDA-NHS-anti fibers had a similar structure but had some dot-like structures on the surface, which might be the anti-N proteins because this fiber was incubated for 48 h in the anti-N protein solution (**Figure 6.5**, **inset**). The size of these dot-like structures varied from 50 nm to 700 nm, indicating different degrees of coagulation of antibody protein on the fiber surface. After 24 h of incubation with S protein, the PU-PDA fiber morphology remained the same, suggesting no chemical reaction between the fiber and S protein (**Figure 6.5**). In comparison, the PU-PDA-NHS and PU-PDA-NHS-anti fibers showed a very rough surface after incubation with S protein (**Figure 6.5**). Larger scale-like structures were observed in the fibers. The results indicated the topographical changes in the fiber morphology might be due to the interaction between the fibers (PU-PDA-NHS and PU-PDA-NHS-anti) and S protein.

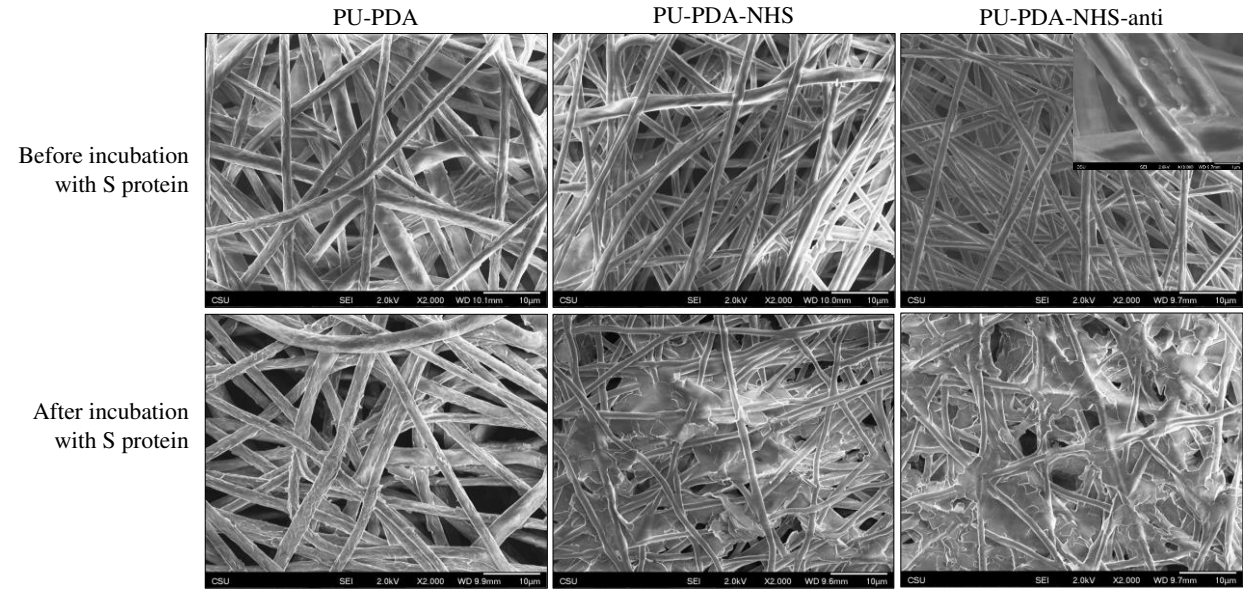

Figure 6.5. SEM images PDA fibers before and after incubation with S protein.

From the SEM images, fiber diameters were measured using the imageJ software. 10 fiber samples from each category were analyzed for fiber diameter analysis before and after incubation with S protein. The average diameter of PU-PDA nanofibers was 1700 nm. The PU-PDA-NHS and PU-PDA-NHS-anti nanofibers had average diameters of 1200 and 1300 nm respectively. The reduction of diameter in PU-PDA-NHS and PU-PDA-NHS-anti fibers was likely due to the addition of functionalized PCDA-NHS in the electrospinning solution. While electrospinning, the fibers were deposited randomly on the collector plate due to the high electrostatic force. So, the size of the nanofibers was not same for all the fibers, rather had a range of diameters as shown in **Figure 6.5**. The variation in diameter was not drastic compared to the previously reported PDA nanofibers prepared via electrospinning [12, 14, 26]. To evaluate statistically significant differences in the fiber diameters, Analysis of Variance (ANOVA) and Tukey's Honest Significant Difference (HSD) tests were performed. The results (**Figure 6.6**) indicated that there was no significant difference between PU-PDA fibers before and after S protein incubation, which is in

good agreement with the morphological observation of the fibers and indicated that the S protein did not react with the PU-PDA fibers. The diameters of the PU-PDA-NHS and PU-PDA-NHS-anti fibers were reduced after S protein incubation, which was likely due to the interaction between PDA fibers and S proteins. However, the diameter reduction in PU-PDA-NHS fiber after S protein incubation was not statistically significant. Fiber morphology and fiber diameter may change due to changes in electrospinning parameters [27], addition of surfactants, chemicals, and drug molecules [28], as well as external stimuli [29]. Previous studies reported a diameter increase and a scale-like morphological change in the PU-PDA fibers in comparison with pristine PU fibers [12]. When the PDAs were modified to prepare PU-PDA-NHS and PU-PDA-NHS-anti fibers, the scale-like structure was also observed (**Figure 6.5**). Then, after the fibers were incubated with S protein, the scales on fiber surface were disrupted as shown in **Figure 6.4**. A hypothesis was that the changes in fiber surface morphology were due to the interaction between antibody conjugated PDA-NHS and S protein. **Figure 6.5** shows no changes found in the PU-PDA fiber after incubation with S protein. It was likely because there was no interaction with the S protein due to the absence of PDA-NHS or PDA-NHS-anti. The nature and dynamics of the interaction between PDA-NHS-anti molecules in the fibers with S protein of SARS-CoV-2 needs further experimental analysis.

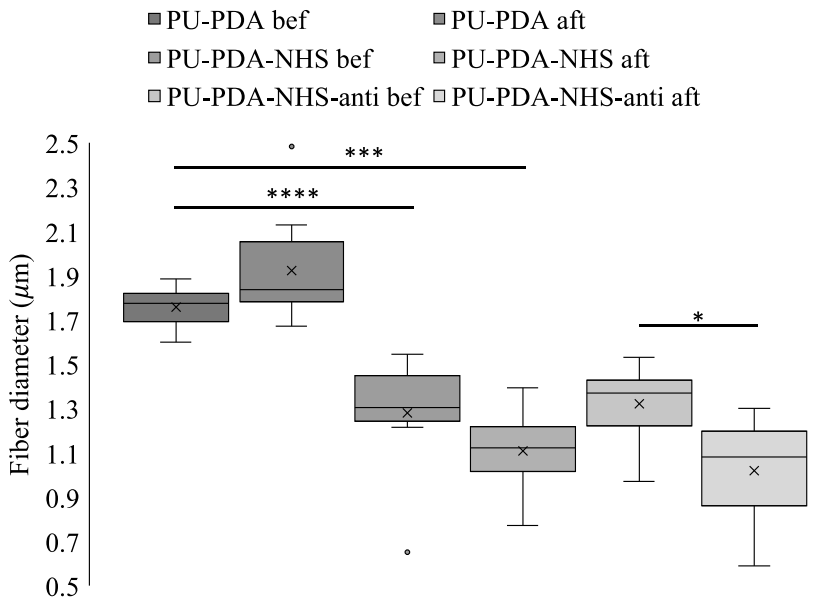

Figure 6.6. PDA fiber diameter before and after incubation with S protein. ANOVA and HSD were performed for statistical analysis (*, ***, and **** indicates $p \leq 0.05$, $p \leq 0.001$ and $p \leq 0.0001$).

When the PU-PDA-NHS-anti fiber was incubated with S-protein (1 μg/mL) at room temperature, the fiber started changing color from blue to red after 4 h of incubation. The color of red became bright after 24 h of incubation (**Figure 6.7a**). In addition, PU-PDA and PU-PDA-NHS fibers were incubated with the S protein. No color change was observed in PU-PDA fibers as expected, which was in good agreement with the morphological observation and fiber diameter analysis. Furthermore, a significant color change was observed in PU-PDA-NHS fiber after 24 h of incubation with S protein (**Figure 6.7a**). That was because the PU-PDA-NHS fiber had open ester groups (-COO-) on macromolecules and hence some S proteins might have been able to conjugate to the PU-PDA-NHS fiber, resulting in a color change. Additionally, all the fibers were incubated with the buffer solution that was used to prepare the S protein solution and no color change was observed. The buffer solution was composed of 0.1% Bovine Serum Albumin (BSA)

protein in wash buffer. The PDA fibers did not change color when they were incubated with buffer solution, thus signifying a specific detection of S protein.

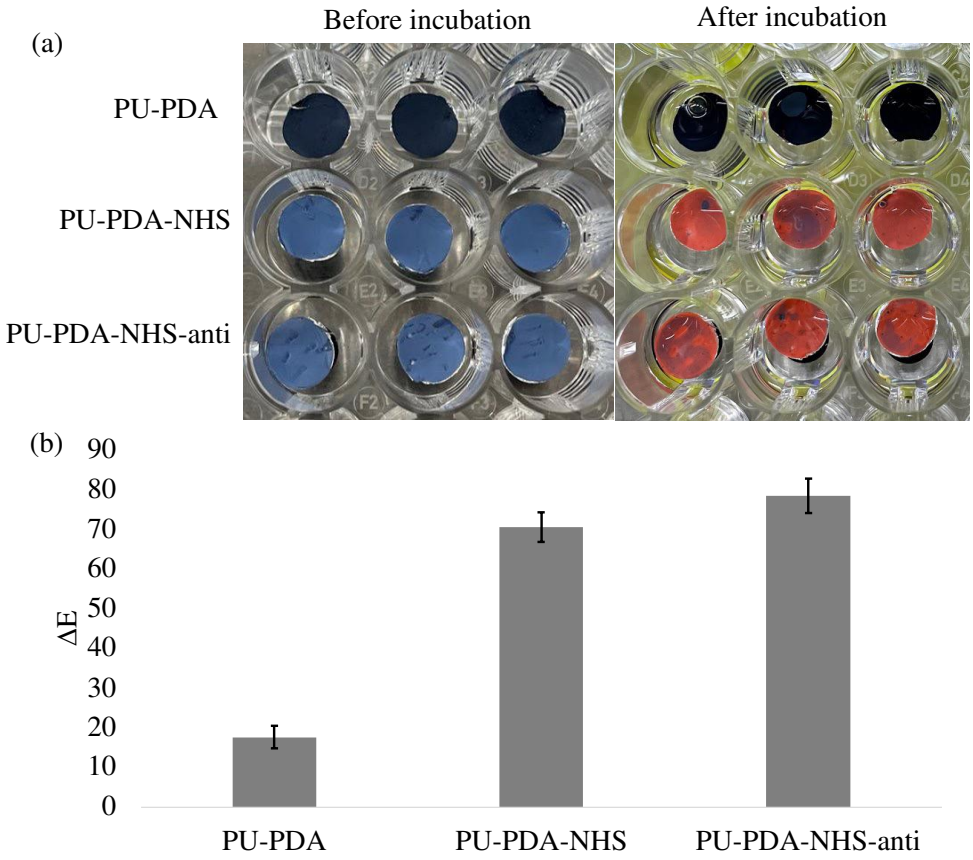

Figure 6.7. (a) Photographs of PDA fibers before and after 24 hours of incubation with S protein, (b) ΔE values of PDA fibers.

The color change in the fibers were quantified using CIE (International Commission of Illumination) color space coordinates that include the values of L*, a*, and b* representing lightness, color position between green and red, and color position between yellow and blue respectively [30]. Photographs of PDA fibers were taken before and after 24 h of incubation with S protein (**Figure 6.7**). CIE L*a*b* values were obtained from the photograph using Digital Color Meter application (Apple Inc.). 20 values of L*, a*, and b* were collected for each fiber on the

photographs. 10 values were for samples before incubation and 10 values were for after incubation. The color change of the fibers was quantified by calculating the ΔE values using Equation (1).

$$\Delta E = \sqrt{(\Delta L)^2 + (\Delta \mathrm{a})^2 + (\Delta b)^2} \qquad (1)$$

where ΔL, Δa, and Δb are the differences in brightness, redness, and yellowness of the fibers before and after the incubation with S protein [30], respectively. The ΔE values are shown in **Figure 6.7(b)**. The ΔE for PU-PDA was 17.61, which is very low compared to the ΔE of PU-PDA-NHS (70.52) and PU-PDA-NHS-anti (78.49) fibers. The higher ΔE of PU-PDA-NHS and PU-PDA-NHS-anti fibers confirmed a distinguishable color change in the fibers after incubation with S protein. Additionally, it was observed that the difference in the ΔE between PU-PDA-NHS and PU-PDA-NHS-anti was very minimum, suggesting that the antibody functionalization may not be necessary for S protein detection. The removal of antibody conjugation can offer cost reduction in biosensor preparation, however, because the color change in PU-PDA-NHS fiber was not proven specifically due to the open ester bond, more control experiments need to be conducted in the future to fully understand the specificity of the fiber.

The average L*a*b* of the fibers before and after incubation with S protein were collected. A negative a* value represents green region but positive a* represents red, and a negative b* indicates blue whereas a positive b* indicates yellowness [31]. b* of all fibers were negative before S protein incubation, meaning the fibers were blue. However, after the incubation, only PU-PDA fiber's b* remained negative (-5.749) which indicated the fiber color remained blue after S protein incubation. On the other hand, a* values of PU-PDA-NHS (44.341) and PU-PDA-NHS-anti (48.614) became positive after S protein incubation, indicating the color of these fibers shifted to red.

The vivid blue to the red transformation of the PU-PDA-NHS-anti fiber suggested an interaction between the S protein and the anti-N protein that might have been responded by a perturbation in the electron cloud of the PDAs and resulted in a color change. The nature of this protein-protein interaction between anti-N and S proteins will be investigated in the future. The initial indication of this protein-protein interaction can help to prepare targeted therapeutics and efficient biosensors that can effectively sense and inactivate the SARS-CoV-2 in the respiratory cells. The preliminary results that were illustrated here have demonstrated that the antibody conjugated PDA nanofibers have the potential in creating wearable devices and personal protective equipment such as facemasks and medical gowns for real-time detecting and monitoring SARS-CoV-2 contamination and contraction on a daily basis as well as in a healthcare setting. Further investigation will focus on sensitivity, selectivity, and biosafety of PDA's colorimetric responses to S protein, which are critical in proof-of-concept of using PDAs in SARS-CoV-2 detection techniques. Additional studies such as comparability and durability of the flexible PDA nanofibers should be considered with the textile materials commonly used in personal protective equipment such as facemasks and medical gowns. A viral load model was described by Soto et al. (2021), where a 4 h timeframe provided a sufficient threshold number of virus captured by a functionalized face mask to perform analytical analysis [32]. The PDA nanofiber biosensor described in this work exhibited a color change after 4 h of incubation with the S protein of SARS-CoV-2, which was consistent with the timeframe reported by Soto et al. (2021) [32]. The 4 h timeframe is a good indication of mask wearing base requirement for an effective sensing of the virus via a mask protection. Future work would require a detection study with live SARS-CoV-2 as well as an optimization study of electrospinning parameters and antibody concentration in the fiber to improve the sensitivity of the PDA nanofibers.

6.3 Conclusions

PDA nanofibers were obtained via chemical functionalization of PCDA monomer and electrospinning, resulting in a binding site for a receptor molecule – nucleocapsid antibody (anti-N) protein of SARS-CoV-2. The anti-N protein was attached to the functionalized PDA fibers via conjugation, resulting in PU-PDA-NHS-anti fibers. The PU-PDA-NHS-anti fibers showed a colorimetric transition from blue-to-red when interacting with S protein of SARS-CoV-2 at room temperature, suggesting it was a colorimetric detection of SARS-CoV-2. The results demonstrated the potential of using PDA nanofibers in creating a flexible, lightweight, no-battery, and colorimetric biosensor. The PDA biosensors can be used in developing wearable devices and personal protective equipment such as facemasks and medical gowns, providing real-time detection to COVID-19 contraction and hence timely medical decisions to improve public health in pandemics. In addition, the flexible PDA biosensors can be used in hygiene products, food processing, and food packaging, providing real-time detection via colorimetric indication. These smart products will empower individuals in the decision-making process and improve health and well-being.

REFERENCES

1. Bhattacharjee, A., Sabino, R. M., Gangwish, J., Manivasagam, V. K., James, S., Popat, K. C., ... & Li, Y. V. (2022). A novel colorimetric biosensor for detecting SARS-CoV-2 by utilizing the interaction between nucleocapsid antibody and spike proteins. *In vitro models*, *1*(3), 241-247. https://doi.org/10.1007/s44164-022-00022-z
2. Hoffmann M, Kleine-Weber H, Schroeder S, Krüger N, Herrler T, Erichsen S, Schiergens TS, Herrler G, Wu N-H, Nitsche A, Müller MA, Drosten C, Pöhlmann S. SARS-CoV-2 cell entry depends on ACE2 and TMPRSS2 and is blocked by a clinically proven protease inhibitor. Cell 2020; 181(2):271-80. https://doi.org/10.1016/j.cell.2020.02.052
3. Zhu N, Zhang D, Wang W, Li X, Yang B, Song J, Zhao X, Huang B, Shi W, Lu R, Niu P, Zhan F, Ma X, Wang D, Xu W, Wu G, Gao GF, Tan W. A novel coronavirus from patients with pneumonia in China, 2019. New Engl. J. Med. 2020; 382:727-33. https://doi.org/10.1056/NEJMoa2001017
4. Coronavirus Disease 2019 (COVID-19) Situation Report - 51. World Health Organization. 2020. https://www.who.int/docs/default-source/coronaviruse/situation-reports/20200311-sitrep-51-covid-19.pdf?sfvrsn=1ba62e57_10
5. Weekly Operational Update on COVID-19, Issue No. 80. World Health Organization. 2021. https://www.who.int/publications/m/item/weekly-operational-update-on-covid-19---15-november-2021
6. Ashour HM, Elkhatib WF, Rahman MM, Elshabrawy HA. Insights into the recent 2019 novel coronavirus (SARS-CoV-2) in light of past human coronavirus outbreaks. Pathogens 2020; 9(3):186-201. https://doi.org/10.3390/pathogens9030186

7. Zhou P, Yang X-L, Wang X-G, Hu B, Zhang W, Si H-R, Zhu Y, Li B, Huang C-L, Chen H-D, Chen J, Luo Y, Guo H, Jiang R-D, Liu M-Q, Chen Y, Shen X-R, Wang X, Zheng X-S, Zhao K, Chen Q-J, Deng F, Liu L-L, Yan B, Zhan F-X, Wang Y-Y, Xiao G-F, Shi Z-L. A pneumonia outbreak associated with a new coronavirus of probable bat origin. Nature 2020; 579:270-3. https://doi.org/10.1038/s41586-020-2012-7
8. Suman R, Javaid M, Haleem A, Vaishya R, Bahl S, Nandan D. Sustainability of coronavirus on different surfaces. Journal Of Clinical and Experimental Hepatology 2020; 10(4):386-90. https://doi.org/10.1016/j.jceh.2020.04.020
9. Lai C-C, Wang C-Y, Ko W-C, Hsueh P-R. In vitro diagnostics of coronavirus disease 2019: Technologies and application. J. Microbiol. Immunol. Infect. 2021; 54(2):164-74. https://doi.org/10.1016/j.jmii.2020.05.016
10. Talebian S, Wallace GG, Schroeder A, Stellacci F, Conde J. Nanotechnology-based disinfectants and sensors for SARS-CoV-2. Nat. Nanotechnol. 2020; 15:618-21. https://doi.org/10.1038/s41565-020-0751-0
11. Alam AKMM, Yapor J, Reynolds MM, Li YV. Study of polydiacetylene-poly (ethylene oxide) electrospun fibers used as biosensors. Materials 2016; 9(3): 1-13. https://doi.org/10.3390/ma9030202
12. Bhattacharjee A, Clark R, Gentry-Weeks C, Li, YV. A novel receptor-free polydiacetylene nanofiber biosensor for detecting *E. coli* via colorimetric changes. Mater. Adv. 2020; 1(9):3387-97. https://doi.org/10.1039/D0MA00619J
13. Hassan F, Gentry-Weeks C, Reynolds M, Li YV. Study on microstructure and mechanical properties of polydiacetylene composite biosensors. J. Appl. Polym. Sci. 2019; 136(34):47877. https://doi.org/10.1002/app.47877

14. Yapor JP, Alharby A, Gentry-Weeks C, Reynolds MM, Alam AKMM, Li YV. Polydiacetylene nanofiber composites as a colorimetric sensor responding to *Escherichia coli* and pH. ACS Omega 2017; 2(10):7334-42. https://doi.org/10.1021/acsomega.7b01136

15. Bhattacharjee A, Clark R, Gentry-Weeks C, Li YV. Study of bacterial components activating a colorimetric transition in bacteria-detecting nanofiber wound dressing applications. International Textile and Apparel Association Annual Conference Proceedings 2020; 77(1). https://doi.org/10.31274/itaa.12123

16. Son SU, Seo SB, Jang S, Choi J, Lim J-W, Lee DK, Kim H, Seo S, Kang T, Jung J, Lim, E-K. Naked-eye detection of pandemic influenza A (pH1N1) virus by polydiacetylene (pda)-based paper sensor as a point-of-care diagnostic platform. Sensor. Actuat. B- Chem. 2019; 291:257-65. https://doi.org/10.1016/j.snb.2019.04.081

17. Charych DH, Nagy JO, Spevak W, Bednarski M. Direct colorimetric detection of a receptor-ligand interaction by a polymerized bilayer assembly. Science 1993; 261(5121):585-8. https://doi.org/10.1126/science.8342021

18. Jiang L, Luo J, Dong W, Wang C, Jin W, Xia Y, Wang H, Ding H, Jiang L, He H. Development and evaluation of a polydiacetylene based biosensor for the detection of H5 influenza virus. J. Virol. Methods 2015; 219:38-45. https://doi.org/10.1016/j.jviromet.2015.03.013

19. Song S, Ha K, Guk K, Hwang S-G, Choi JM, Kang T, Bae P, Jung J, Lim E-K. Colorimetric detection of influenza A (H1N1) virus by a peptide-functionalized polydiacetylene (PEP-PDA) nanosensor. RSC Adv. 2016; 6:48566-70. https://doi.org/10.1039/C6RA06689E

20. Qian X, Städler B. Polydiacetylene-based biosensors for the detection of viruses and related biomolecules. Adv. Funct. Mater. 2020; 30(49):2004605. https://doi.org/10.1002/adfm.202004605

21. Bukkitgar SD, Shetti NP, Aminabhavi TM. Electrochemical investigations for COVID-19 detection-A comparison with other viral detection methods. Chem. Eng. J. 2021; 420(2):127575. https://doi.org/10.1016/j.cej.2020.127575

22. Tymm C, Zhou J, Tadimety A, Burklund A, Zhang JXJ. Scalable COVID-19 detection enabled by lab-on-chip biosensors. Cell. Mol. Bioeng. 2020; 13:313–29. https://doi.org/10.1007/s12195-020-00642-z

23. Troyano-Hernáez P, Reinosa R, Holguín Á. Evolution of SARS-CoV-2 envelope, membrane, nucleocapsid, and spike structural proteins from the beginning of the pandemic to September 2020: A global and regional approach by epidemiological week. Viruses 2021; 13(2):243. https://doi.org/10.3390/v13020243

24. Burbelo PD, Riedo FX, Morishima C, Rawlings S, Smith D, Das S, Strich JR, Chertow DS, Davey Jr RT, Cohen JI. Sensitivity in detection of antibodies to nucleocapsid and spike proteins of severe acute respiratory syndrome coronavirus 2 in patients with coronavirus disease 2019. The Journal of Infectious Diseases 2020; 222(2):206-13. https://doi.org/10.1093/infdis/jiaa273

25. Ates HC, Yetisen AK, Güder F, Dincer C. Wearable devices for the detection of COVID-19. Nat. Electron. 2021; 4:13-4. https://doi.org/10.1038/s41928-020-00533-1

26. Kim JH, Lee JS. Development of polydiacetylene embedded polyurethane nanocomposites as a mask for sensing and filtering fine dust. Fibers Polym. 2021; 22:489-97. https://doi.org/10.1007/s12221-021-0187-7

27. Bhardwaj N, Kundu SC. Electrospinning: A fascinating fiber fabrication technique. Biotechnol. Adv. 2010; 28(3):325-47. https://doi.org/10.1016/j.biotechadv.2010.01.004

28. Zeng J, Xu X, Chen X, Liang Q, Bian X, Yang L, Jing X. Biodegradable electrospun fibers for drug delivery. J. Control Release. 2003; 92(3):227-31. https://doi.org/10.1016/S0168-3659(03)00372-9

29. Aussawasathien D, Dong JH, Dai L. Electrospun polymer nanofiber sensors. Synthetic Met. 2005; 154(1-3):37-40. https://doi.org/10.1016/j.synthmet.2005.07.018

30. Arafat MT, Mahmud MM, Wong SY, Li X. PVA/PAA based electrospun nanofibers with pH-responsive color change using bromothymol blue and on-demand ciprofloxacin release properties. J. Drug Deliv. Sci. Tec. 2021; 61:102297. https://doi.org/10.1016/j.jddst.2020.102297

31. Agarwal A, Raheja A, Natarajan TS, Chandra TS. Development of universal pH sensing electrospun nanofibers. Sensor Actuat. B-Chem. 2012; 161(1):1097-101. https://doi.org/10.1016/j.snb.2011.12.027

32. Soto F, Ozen MO, Guimarães CF, Wang J, Hokanson K, Ahmed R, Reis RL, Paulmurugan R, Demirci U. Wearable collector for noninvasive sampling of SARS-CoV-2 from exhaled breath for rapid detection. ACS Appl. Mater. Interfaces. 2021; 13(35):41445-53. https://doi.org/10.1021/acsami.1c09309.

CHAPTER 7/CONCLUSIONS AND FUTURE WORKS

Nanostructured materials offer unique advantages to the bulk material for biomedical applications. In this work, titania (TiO_2) nanotubes (NT) were fabricated on titanium (Ti) orthopedic surfaces to improve the bioactivity of these implants. From the work described in **Chapter 2**, it is evident that NT surfaces differ in surface properties compared to the bulk Ti surface. The NT surface was superhydrophilic in nature which resulted from the presence of nanotubes that reduced the surface tension of the static water thus reducing the water contact angle. When important trace element zinc (Zn) was doped on the NT surface to prepare NT_{hyt} and NT_{alk}, the surfaces had unique morphological features. NT_{hyt} had crystal like structure and NT_{alk} exhibited a web-like structure identified by scanning electron microscopic (SEM) images. Energy-dispersive energy spectroscopy (EDS) maps confirmed an even distribution of Zn throughout both the surfaces. The relative atomic weight percentages (at %) of Zn on these surfaces were also evaluated by taking X-ray spectroscopy (XPS) spectra. All these material characterization results indicated a significant surface property difference on the nanostructured surfaces compared to the pure Ti surface property. Then, antibacterial property evaluation on these surfaces indicated that all the nanostructured surfaces (NT, NT_{hyt}, and NT_{alk}) could successfully reduce the bacterial adhesion compared to the pure Ti. NT_{hyt} surface which had hydrothermally doped Zn could reduce the bacterial adhesion more than the alkaline heat treated NT_{alk} surface.

In **Chapter 3**, two important trace elements Zn and strontium (Sr) were doped on the NT surface to prepare NTZn and NTSr. These surfaces also had unique surface properties that are different from pure Ti. Also, these surfaces did not possess any cytotoxicity towards adipose derived stem cells (ADSC). After 4 and 7 days of incubation with the ADSCs, it was observed that

the cells adhered to the NT surfaces could spread better due to the presence of nanotubes which acted as anchoring sites for the adhering cells. These adhered cells were also found to differentiate faster to osteoblasts which are bone cells that indicated better osseointegration properties imparted by the nanostructured surfaces. The adhered ADSCs on the NTSr surface differentiated in a faster rate compared to the other surfaces indicating the enhanced bioactivity resulting from the presence of nanotubes and signaling element.

In **Chapter 4**, the conjugated effect of antibacterial activity and osseointegration properties were discussed. A new surface NTZnSr was prepared which holds both the important trace elements Zn and Sr. This surface could significantly reduce both Gram-positive *S. aureus* and Gram-negative *P. aeruginosa* adhesion. This is due to the presence of Zn which acted as an antibacterial agent and reduced the bacterial adhesion on the new surface. The NTZnSr surface also indicated improved ADSC adhesion and spreading. These adhered cells also differentiated significantly faster to osteoblasts confirming the improvement in osseointegration property. Therefore, the nanostructured NTZnSr surface could enhance both the antibacterial and osseointegration properties of Ti orthopedic implants.

In future, the NTZnSr surface can be evaluated for *in vivo* studies. There has been growing interest for surface modification approaches to make orthopedic implants more bioactive. Majority of the implants fail due to the bacterial adhesion and poor osseointegration. Since the NTZnSr surface could improve both antibacterial and osseointegration properties on the Ti surface indicated by the *in vitro* studies, the obvious next step is to check the efficacy of this surface during *in vivo* studies. Commercial viability of this nanostructured surface can also be evaluated in the future studies.

Polydiacetylene (PDA) nanofiber biosensor was the other nanostructured material that was developed in this work for improving the bioactivity. PDA is a popular polymer that can change color in contact with an external stimulus such as bacteria and virus. For that reason, PDA based biosensors are popular in the biomedical research area. However, there is a lack of research efforts to prepare a flexible biosensor using the PDA polymer. Therefore, in this work, a PDA nanofiber biosensor was synthesized using electrospinning technique which was discussed in **Chapter 5**. The nanofiber color was blue after the photopolymerization which changed its color to red in the presence of Gram-negative bacteria *E. coli* and *P. aeruginosa*. However, no color change was observed at the presence of Gram-positive bacteria *S. aureus*. Therefore, the colorimetric transition was only due to the presence of a Gram-negative bacteria and thus the PDA nanofiber biosensor can selectively detect the Gram-negative bacteria. The difference in color change was due to the differences of extracellular proteins released by the different strains of bacteria. In future, the extracellular matrix polymers and proteins released by different bacterial strains can be evaluated in detail to understand the PDA color changing mechanism in depth. Also, the fiber's capability to selectively detect Gram-negative bacteria can be evaluated by incorporating the fiber in a commercially available product such as a face mask.

The PDA polymer has a flexible polymer structure with a carboxylic acid (-COOH) end group which can be chemically treated to produce carbonyl (-COO-) end group that has an open bond. This can be acted as a binding site for a receptor to detect specific targets such as a specific strain of bacteria or virus. Utilizing this flexibility of the PDA polymeric structure, the PDA biosensor was functionalized chemically to detect the spike protein of the pandemic coronavirus (SARS-CoV-2). The functionalization and the material properties are described in **Chapter 6**. For this, antibody nucleocapsid (anti-N) protein was conjugated to the PDA nanofiber. The

functionalized fiber could detect the spike protein (S) of SARS-CoV-2 by a colorimetric transition from blue to red which is visible to the human eye. So, the functionalized fiber could selectively detect the SARS-CoV-2 via a color change. This result indicated that the flexible nature of the PDA polymer chain can be utilized to selectively detect a diverse range of pathogens in the future. Also, the color changing mechanism can be evaluated more in depth in the future. Moreover, the fibers can be incorporated to different personal protective equipment in the future to evaluate their biosensing capability in a real-world scenario.